Modeling of Long-Term Multipactor Evolution in Microwave Components Including Dielectric Layers

THÈSE N^{O} 6535 (2015)

PRÉSENTÉE LE 12 MARS 2015
À LA FACULTÉ DES SCIENCES ET TECHNIQUES DE L'INGÉNIEUR
LABORATOIRE D'ÉLECTROMAGNÉTISME ET ACOUSTIQUE
PROGRAMME DOCTORAL EN GÉNIE ÉLECTRIQUE

ÉCOLE POLYTECHNIQUE FÉDÉRALE DE LAUSANNE

POUR L'OBTENTION DU GRADE DE DOCTEUR ÈS SCIENCES

PAR

Apostolos SOUNAS

acceptée sur proposition du jury:

Prof. C. N. Jones, président du jury
Prof. J. R. Mosig, Dr M. Mattes, directeurs de thèse
Prof. A. Melcon Alvarez, rapporteur
Prof. F. Rachidi-Haeri, rapporteur
Dr F. Zimmermann, rapporteur

ÉCOLE POLYTECHNIQUE
FÉDÉRALE DE LAUSANNE
Suisse
2015

Abstract

Multipactor is a resonant vacuum discharge occurring in microwave components of satellite systems as well as in particle accelerators. Due to its undesirable effects, multipactor analysis constitutes a mandatory step in the design of modern satellite components and in performance studies of particle accelerators. To this end, the development of computational techniques for multipactor prediction attracts intense interest in the scientific community.

The phenomenon evolves in two distinct phases: first, a fast growth of the electron population and, second, a steady state during which the population reaches a saturation level and remains almost constant. State-of-the-art computational models focus on the precise prediction of the initial multipactor phase, which defines whether the discharge occurs or not. However, a clear overview of the phenomenon also requires the analysis of the long-term multipactor evolution. Due to the high complexity introduced by considering saturation mechanisms, long-term multipactor evolution remains still unclear for many configurations of highly practical importance. Such a case is the multipactor analysis in the presence of dielectrics, a case dealt within this thesis.

Motivated by the challenging nature of analyzing the multipactor steady state, this work aims to provide its own contribution to the modeling and the analysis of long-term multipactor evolution. For this, a sophisticated computational tool has been developed for the full-3D multipactor analysis, taking into account saturation mechanisms.

In order to get a fast overview of the phenomenon, a generalized single-electron model has been developed which allows a multipactor analysis in any configuration with unidirectional-like electric field. Based on this 1D model, qualitative studies considering the effect of low-energy electron collisions and of single-sided multipactor in non-uniform coaxial fields have been performed. As a further step, a multiple-particle, full-3D model able to consider the stochastic nature of the secondary emission phenomenon has been developed. The single-electron model nicely supplements the robust 3D analysis by providing fast estimations for the most likely cases in which multipactor occurs.

Saturation mechanisms have been considered, too, for both 1D and 3D approximations. Taking into account the induced charges on the metallic boundaries, a fast analysis of long-term multipactor is provided by the 1D model for the parallel plate and coaxial line cases. The saturation study is boosted in the 3D analysis by taking into account the mutual Coulomb interaction between particles.

The developed multipactor model has been properly adapted in order to study long-term multipactor in the case of dielectric-loaded waveguides. Space charge effects as well as the effect of the surface charge developed on the dielectric layer have been both considered in the analysis. Particularly, in order to efficiently take into account the effect of the induced charges, a novel image method for the evaluation of the 3D Green function in multi-layered media has been developed. For the first time, a saturation steady state is identified in parallel plates loaded with a dielectric layer.

Keywords: multipactor, multipactor modeling, single electron model, multiple electron model, long-term multipactor, multipactor saturation, image method, dielectrics

Résumé

L'effet multipactor est un phénomène de décharge électronique résonnant dans le vide qui se produit dans les composants micro-ondes de systèmes satellite ainsi que dans les accélérateurs de particules. En raison des effets indésirables de l'effet multipactor, l'analyse de ce dernier constitue une étape incontournable dans la conception des composants de satellites modernes et dans l'étude de performance des accélérateurs de particules. A cet effet, le développement des techniques de calcul pour la prévision de l'effet multipactor provoque un vif intérêt dans la communauté scientifique.

Le phénomène évolue en deux phases distinctes: premièrement, une croissance rapide de la population d'électrons et, deuxièmement, un état d'équilibre au cours duquel la population atteint un niveau de saturation et demeure à peu près constante. Les modèles computationnels de l'état de l'art se concentrent surtout sur la prédiction précise de la phase initiale de l'effet multipactor, phase qui définit si la décharge a lieu ou non. Cependant, un aperçu clair du phénomène exige également l'analyse de l'évolution à long terme de l'effet multipactor. En raison de la grande complexité induite par la considération des mécanismes de saturation, l'évolution à long terme de l'effet multipactor reste encore très floue pour de nombreuses configurations d'importance grandement pratique. L'analyse de l'effet multipactor en présence de diélectriques fait partie de ces configurations et celle-ci est traitée dans cette thèse.

Motivé par la nature difficile de l'analyse de l'état stationnaire de l'effet multipactor, ce travail vise à offrir sa propre contribution à la modélisation et à l'analyse de l'évolution à long terme de l'effet multipactor. Pour cela, un outil de calcul sophistiqué a été mis au point pour l'ensemble de l'analyse entièrement 3D de l'effet multipactor, en tenant compte des mécanismes de saturation.

Afin d'obtenir un aperçu rapide du phénomène, un modèle à électron unique généralisé a été mis au point, modèle qui permet l'analyse de l'effet multipactor dans n'importe quelle configuration avec un champ électrique unidirectionnel. Basées sur ce modèle 1D, des études qualitatives considérant l'effet des collisions d'électrons de faible énergie et de l'effet multipactor unilatéral dans les câbles coaxiaux non uniformes ont été effectuées. Ensuite, un modèle entièrement 3D à particules multiples a été développé, qui est en mesure d'examiner la nature stochastique du phénomène d'émission secondaire. Le modèle à électron unique est complémentaire à l'analyse robuste en 3D, fournissant des estimations rapides pour les cas où les décharges de l'effet multipactor sont le plus probable.

Les mécanismes de saturation ont aussi été considérés pour les deux approximations 1D et 3D. Compte tenu des charges induites sur les bords métalliques, une analyse rapide de l'effet multipactor à long terme est fournie par le modèle 1D de la plaque parallèle et dans le cas de la ligne coaxiale. L'étude de saturation est améliorée dans l'analyse 3D en tenant compte de l'interaction mutuelle de Coulomb entre les particules.

Le modèle de l'effet multipactor développé a ètè correctement adaptè afin d'ètudier l'effet multipactor à long terme dans le cas de guides d'ondes en présence de diélectriques. Les effets de charge dans l'espace ainsi que l'effet de charge de surface développés sur la couche diélectrique ont aussi été examinés dans l'analyse. En particulier, afin de prendre efficacement en compte l'effet de charges induites, une nouvelle méthode des images pour l'évaluation de la fonction de Green 3D dans les milieux multicouches a été développèe. Pour la première fois, un état d'équilibre de saturation est identifié dans des plaques parallèles en présence d'une couche diélectrique.

Mots-céls: effet multipactor, modélisation de l'effet multipactor, modèle d'électron unique, modèle à électrons multiples, effet multipactor à long terme, saturation de l'effet multipactor, méthode des images, diélectriques.

Kurzfassung

Multipaktor ist eine Entladung, die in Vakuum unter Resonanzbedingungen auftritt und sowohl Mikrowellenkomponenten in Satellitensystemen als auch Teilchenbeschleuniger betrifft. Wegen der dazugehörenden unerwünschten Effekte, ist eine Multipaktoranalyse ein unverzichtbarer Schritt in der Synthese von Mikrowellenkomponenten und Effizienzstudien von Teilchenbeschleunigern. Die Entwicklung von Simulationsmethoden zur Vorhersage von Multipaktor ist daher auf großes Interesse.

Multipaktor verläuft prinzipiell in zwei Phasen: als erstes kommt es zu einem raschen Anstieg von freien Elektronen in den Komponenten. Danach folgt die Sättigungsphase, in der die Anzahl der Elektronen nahezu konstant bleibt. In modernen Computermodellen wird vor allem die erste Phase betrachtet, die darüber entscheidet, ob es zu einer Entladung kommt oder nicht. Für eine genaue Analyse des Phänomens muß allerdings auch dessen Langzeitverhalten untersucht werden. Da die Berücksichtigung von Sättigungsmechanismen die Komplexität der Simulationsmodelle drastisch erhöht, ist das Langzeitverhalten von Multipaktor für viele Geometrien, die von hohem praktischem Interesse sind, jedoch unklar.

Diese Arbeit möchte einen Beitrag zur Untersuchung von Langzeitmultipaktor leisten. Zu diesem Zweck wurde ein fortgeschrittener Algorithmus entwickelt und implementiert, der die Simulation von 3D Problem unter Einbeziehung von Sättigungsmechanismen erlaubt.

Für eine schnelle Multipaktoranalyse wurde ein Einelektronenmodell für Geometrien entwickelt, die durch 1D elektrische Felder angenähert werden können, wie z. B. in einem Parallelplattenleiter. Basierend auf diesem 1D Modell wurden qualitative Studien für niederenergetische Elektronenkollisionen und einseitigem Multipaktor in ungleichförmigen Koaxialfeldern durchgeführt. Als nächstes wurde ein 3D Mehrelektronenmodell entwickelt, das das stochastische Verhalten der sekundären Elektronenemission berücksichtigt. Das Einelektronenmodell stellt dabei eine ideale Ergänzung zum 3D Modell dar, weil es eine sehr schnelle Abschätzung von möglichen Multipaktorproblemen erlaubt.

Sättigungsmechanismen wurden sowohl für 1D als auch 3D Modelle berücksichtigt. Unter Einbeziehung der induzierten Ladung an den Rändern ist eine schnelle Analyse von Langzeitmultipaktor für 1D Modelle wie Parallelplatten- und koaxiale Hohlleiter möglich. Zusätzlich wird im 3D Modell die Coulomb-Wechselwirkung zwischen den Teilchen berücksichtigt, um die Sättigungsphase zu simulieren.

Um das Langzeitverhalten für Strukturen mit Dielektrika zu untersuchen, wurden die entwickelten Multipaktormodelle entsprechend erweitert. Dabei wurden sowohl der Einfluß der Elektronenwolke als auch die Oberflächenladung auf dem Dielektrikum in die Berechnungen mit einbezogen. Insbesondere, um die induzierte Ladung effizient zu modellieren, wurde eine neue Spiegelladungsrepräsentation der 3D Greenschen Funktion für mehrschichtige Strukturen entwickelt. Dies ermöglichte zum ersten Mal die Simulation des Sättigungsbereichs von Multipaktor in Parallelplattenleitern mit dielektrischen Schichten.

Stichworte: Multipaktor, Multipaktormodellierung, Einelektronenmodell, Mehrelektronenmodell, Langzeitmultipaktor, Multipaktorsättigung, Spiegelladungsmethode, Dielektrika

Acknowledgements

First and foremost, I would like to thank my thesis advisor and co-advisor, Prof. Juan R. Mosig and Dr. Michael Mattes, respectively, for providing me with the great opportunity to join the Laboratory of Electromagnetics and Acoustics (LEMA) in order to pursue my PhD. I am very thankful to Juan, not only for his invaluable scientific advices, for his exceptional pedagogical skills but also for his positive attitude making the environment in LEMA uniquely warm and friendly. My deepest thanks to Michael, for his invaluable guidance throughout this thesis, his willingness to help and discuss any time and above all for his great personality.

I would like to thank the committee members, Prof. Alejandro Álvarez Melcón, Dr. Frank Zimmermann, Prof. Farhad Rachidi-Haeri and Prof. Colin Jones for examining this work, for their interesting comments and for their valuable suggestions on improving the final content of this thesis. This work has been supported by the Swiss Commission for Technology and Inovation (CTI) through my involvement in the project POSEIDON. I am grateful for this support as well as for the nice collaboration I had with the other partners involved in the project. Special thanks to Nik Chavannes and Pedro Crespo from SPEAG AG.

I am very thankful to Thanos Polimeridis for his wise advices before and during my PhD. I cannot miss to thank also Prof. Trainos Youltsis, my diploma thesis advisor, for inspiring and encouraging me to do PhD in such a nice institute.

I would like to thank all my great colleagues and friends from LEMA for making the lab being a pleasant place to work. Many thanks to Prof. Anja Skrivervik for the very interesting and fruitful discussions, to Jean-François Zürcher for his technical support in LEMA, to Eulalia Durussel and to Mercedes Quintas for the kind secretarial support. Many thanks to all former and current LEMA members. Special thanks to Yiannis for sharing great moments all these years, to Sebas and Marc for our interesting discussions and for the great tennis games, Jovanche, Marco and Gabriele for the exciting ski days. Many thanks to Benji, Eden and Mina for being such nice officemates. To the former LEMA members, Ruzica, Roberto, Madda, Francesco, Fred and to the current LEMA members, Joana, Maria, Anton, Baptiste, Santiago, Tomislav, Michele, Hussein, Hamed, Pietro, Pedro many thanks for the excellent time we spent together. Nevena, thank you for the nice Serbian delicacies.

At this point, I would like to express my warmest thanks to Prêtre Alexandros Iossifidis and his wife Ploumi, for making me feel as a member of their family. Special thanks to Teo, Alex, Polydefkis, Giannis Lignos who were the core of the Greek team when I arrived in Lausanne. Many thanks to Pavlos and Nathalie for our nice friendship, and to many other Greek friends.

My deepest gratitude goes to my parents, Georgia and Lemonis, and to my brother, Dimitris, who have generously supported me, by any possible means, despite the distance. Dimitris, special thanks for you invaluable scientific help. To all of you, I devote this thesis.

Contents

1. Introduction 1

1.1. Context . . . 1

1.2. Motivation . . . 2

1.3. Objectives . . . 3

1.4. Outline and Original Contributions . . . 4

2. Multipactor Review 7

2.1. Introduction . . . 7

2.2. Multipacting . . . 7

2.3. Secondary Electron Emission . . . 8

2.3.1. Secondary Emission Yield . . . 9

2.3.2. Emission Energy Distribution . . . 11

2.3.3. Angular Distribution of the Emitted Electrons . . . 12

2.4. Resonant Motion . . . 14

2.4.1. Resonance Conditions . . . 14

2.4.2. Phase Focusing . . . 16

2.5. Saturation . . . 18

2.6. Summary . . . 19

3. The Single Electron Model 21

3.1. Introduction . . . 21

3.2. Model Assumptions and Applicability . . . 22

3.3. Theoretical Analysis . . . 23

3.3.1. Resonance condition 24
3.3.2. Secondary Emission condition 26
3.3.3. Stability Condition 27
3.3.4. Multipactor Chart 30
3.4. Generalized Single Electron Model 32
3.4.1. Algorithm 34
3.4.2. Multipactor Chart Representation 36
3.4.3. Validation 38
3.5. Examples of Analysis 39
3.5.1. Effect of elastic reflection in multipactor evolution 40
3.5.2. Multipacting in coaxial lines 44
3.6. Summary 47

4. Multipactor in the Presence of Dielectrics **51**
4.1. Introduction 51
4.2. Theory 52
4.3. 1D Approach 53
4.3.1. Formulation 53
4.3.2. Analysis 58
4.3.3. Summary 69
4.4. 3D Approach 71
4.4.1. Modeling 71
4.4.2. Formulation 75
4.4.3. Example of Analysis 76
4.5. Summary 78

5. Image Method for Multilayered Shielded Media **81**
5.1. Introduction 81
5.2. Image Series Formulation 82
5.2.1. Green Function Derivation 82

5.2.2. Extraction of Singular Images 88
5.3. Numerical Examples 88
5.3.1. Validation 90
5.3.2. Convergence 90
5.3.3. Efficiency and Accuracy 92
5.4. Conclusion 97

6. Summary and Perspectives 99

A. Solution of the Characteristic Equation 101

Bibliography 105

List of Figures 115

List of Tables 123

1. Introduction

1.1. Context

Multipactor is a radio-frequency (RF) discharge that occurs in microwave components under vacuum conditions. The phenomenon has been observed in a variety of applications, such as RF satellite payloads [1–4], particle accelerators [5–8], high power RF windows [9–11] and microwave vacuum tubes [12, 13]. The underlined mechanism behind the discharge is an electron multiplication due to secondary electron emission on the device walls. Under certain resonant conditions, the motion of electrons can be synchronized with the RF field. As a result, the multiplication process is self-sustained and an electron avalanche takes place.

Multipactor was first recognized and studied by Philo Taylor Farnsworth in the early 1930's [14]. Taking profit of the electron avalanche of the discharge, Farnsworth developed a high frequency signal amplifier for electronic television systems. His work stimulated the interest of other researchers who performed theoretical and experimental studies for further investigation of the phenomenon and for any other possible applications [15–17]. However, during the last decades, multipactor has triggered intense scientific interest due to the adverse effects it can have on microwave systems operating in vacuum environments. Particular interest has been focused on satellite systems where the high power operation as well as the low pressure environment make them susceptible to multipaction onset. Serious problems may appear, like heat load of the device walls, increase of noise level and detuning of resonant cavities. Such effects may significantly disturb the normal operation of satellite systems or even destroy some internal components [18]. A potential disruption of the connection between the satellite and the terrestrial station would be fatal for the space mission. Undesired effects due to multipacting process have been also reported in particle accelerators [7, 19]. In this case, the discharge results in an electron cloud within the beam pipe that causes various beam instabilities reducing the efficiency of particle accelerators.

It is obvious that multipactor is a key parameter in a variety of vacuum applications. The importance of the phenomenon is raised, even more, by the current trend in the market of satellite communications. The increased demand for high data rates and qualitative services in modern satellite communications leads to the need for higher power operation level, as shown in Fig. 1.1. This trend results in an increasing risk that a multipactor discharge to occur in satellite microwave components. To this end, a significant effort has been devoted in the development of multipactor prediction techniques in order to support the design of new satellite components.

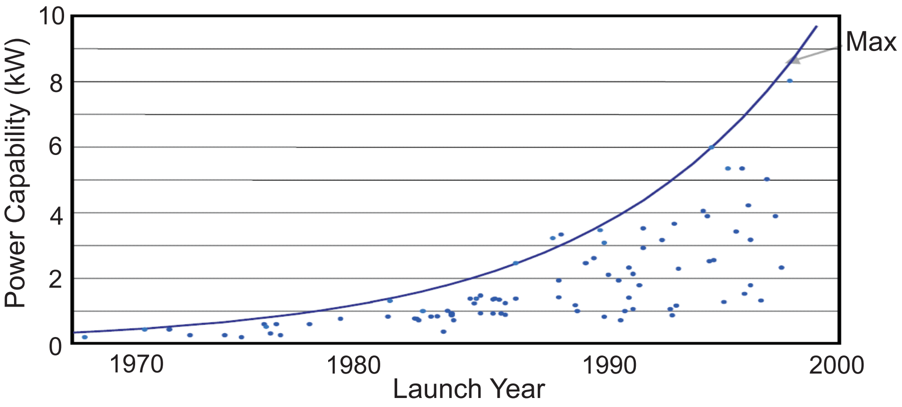

Figure 1.1.: Trend of power capability of GEO satellites. Source: WTEC Panel Report on Global Satellite Communications Technology and Systems, December 1998 International Technology Research Institute Baltimore, Maryland 21210-2699 ISBN 1-883712-51-3

1.2. Motivation

In principle, multipactor evolves in two distinct phases. First, a fast growth of the electron population takes place due to a resonant avalanche mechanism. As the electron population increases, saturation mechanisms disturb the resonant motion of electrons preventing, thus, an infinite growth of the electron population. Therefore, in the second phase, the phenomenon reaches a steady state where the population cannot exceed a certain saturation level.

Both phases are of particular interest. First, multipactor onset, corresponding to the initial phase, reveals if a component is susceptible to the discharge or not. From an engineering point of view, this is the most important aspect regarding the design of microwave structures that are free of the risk of a possible discharge. On the other hand, steady-state provides a global overview of the phenomenon revealing valuable information regarding the side-effects of the discharge, like noise level and heat load. The importance of the second phase is even more augmented by the following feature: the evaluation of the multipactor steady-state can be beneficially exploited in order to experimentally assess the multipactor onset. More specifically, the discharge can be detected by using the third harmonic technique [20], which proposes to search for the third harmonic in the radiated power spectrum of the electron cloud current. Since the intensity of the power spectrum is directly connected with the number of electrons involved in the discharge [21] and the detection is supposed to take place after the steady-sate is reached the radiated power is connected with the saturation level. Linking the predictions to the measurements of the radiated power spectrum will help to define a unique multipactor onset criterion. This rises a particular motivation on investigation the long-term multipactor evolution.

The multipactor steady state has been, mainly, studied assuming two saturation mechanisms: the space charge effect and the detuning of resonant cavities. An additional saturation mechanism is supposed to act in case of dielectric surfaces. More specifically, a surface charge is developed, parallel to the discharge evolution, resulting in a DC-like electric field. This field can significantly affect the electron dynamics and, consequently, the evolution of the discharge.

The presence of dielectrics in multipactor analysis has been, mainly, investigated in the framework of particle accelerators for the cases of ceramic RF windows [11, 22–27] and of dielectric loaded accelerating (DLA) structures [28–30]. However, little is known about multipactor discharges on dielectric surfaces in the framework of space applications. Some works have numerically dealt with multipactor discharge inside a parallel-plate waveguide partially loaded by a dielectric slab [31, 32]. Results revealed an interesting self-extinguishing mechanism that acts in the long-term evolution of the phenomenon. However, these studies were based on a critical simplification by neglecting the induced charges on the metallic walls due the surface charge on the dielectric. It has been reported that the charges induced on the metallic walls can significantly affect the steady state of the discharge [33]. This adds a strong motivation in studying the problem by including the effect of the induced charges.

1.3. Objectives

The main objective of this thesis is to investigate the long-term multipactor evolution in the presence of dielectrics. For this purpose, a model able to consider the saturation mechanisms has to be applied, including the effect of the space charge. Space charge implies the mutual interaction between electrons. This results in a huge complexity of $O\left(N^2\right)$, where N is the number of electrons. Since the electron population increases exponentially during the multipactor onset, N is expected to be in the order of several magnitudes and, consequently, special simplifications has to be done. To this end, a systematic approach is ventured able to gradually study multipactor starting from a fast, but rough, overview of the phenomenon and ending in robust and demanding predictions.

Briefly, the objectives of this thesis are summarized as follow:

- A fast numerical technique in order to obtain a first overview of the multipactor onset by deriving the susceptibility zones (see Chapter 3). For this purpose, a generalized 1D technique is explored in order to extend the analysis from the fundamental parallel plates case to any 1D-like configuration, e.g. coaxial lines.

- A 3D multipactor technique able to consider the stochastic behavior of the secondary emission. Taking into account the statistics of the secondary emission as well as the 3D motion of electrons the multipactor onset will be accurately approached. The 1D technique can supplement nicely the robust 3D analysis by providing fast estimations for the most likely cases for which multipactor occurs.

- Investigation of the long-term multipactor evolution in the case of parallel plates loaded by a single dielectric slab. For this purpose, the above described techniques are properly modified in order to include the space charge effects as well as the effect due to the surface charge on the dielectric. In order to consider the effect of the induced charges, special attention is devoted to the 3D case where a Green Function (GF) able to provide the self-consistent field on an electron due to its induced charges is explored. Since image series fits well in this feature, a novel image method for the GF evaluation in the case of multilayer shielded media is ventured.

1.4. Outline and Original Contributions

This section summarizes the contents of the chapters of this thesis and links them together with the framework of investigation of the long-term multipactor evolution in the presence of dielectrics. The original contributions performed during this thesis are also included in the corresponding chapters.

Chapter 2

This chapter reviews the physics of multipactor discharge. The two guided mechanisms of the discharge, namely the secondary emission and the resonant motion of the electrons, are described in detail. The chapter serves a solid theoretical background of multipactor required before continuing with the modeling of the phenomenon in the next chapters.

Chapter 3

A generalized technique able to analyze multipactor in any 1D configuration is developed. The chapter contains two main parts. In the first, the single electron approach is reviewed, underlying its fundamental assumptions. Then, based on the single electron model, a theoretical analysis is presented for the parallel plates case, in order to get a physical insight to the multipactor mechanisms. As a result, the multipactor chart that depicts the susceptibility zones for different multipactor modes is obtained. Special emphasis is given to explaining the mechanisms affecting the multipactor threshold. The second part of the chapter deals with the proposed generalized technique. After describing it, the proposed numerical method is validated through comparisons with theoretical and numerical results as well as with measurements. The technique is, then, applied in order to study two topics of particular interest in multipactor analysis: first, the effect of electric reflection of impact electrons on the multipactor onset and, second, multipactor effect in coaxial lines focusing on the effect of the characteristic impedance on the lower multipactor threshold. The developed 1D technique is used in Chapter 4 in order to investigate multipactor in the presence of dielectrics.

Original Contributions

- **Generalized single electron model:** A generalized model is developed able to simulate multipactor in any 1D configuration.

- **Effect of elastic reflection emission mechanism on the multipactor onset:** By applying the developed technique, the effect of the elastic reflection on the multipactor onset has been investigated using realistic secondary emission yield models. As a conclusion, it has been shown that the lower multipactor threshold corresponding to the 1^{st} order multipactor mode is not affected by the elastic reflection mechanism.

- **Multipaction in coaxial lines, effect of the characteristic impedance:** In this work, multipaction in coaxial lines has been investigating focusing on the effect of the characteristic impedance on the lower multipactor threshold.

Chapter 4

The long-term multipactor evolution inside a parallel plates waveguide partially loaded by a dielectric slab is investigated. For this purpose, the space charge effect as well as the surface charge on the dielectric are taken into account. The 1D technique developed in Chapter 3 is properly modified in order to consider the induced charges on the metal plates. A deeper insight of the phenomenon is provided by a 3D model able to consider for the statistics of the secondary emission. The electric field due to the induced charges in the 3D analysis is efficiently evaluated through an image series as presented in Chapter 5.

Original Contributions

- **Long-term multipactor evolution in the presence of dielectrics:** The multipactor steady state in parallel plates waveguides partially loaded by a dielectric slab has been investigated considering the induced charges on the metal surfaces. For the first time, a saturation stage in the investigated configuration is reported.

Chapter 5

A novel technique for image series derivation in multilayer shielded media is presented. The proposed technique is validated through comparisons with the well established methods of Sommerfeld integration and modal series expansion. Through numerical examples, the efficiency of the proposed image series is studied. The image series is efficiently incorporated in the 3D analysis of Chapter 4, in order to evaluate the electric field due to the induced charges.

Original Contributions

- **Image method for the electrostatic Green Function in multilayered shielded media**

Chapter 6

This chapter summarizes the concluding remarks and proposes future research directions within the topics covered in this thesis.

2. Multipactor Review

2.1. Introduction

Multipactor effect is a RF breakdown phenomenon which is normally observed in microwave components under vacuum or low pressure conditions. In brief, the phenomenon starts when a free electron in a vacuum cavity, accelerated by a RF field, impinges on a surface (metallic or dielectric) of the device. Depending on the impact energy, this collision can cause the emission of two or more secondary electrons from the surface. Under certain resonance conditions, these new electrons may in turn be accelerated and impinge on the same or another surface producing, thus, more electrons. If this process is sustained for a few RF cycles, it may lead to an avalanche phenomenon which results in a dense cloud of free electrons inside the device.

The aim of this chapter is to provide a review on the physics behind the phenomenon. After introducing the fundamental concept of multipacting, the main physical mechanisms responsible for multipactor discharge are discussed, i.e. the secondary emission phenomenon and the resonant motion of electrons, in Sections 2.3 and 2.4, respectively. The chapter ends with a description of the main saturation mechanisms, responsible for the long-term characterization of the phenomenon, in Section 2.5.

2.2. Multipacting

As already mentioned, the multipactor effect can occur inside a RF device under vacuum conditions when free electrons impact the surfaces in resonance with the alternating field causing the emission of more electrons. Fig. 2.1 illustrates the evolution of the discharge in the simple case of two parallel plates. First, a free electron starts moving from the lower surface continuously accelerated towards the upper conductor due to the electric field. When this electron hits the conductor it is assumed to have sufficient energy so that two new electrons are emitted. Since this collision occurs when the field reverses direction, the emitted electrons are in turn accelerated towards the opposite surface. Again, these electrons traverse the gap in a time that amounts to one half of the signal period and impact the lower conductor with enough energy for secondary emission. If this procedure continues the population of the particles will exponentially grow. At the end, an electron cloud will be created inside the device.

As it becomes obvious, the two main mechanisms causing multipacting, i.e. the process that yields to the exponential growth of the electron population, can be summarized as follows:

- *Resonant motion of the electrons.* The electrons are emitted from a cavity wall, they are driven by the electromagnetic field and return back to the same point after a integer number of RF cycles.

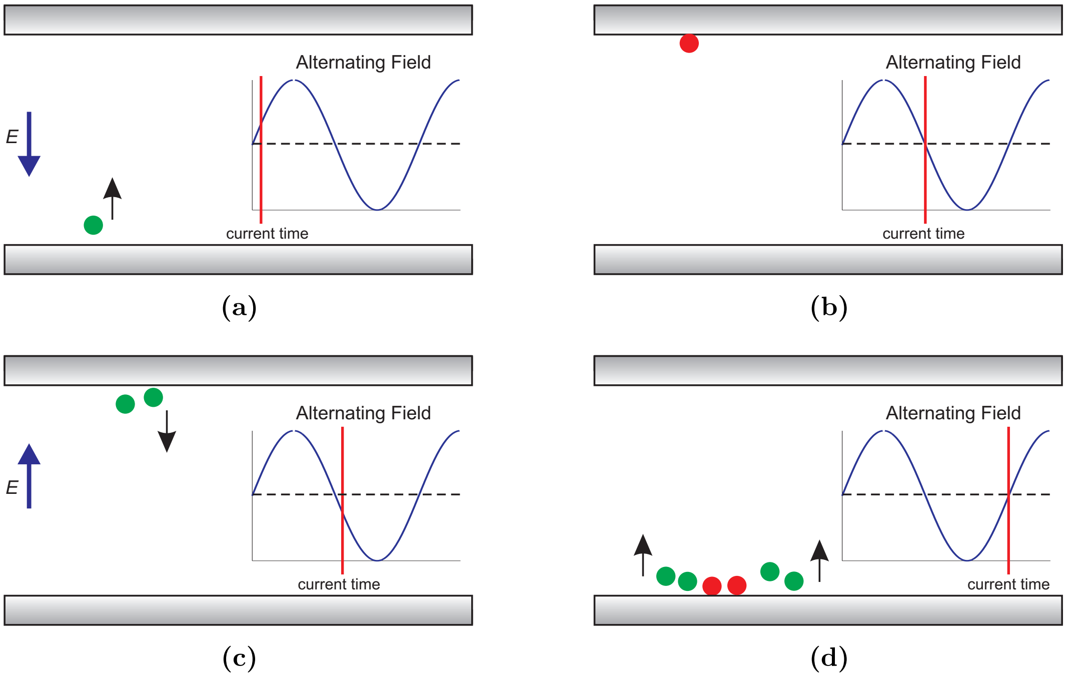

(a) (b) (c) (d)

Figure 2.1.: Multipacting process. (a) A free electron is accelerated by the electric field. (b) The electron hits the surface and (c) causes the emission of two secondary electrons. The field reverses direction and the new electrons are accelerated towards the opposite conductor. (d) The procedure continues.

- *Secondary emission of more than one electrons.* The electrons hit the cavity walls with sufficient energy so that they provoke the emission of two or more electrons.

In reality, these two mechanisms, as ideally described above, can only roughly take place due to the complex nature of the secondary emission phenomenon and due to asymmetries appearing in realistic microwave cavities, too. Both topics of Secondary Electron Emission and resonant motion are discussed in more detail in the following sections

2.3. Secondary Electron Emission

Secondary electron emission (SEE) refers to the phenomenon that takes place after an electron impact on a surface, from which additional electrons are emitted [34]. The phenomenon has been extensively studied theoretically [35–40], experimentally [41–45] and numerically [46–48]. Secondary electron emission can be briefly described as follows: when an electron bunch impinges on a surface a portion of the electrons is elastically reflected while the rest penetrates into the material. Some of these electrons scatter from atoms inside the material, are reflected back and finally are re-emitted from the surface. These are the so-called 'rediffused' or 'inelastically backscattered' electrons [3, 49]. The rest of the penetrated electrons interact in a more complicated way with the material atoms and they can cause the excitation of other electrons, the so-called 'secondary electrons' [49]. If these interactions take place close to the surface some of the excited electrons are able to escape from the material and are emitted. Of course, apart from these mechanisms, there is also the possibility that some electrons are absorbed without causing any emission, a phenomenon that yields to the decrease of the free electron population. The three mechanisms of emission, that is elastic and inelastic reflection as well as generation of true secondaries, are summarized in Fig. 2.2. Although backscattering (elastic or inelastic) of electrons is in a strict sense not an emission of true secondaries but only a re-emission of the primary electron, the term SEE is commonly used in a way that implies all the mechanisms of emission. This convention is also followed in this thesis.

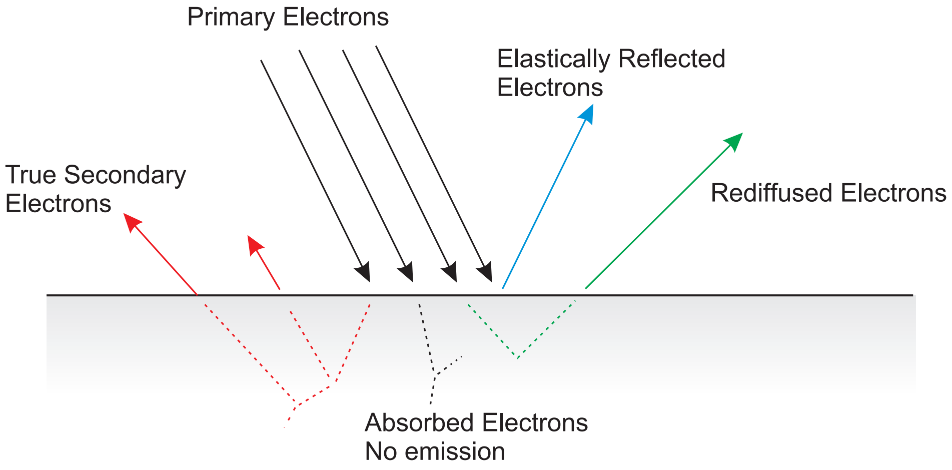
Primary Electrons
Elastically Reflected Electrons
True Secondary Electrons
Rediffused Electrons
Absorbed Electrons No emission

Figure 2.2.: Emission mechanisms occuring after impact of an electron bunch impact on a surface.

2.3.1. Secondary Emission Yield

One of the most important aspects in SEE study is the secondary emission yield (SEY), also known as secondary electron emission coefficient (SEEC). Secondary emission yield represents the average ratio between emitted and impacting electrons on a material surface. Fig. 2.3 depicts qualitatively a typical SEY as a function of the impact energy of the primary electron. As it is shown, the three different emission mechanisms contribute to the total SEY in a different way.

Starting the discussion with the total SEY curve, which presents the most practical importance, there are two crucial points of impact energy, E_1 and E_2, called the first and the second crossover point, respectively. For these two impact energies the total SEY equals 1, whereas between them it is always greater than 1, something that means that the number of the emitted electrons are in average larger than the number of primary electrons. This region is of great importance in multipaction analysis since discharges imply multiplication of electrons by secondary emission, that is collisions with impact energy, E_{imp}, such that $E_1 < E_{\text{imp}} < E_2$. Between the two crossover points the total SEY curve reaches a maximum value $\sigma_{\max}$ for a corresponding impact energy $E_{\max}$ while outside this region it takes values less than unity.

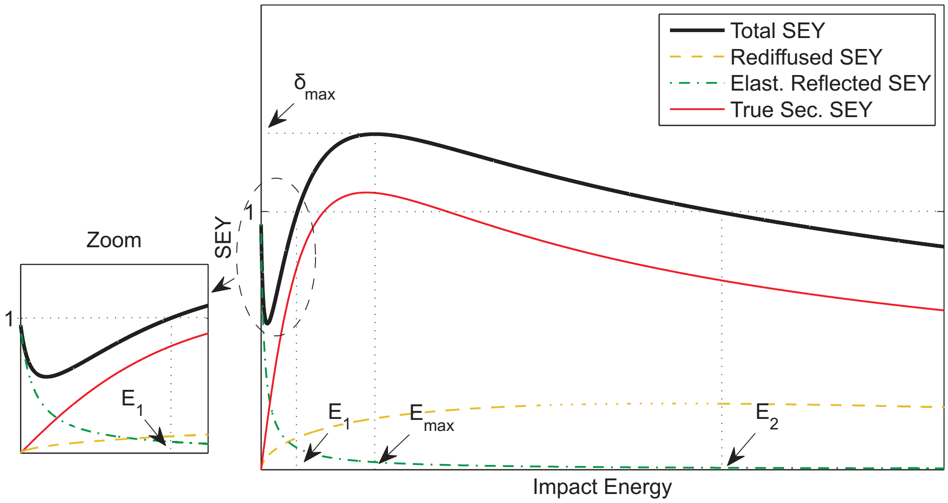

Figure 2.3.: A typical Secondary Emission Yield (SEY) curve as a function of the impact energy. The total SEY results from the contribution of the true secondary, of the inelastically backscattered and of the elastically reflected electrons.

In order to better understand the behavior of the total SEY one should also examine the contribution of the individual emission mechanisms. At very low impact energies the secondary emission is mainly dominated by the elastic reflection. In particular, a SEY close to 1 implies that almost all the low energy electrons are reflected back [50]. As the impact energy increases, the other two emission mechanisms start to appear since some electrons penetrate into the material. As it is shown, the generation of true secondaries becomes soon the dominant emission mechanism, thus, making the total SEY follow a similar behavior. For low energies, there is an absorption process because many of the penetrated electrons do not have sufficient energy in order to excite the emission of new electrons. However, a continuously augmentative tendency is observed for the number of the emitted secondary electrons yielding to a total SEY greater than 1 after the first crossover point. This behavior continues until the total SEY reaches a peak at E_{max}. After that, the total SEY decreases monotonously and at the end it becomes less than unity after the second crossover point. This can be explained as follows: since the impact energy is too high the primary electrons penetrate too fast deeply into the material before they manage to transfer enough energy to potential secondaries close to the surface. The secondaries are mainly generated far from the boundary and at the end they do not manage to escape.

Apart from the impact energy, the SEY depends also on the incident angle of the primary electron. It has been observed that the secondary yield can increase with oblique incident angles, especially for high impact energies as Fig. 2.4 shows. The explanation comes from the fact that in case of oblique incidence the penetration depth gets smaller allowing, thus, the impact electrons to interact more with material atoms which are close to the surface [51].

Secondary emission also varies with regard to the material properties as well as to the surface conditions like the ‘roughness’. In general, dielectric surfaces have higher values of

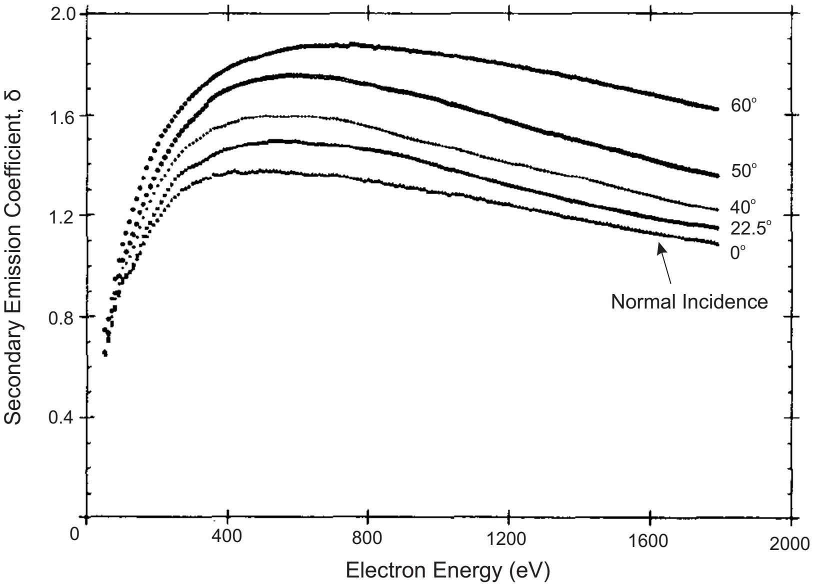

Figure 2.4.: SEY curve as it was measured on a molybdenum sample for several incidence angles [51].

SEY than metallic ones. On the other hand, a rough surface yields to lower SEY since there is an increased probability for an emitted electron to be immediately reabsorbed by a neighbor peak of the rough surface. Moreover, the presence of contaminations, like dust, can also affect the SEY behavior.

2.3.2. Emission Energy Distribution

Fig. 2.5 illustrates a representative example of the energy distribution curve (EDC) based on measurement results [49]. As it is shown, the energy spectrum can be separated in three areas which are related with the different emission mechanisms. The peak close to the same energy as the primary energy E_{PE} is due to the elastically reflected electrons, which are emitted with almost zero energy losses. Rediffused electrons correspond to the mid-energy area. They lose an amount of their impact energy that follows a quite uniform distribution. Finally, the true secondary electrons are distributed in the low-energy area, around a peak that corresponds to their most probable emission energy.

The above described behavior of the energy distribution has been also reported in other studies [43, 52]. It is assumed to be similar (the shape of the spectrum) for relatively high primary energies, greater than 100 eV. In general, the three secondary emission mechanisms cause emission in different energy ranges. However, the ranges of the true secondaries and the rediffused electrons are not clearly separable since there is a smooth transition of the curve between the corresponding areas. In fact, these two areas may be overlapped. However, it is conventionally assumed that the energy range below 50 eV corresponds to the true secondary electrons. It has been found that for high primary energies the true secondaries

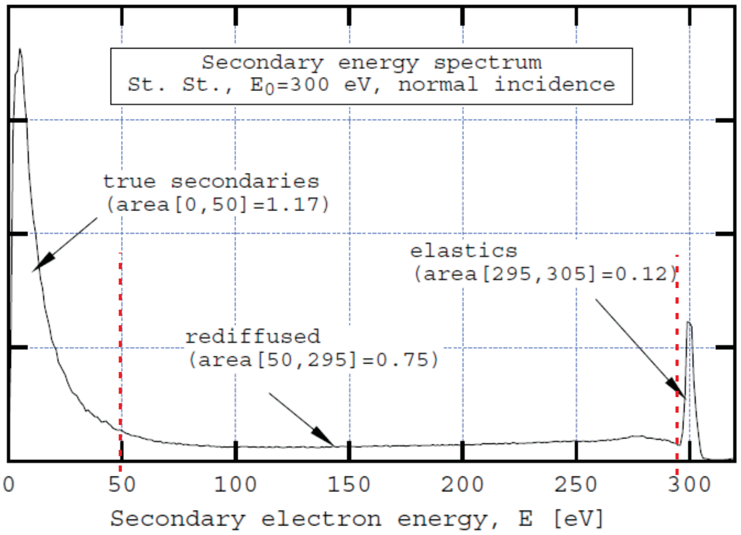

Figure 2.5.: A sample of the emission energy spectrum extracted from [49]. The primary energy is $E_{\mathrm{PE}} = 300\mathrm{eV}$. The areas that correspond to each emission mechanism are separated by the red dashed lines.

energy distribution is independent of the impact energy whereas they achieve a peak at an energy of a few eV (around 5 eV).

Now, it is worth to examine what happens at low impact energies. In fact, this is a subject that has not been intensively studied since the very-low primary energies are difficult to treat through experiments. Cimino *et al* performed measurements examining the behavior of the EDC for very-low impact energies [50]. Fig. 2.6 presents results from their work for four different cases with different primary energies. First, when the primary energy is high ($E_{\mathrm{PE}} = 112$ eV), the spectrum has a form like the one previously described and the three areas can be clearly distinguished. As it was expected, when the primary electron impacts with lower energy the three areas are getting closer and at the end they are mutually overlapped. The ranges of rediffused and true secondary electrons cannot be separated any more, whereas the peak due to the elastic reflection becomes more and more intense. The last comes in agreement with the SEY data in Fig. 2.3 where, as has been already mentioned, for very low impact energies elastic backscattering dominates the secondary emission.

2.3.3. Angular Distribution of the Emitted Electrons

The true secondary electrons are emitted to all directions according to the cosine law [37], which means that the emission angle is independent of the primary incident direction. The cosine law implies that the secondary electrons are most probable to be emitted towards the surface normal direction and almost impossible towards grazing angles, as Fig. 2.7 shows. Regarding the elastically reflected electrons, they can also be emitted to all directions. How-

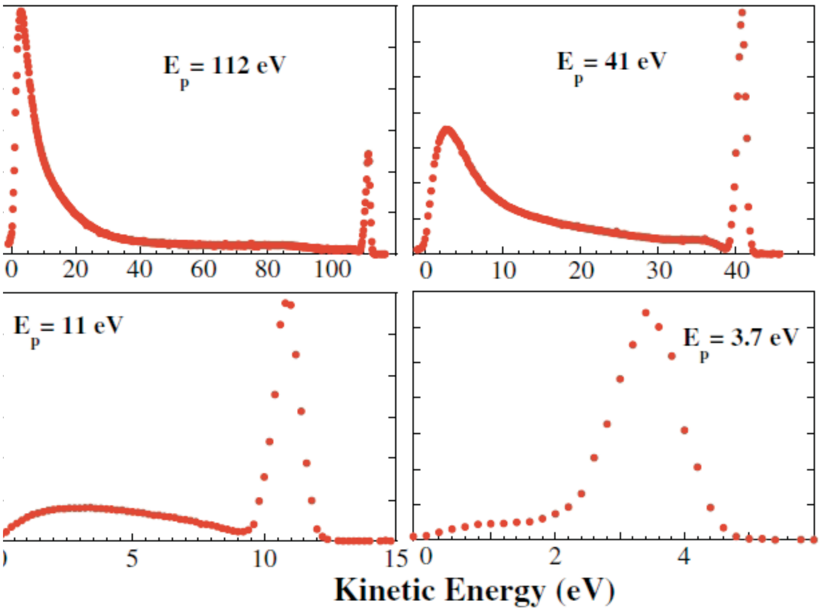

Figure 2.6.: Measured EDCs for different primary energies extracted from [50].

ever they have a more complicated angular distribution that is related with the impact angle. In general, they prefer a mirror-like reflection direction. Rediffused electrons follow a similar angular distribution as the elastically reflected electrons.

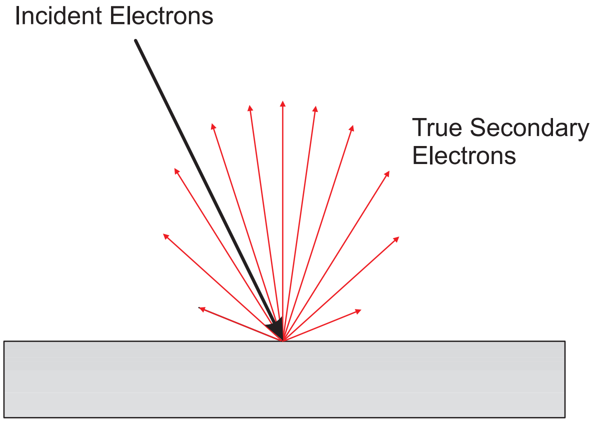

Figure 2.7.: Angular distribution of the true secondary electrons. The length of each arrow is proportional to the number of the emitted electrons.

2.4. Resonant Motion

As already mentioned, one of the two main mechanisms of multipacting is the resonant motion of the electrons which is responsible for sustaining the secondary emission process after electron collisions against the device walls. In microwave components, the motion of the electrons is forced by the applied, periodic, RF field. However, a perfect periodic motion of the electrons is impossible to occur in reality. In fact, it is the electron impacts on the device wall that prevent a periodic motion. Due to the stochastic nature of the secondary emission phenomenon, the secondary electrons are emitted with a random initial velocity following certain energy spectrum and angular distributions, as described in the previous section. However, despite the randomness of the emission velocities, the electrons tend to follow a resonant-like motion due to a mechanism called 'phase-focusing', as it will be discussed later.

2.4.1. Resonance Conditions

In order to study the conditions required for a resonant motion of electrons, a consideration about the initial velocity of the emitted electrons has to be done. The most common approaches found in the literature are those ones of 'constant-u' (or also referred to as 'constant velocity') [53] and of 'constant-k' [15]. The 'constant-k' approach considers a constant ratio (k) between the primary and the secondary emission electron velocities. However, this assumption lacks of a physical explanation, since the emission velocity of the secondary electrons (true secondary electrons) is known to be highly independent from the impact velocity, as discussed in 2.3.2. On the other hand, the constant-u approach assumes that the emitted electrons leave always the surface with a constant velocity. Despite the poor statistical representation of the emission energy spectrum, the constant-u approach is physically consistent with the fact that the impact and emission velocities are almost uncorrelated. For this reason, in this section, the secondary electrons are assumed to be emitted with constant energy.

Considering the basic example of parallel plates, the most obvious resonant condition states that the electrons, driven by the electric field, should traverse the gap in an odd number of half RF cycles. This ensures that the emitted electrons on the opposite plate are subject to the same conditions in reverse, since the RF field changes polarity every half period. Therefore, the electrons return back to the same electrode in a integer, odd, number of periods, $N = 1, 3, 5 \cdots$. Each number N, i.e. the number of half-periods needed for the electrons to traverse the plates gap, corresponds to a certain resonant motion which defines the corresponding 'multipactor order' or 'multipaction mode', as will be discussed in the next chapter. For the moment, let us use the terms 'resonance-order' and 'resonance-mode', instead. Figure 2.8 shows some representative motions corresponding to different order of resonance.

A resonance motion can be only achieved for certain parameters of dimensions (plates gap), RF field (amplitude and frequency) and initial emission velocity. Figure 2.9 depicts an example about the conditions needed for the 1^{st} order resonance. Then, if the resonant conditions are satisfied, there is a favorable phase difference between the emission time and the time that the RF field changes polarity for which the electrons follow a periodic motion. This can be clearly seen in Fig. 2.8a where the electrons are emitted before the electric field changes polarity

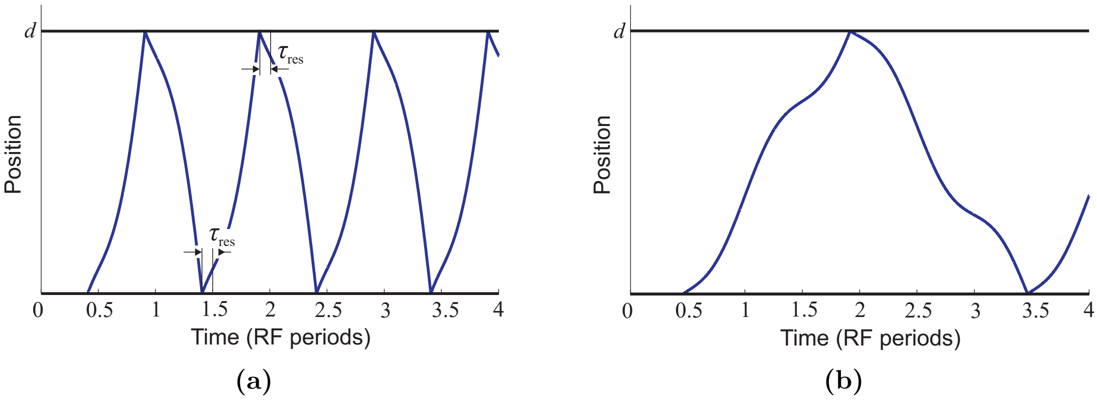

Figure 2.8.: Periodic motions of electrons in parallel plates configuration: (a) 1^{st} resonance order, (b) 3^{rd} resonance order. The electrons are emitted with a time difference τ_{res} with respect to the moment at which the electric field changes polarity. i.e every half period. The corresponding resonant phase is equal to $\varphi_{res} = \omega\tau_{res}$, where ω is the angular frequency of the applied RF field.

with a negative time shift τ_{res}. The corresponding phase shift is called 'resonant phase'.

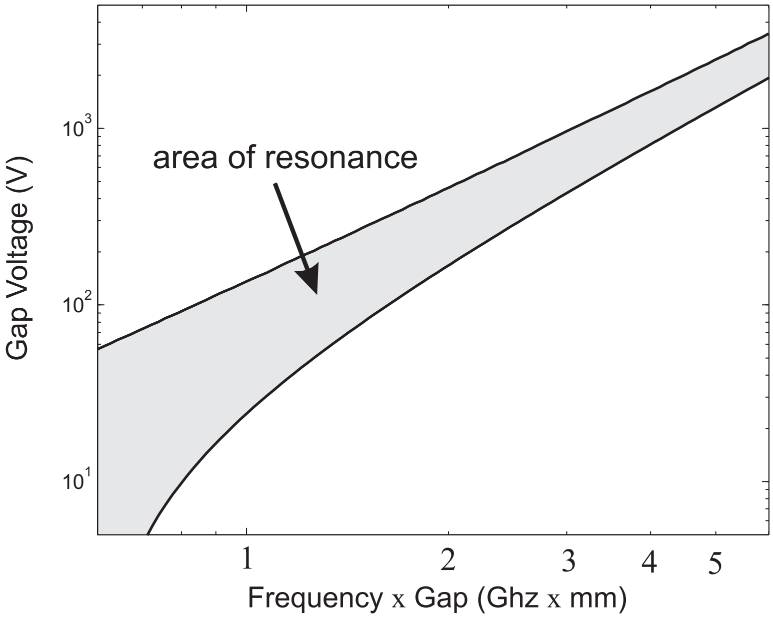

Figure 2.9.: Conditions for achieving 1^{st} resonance order in parallel-plates configuration. A constant emission velocity equal to $u_0 = 4\,\text{eV}$ is considered.

Up to now, the resonant conditions has been discussed under the assumption that the electron motion is periodic and symmetric with respect to the parallel plates. However, resonance can be achieved in a more general manner without the demand for symmetric motion. For instance, in the parallel plates configuration some additional resonant modes, called ‘hybrid modes’, have been identified [54]. These modes, correspond to periodic motions under the condition that the two-way transit time of electrons must be an integer number of RF cycles. i.e. $\tau_{12} + \tau_{21} = kT$ where τ_{12} and τ_{21} are the one-way transit times and T the RF period. Contrary to the classical symmetric modes, in the hybrid modes the transit times τ_{12} and τ_{21} can be different, describing, thus, a broader range of resonant manners. Apart from parallel plates, resonance can also occur to more complex configurations with non-uniform electric field, that is the case commonly met in realistic microwave components. In such cases, i.e. when the RF field is non-uniform, a single-side resonant motion is also possible, like the example depicted in Fig. 2.10.

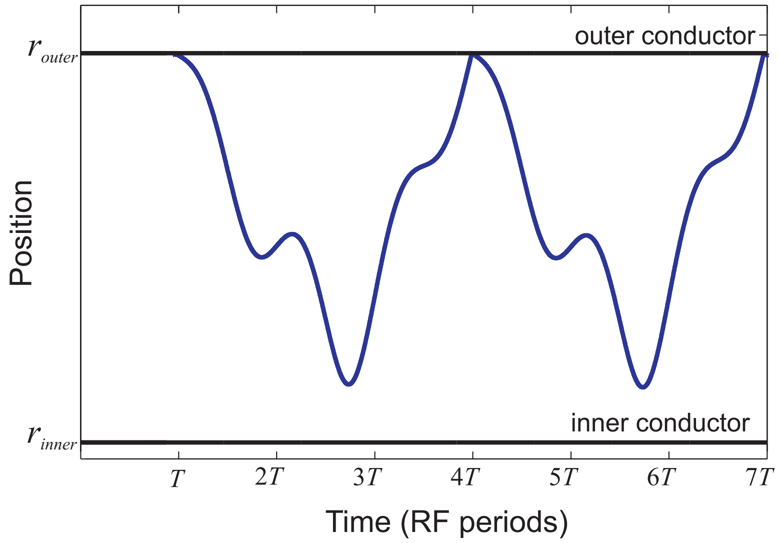

Figure 2.10.: Single side resonant motion in a coaxial cable. The following parameters are considered: $r_{outer}/r_{inner} = 5.3$, $V = 150$ V and $f = 65$ GHz where r_{inner} and r_{outer} is the radius of the inner and the outer conductor, respectively, V the gap voltage between the conductors and f the frequency of the applied RF field. A constant emission velocity equal to $u_0 = 4\,\text{eV}$ is considered.

2.4.2. Phase Focusing

In order an electron to follow a periodic motion, it must be emitted with the resonance phase, as defined in the previous subsection. Due to the delays between the emission and the impact of electrons and due to the spread in the initial velocities, the emitted electrons acquire a phase error. However, due to a phase focusing mechanism this error may decrease as the electron traverses the electrodes gap.

A qualitative insight about how the phase focusing mechanism acts on the electrons motion is given through the two following examples, illustrated in Figs. 2.11 and 2.12. First, let us assume that an electron is emitted with a phase error with respect to the resonant phase. As

Fig. 2.11 depicts, the motion is very quickly synchronized with the electric field, following, thus, the exact resonant motion. As can be seen in Fig.2.11b, the phase converges very fast to the resonant phase. The second example considers the more realistic case where the emission velocity after each impact is random. For demonstration reasons, the emission velocity is assumed to follow a normal distribution with a mean value equal to u_0, i.e. the constant initial velocity in the case of perfect resonant motion. As can be seen in Fig. 2.12a the electrons follow a resonant-like motion, close to the motion expected by considering a constant emission velocity. Regarding the phase at the impact events, it is oscillating around the resonant phase, bounded within a certain phase range, as Fig. 2.12b illustrates.

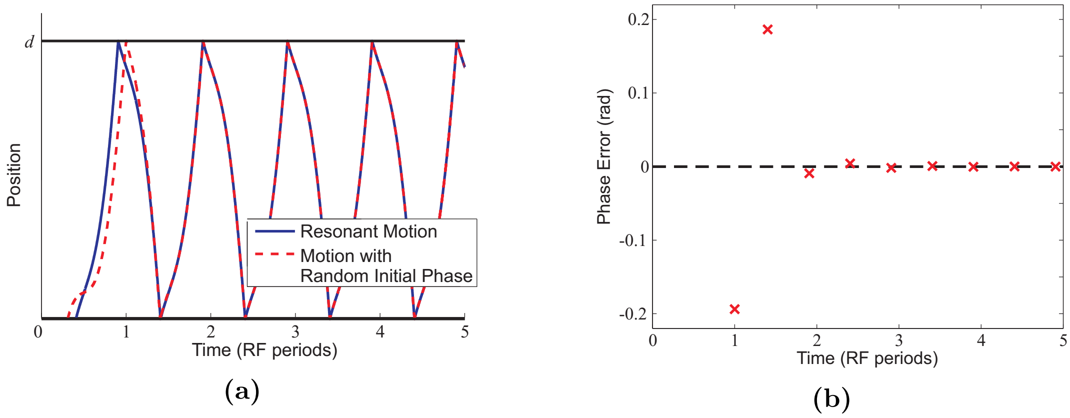

Figure 2.11.: Phase focusing mechanism when the electron is emitted with a initial phase error considering constant emission velocity: (a) electron motion, (b) phase error at the impact events.

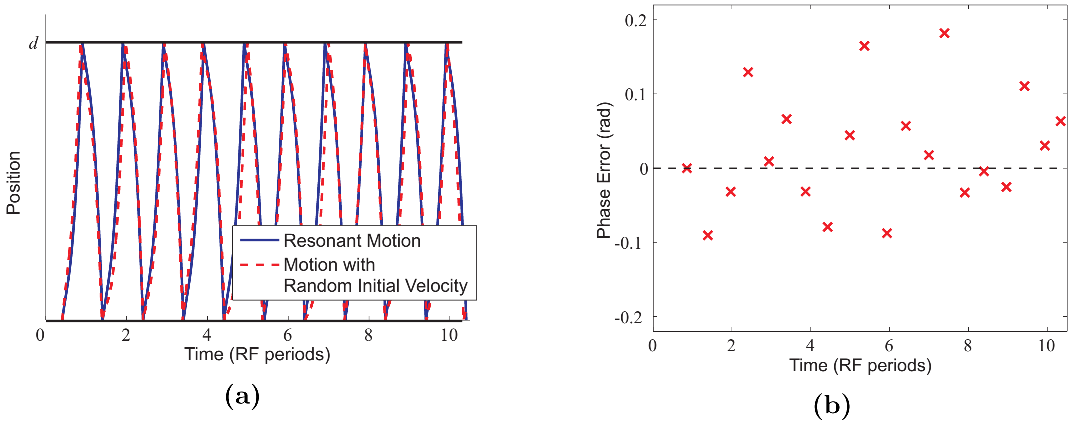

Figure 2.12.: Phase focusing mechanism when the electron is emitted with a random initial velocity that follows a normal distribution with $\mu = u_0 = 4$ eV and $\sigma = 0.3$ eV: (a) electron motion, (b) phase error at the impact events.

Each resonant motion is characterized by a specific resonant phase and a corresponding phase range, around the resonant phase, where the phase focusing mechanism can take place.

Outside this range, which is called ‘phase-focusing range’, the phase error grows after each transit and the electrons tend to follow unstable trajectories. This results in impact events with low impact energy and, consequently, in the absorption of the electrons. Under certain conditions, the phase focusing range can be very small or even equal to zero. Under such circumstances, although the resonant conditions are satisfied, multipacting cannot take place in realistic conditions since the spread of the emission velocities leads to unstable motion of electrons.

2.5. Saturation

In a microwave component, once the conditions are favorable to the multipacting process, the multipactor discharge may start, resulting in a rapid increase of electron population. Since the growth is, typically, exponential, due to the resonant motion of electrons and the multiplication process of secondary emission, the number of electrons reach high values after few RF cycles. However, there are physical mechanisms that act against multipacting and prevent an infinite growth of electron population. These mechanisms, referred to as ‘saturation mechanisms’, act like a feedback in a control system and keep the electron population, almost, constant to a saturation level. So far, two main saturation mechanisms have been described in the literature: the space charge effect [33] and the detuning of resonant cavities [55].

The space charge effect involves two mechanisms which can affect the motion of electrons: first, the mutual interaction between the electrons, through the Coulomb force, and, second, the interaction between the electrons and the induced charges on the devices walls. As the electrons approach each other they tend to repel due to the coulombian field. In the early stage of the discharge this repulsion does not affect the multipactor process. The reason is that the coulombian field is much smaller than the applied RF field, since the electron density is low. However, as the population increases, the mutual repulsion between electrons becomes more intense, affecting the electron dynamics. In addition to this, the electrons tend to be attracted towards the device walls by the charges induced on them or equivalently, by their image charges. At the end, the electrons acquire a significant phase error which cannot be compensated by the phase-focusing mechanism. Consequently, some of them are absorbed on the device walls and the population reaches a equilibrium steady state.

Detuning can be an alternative saturation process in cavity resonators with high quality factor (Q-factor) [55]. Due to high Q-values, the electric field amplitude is high and a multipactor discharge is likely to occur. Then, the moving electrons induce a wall current which in turn loads the resonator. This means that the cavity will be detuned and, consequently, the electric field strength will decrease. By this way, the multipacting process is self-suppressed and the electron population reaches a steady state. Both detuning and space charge effects can simultaneously take place in a cavity. However, for high Q-values detuning becomes the dominant saturation mechanism, as reported in [55].

In addition to the above mentioned mechanisms, another physical process may affect the long-term evolution of multipactor in structures with dielectric surfaces. In particular, any dielectric surface is charged positively after the emission of secondary electrons. In case of a multipactor discharge, this yields an electric field which can, significantly, disturb the resonant motion of electrons. Contrary to the previously described saturation mechanisms, this process depends on the impact events on the dielectric surfaces and not on the electron cloud density. The following particular process may arise: the electrons are attracted on a dielectric surface, due to the positive surface charge, and provoke secondary emission on it. On the other hand, due to this attraction, the electrons may impact on other, metallic surfaces with low energy and, consequently, be absorbed. If the absorption rate is more intense than the rate of the secondary emission the whole process yields in a decrease of the electron population. As reported in some works [31, 32], under these circumstances, the electron cloud may disappear while the dielectric surface remains charged.

2.6. Summary

This chapter reviewed the physics of multipactor discharge. The two major mechanisms responsible for multipacting, namely the secondary emission and the resonant motion of the electrons, have been described in detail. In addition, saturation mechanisms have also been introduced providing a global overview of the long-term multipactor evolution. The chapter serves a solid theoretical background of multipactor required before continuing with the modeling of the phenomenon in the next chapters.

3. The Single Electron Model

3.1. Introduction

The ‘single electron model’, or also referred to as the ‘mono-energetic model’, has been widely used in early studies of multipactor discharge in order to understand the physical mechanisms of the phenomenon as well as to establish the basic multipaction theory. The model originates from the study of multipactor in the case of two infinite parallel plates. As revealed by the term ‘mono-energetic’, the model is based on the assumption that the electrons move simultaneously between the plates, all with the same speed. As a consequence, they compose an infinitely thin sheet which can be represented by a single, effective, electron.

The single electron approach simplifies notably the analysis of multipaction in infinite parallel plates. Although such a configuration is met approximately only in few realistic applications, it attracts intense interest, especially for theoretical studies of the discharge. What makes it appealing is the fact that the electron motion can be expressed in analytical form. By applying the single electron approach, closed analytical formulas can be derived regarding the conditions required for multipacting. Moreover, the single electron analysis provides a physical insight into the multipactor phenomenon through, for instance, the study of the resonant modes or the phase focusing mechanism.

Apart from theoretical studies, the single electron model presents significant interest from a practical point of view, too. Through the well-known multipactor chart, one can get an overview about the operation zones in which a microwave component is susceptible to multipactor discharge. The single electron model can be applied as a first approach in order to rapidly obtain the multipactor chart which can be used as an engineering tool for designing components that locally resemble the parallel plates configuration, e.g. a rectangular waveguide with small height to width ratio. Several studies have been performed on deriving analytically the susceptibility zones for the case of parallel plates. Indeed, some of them [17] have been used as a basis for deriving standardization for multipactor avoidance [2].

In addition to the parallel plates problem, the applicability of the single electron approach can be extended to any other configuration that, fairly, resembles a 1D geometry. Such an example is the coaxial line. Considering the fundamental TEM mode, the electric field is unidirectional, radially distributed with azimuthal symmetry. Therefore, the electrons can be assumed that travel towards the radial direction, composing a cylindrical sheet which oscillates between the inner and the outer conductor. Contrary to the parallel plates case, the electric field is not uniform, regarding the radial coordinate, and the electron motion cannot be expressed in an analytical, closed form. Under some approximations, some authors performed qualitative studies on multipaction in coaxial lines by applying the single electron model [56]. However, in order to derive closed, quasi-analytical expressions, their work is limited by the assumption that the secondary electrons are emitted with zero energy which is in contrast to the experimental data related with the secondary emission spectrum, as discussed in 2.3.2. To the author's best knowledge, there are no other works that apply the single electron model further to the classical parallel plates configuration.

Here, a generalized method which extends the applicability of the single electron approach to any 1D configuration is presented. The electron motion is efficiently evaluated by a numerical integrator able to account for any 1D electric field distribution. Apart from the parallel plates case, by applying the proposed numerical technique the multipactor chart can be rapidly derived for coaxial lines taking into account the exact, analytic field distribution. Moreover, multipactor studies can be performed even for more complex geometries, which locally resemble 1D configurations, using realistic field distributions as obtained by full wave analysis.

3.2. Model Assumptions and Applicability

As mentioned before, the single electron model originates from multipactor studies in the case of parallel plates. The basic principle behind the model is that the electrons are all travelling with the same speed, composing, thus, an infinitely thin electron sheet between the plates. This, mainly, entails two assumptions. First, the electrons are all moving in one direction, meaning that they are forced by a unidirectional RF electric field. Second, the secondary electrons are all emitted with the same energy, towards the normal direction with respect to the surface.

Both assumptions can be fairly considered valid for the case of a multipactor discharge in infinite parallel plates. In particular, considering the fundamental TEM mode, the electric field is unidirectional and normal to the surfaces, forcing, thus, the electrons to follow a 1D motion. Even if the secondary electrons are emitted in a direction, slightly, different to the normal one their motion is aligned with the 1D electric field. On the other hand, despite the spread of the initial velocities, the secondary electrons tend to converge to resonant motions with fixed (monoenergetic) emission velocity due to the phase focusing mechanism, as described in Chapter 2.

Due to its 1D monoenergetic nature, the single electron model neglects the magnetic field force as well as the mutual repulsion between the electrons, two mechanisms that could potentially affect the electron motion. As a first approach, the effect of the magnetic field can be neglected by assuming that the velocity of electrons is much lower than the speed of light. If this happens, which is the most likely case in multipactor regimes, the motion of the electrons is extensively dominated by the electric field force and, therefore, the effect of the magnetic field is almost negligible. On the other hand, the space charge that includes the mutual repulsion between electrons starts to affect the multipactor evolution when the population approaches the saturation stage. Hence, focusing only on the beginning or onset of the multipacting process (electron avalanche/no electron avalanche), the space charge can be safely omitted in the analysis of the breakdown.

Appart from the parallel plates, the conditions assumed in the single electron model are also met in other, more realistic structures with a unidirectional-like electric field. Such cases include rectangular structures, like waveguides and filters, with a small height to width ratio.

Considering the fundamental mode, the electric field in the central area of the rectangular cavity resembles the one of the parallel plates. Since the electric field is stronger in the central area, the discharge is most probable to occur there and, hence, a local 1D multipactor analysis can be performed as a first approximation. The single electron model can be applied in geometries with cylindrical symmetry, too. Apart from the case of an infinite coaxial line, more complex cylindrical structures can be approached with the monoenergetic model. For instance, in SMA connectors various gaps often appear with azimuthal symmetry. In such cases, the single electron model can be used as a first approach to locally study multipaction in the central parts of these gaps [57].

3.3. Theoretical Analysis

Considering the fundamental configuration of parallel plates, a theoretical multipactor analysis can be performed based on the monoenergetic model. As mentioned in Section 2.4.1, two approaches regarding the emission velocity have been mainly applied so far: the constant-k and the constant-u approach. Using the constant-u approach, which is physically more consistent with the fact that the emission and impact velocities are almost uncorrelated, a quasi-analytical study of multipactor is next presented. The analysis is based on the classical multipactor theory which considers two required conditions for multipacting: a) resonant motion of electrons and b) sufficient impact energy which results in SEY higher than unity. The configuration under study is depicted in Fig. 3.1.

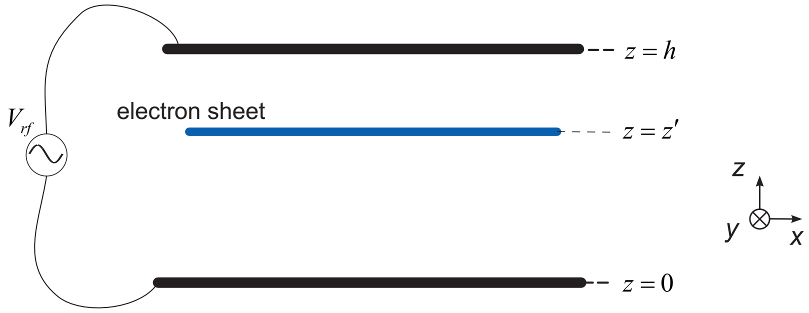

Figure 3.1.: Configuration under study: two infinite parallel plates are considered, lying on xy plane. An external alternating voltage V_{rf} is applied between the plates. The single electron model is assumed: the electrons move in z direction, normally to the plates, all with the same speed, composing an infinite electron sheet.

Assuming a harmonic excitation $V_{\mathrm{rf}} = V \sin(\omega t)$, the electric field between the plates is expressed as follow

$$\mathbf{E} = \frac{V}{h} \sin(\omega t)\, \hat{\mathbf{z}}, \tag{3.1}$$

where h is the distance between the plates and V the peak value of the applied RF voltage. Then, the electrons are accelerated and move between the plates due to the Lorentz force. Let us assume that an electron is emitted from the bottom plate ($z = 0$) at the time $t = t_0$

with an initial velocity u_0, normal to the surface. Then, its motion, in terms of velocity and position, is described by the following formulas

$$u\left(t\right) = -\frac{eV}{mh\omega}\cos\omega t + C_1 \tag{3.2a}$$

and

$$z'\left(t\right) = -\frac{eV}{mh\omega^2}\sin\omega t + C_1 t + C_2, \tag{3.2b}$$

where u and z' are the electron velocity and position, respectively, m the electron mass and e the charge of an electron. The coefficients C_1 and C_2 depend on the initial conditions and are given by the following expressions

$$C_1 = \frac{eV}{mh\omega}\cos a_0 + u_0 \tag{3.3a}$$

and

$$C_2 = \frac{eV}{mh\omega^2}\sin a_0 - \left(\frac{eV}{mh\omega^2}\cos a_0 + \frac{u_0}{\omega}\right) a_0, \tag{3.3b}$$

where $a_0 = \omega t_0$ is the so-called initial phase of the emitted electron.

3.3.1. Resonance condition

In order to investigate the conditions needed for a multipacting process, let us start by studying the resonance of the electron motion. Since parallel plates is a geometrically symmetric structure, the most obvious resonant manner states as follows: the electrons traverse the gap in an odd number of RF cycles. This guarantees that the emitted electrons on the opposite plate are subject to the same initial conditions in reverse and, therefore, a resonant motion is achieved. Such a resonance implies the following condition,

$$z'\left(t_{\text{imp,res}}\right) = h, \tag{3.4a}$$

$$\omega t_{\text{imp,res}} = a_0 + N\pi, \tag{3.4b}$$

where N is an odd number. Substituting Eqs. (3.4) into Eq. (3.2b) the following expression is obtained for the applied peak voltage

$$V_{\text{res}} = \frac{m\omega h}{e\sqrt{\left(N\pi\right)^2 + 4}} \frac{\left(\omega h - N\pi u_0\right)}{\sin\left(a_{0,\text{res}} + \theta\right)}, \tag{3.5}$$

where $\theta = \tan^{-1}\left(N\pi/2\right)$. Taking into account that $\left|\sin\left(a_{0,\text{res}} + \theta\right)\right| \leq 1$, the minimum gap voltage required for a resonant motion is

$$V_{\text{res,min}} = \left|\frac{m\omega h\left(\omega h - N\pi u_0\right)}{e\sqrt{\left(N\pi\right)^2 + 4}}\right|. \tag{3.6}$$

Equation (3.5) can be interpreted as follows: considering a certain frequency-gap product, fh, and an applied gap voltage $V \geq V_{\mathrm{res,min}}$ there are two different ways that an electron can reach the opposite plate after an odd number of half RF cycles. These two ways correspond to two different initial phases, $a_{0,\mathrm{res}}^{(1)}$, $a_{0,\mathrm{res}}^{(2)}$, which can be found by solving Eq. (3.5) in terms of $a_{0,\mathrm{res}}$ as following

$$a_{0,\mathrm{res}}^{(1)} = 2\pi + \sin^{-1}(C_3) - \theta, \tag{3.7a}$$

$$a_{0,\mathrm{res}}^{(2)} = \pi - \sin^{-1}(C_3) - \theta, \tag{3.7b}$$

where $C_3 = \frac{m\omega h(\omega h - N\pi u_0)}{eV_{\mathrm{res}}\sqrt{(N\pi)^2+4}}$. *

Up to now, the condition forced for achieving resonance, as described by Eqs. (3.5) and (3.6), does not consider the presence of the two parallel plates. As Fig. 3.2 illustrates, an electron may hit one of the two surfaces before it theoretically reaches the opposite plate at $t = t_{\mathrm{imp,res}}$. In order to ensure that there is no impact on the walls before the predicted time $t_{\mathrm{imp,res}}$ two additional conditions have to be imposed. The first is related with those cases that the electrons are emitted before the electric field reverses, retarded by the field and finally return to the wall of emission due to low velocity or due to strong retarding electric field, as the example depicted in Fig. 3.2a. The condition required in order to exclude such cases is described by the following set of equations:

$$u(t_{zero}) = 0, \tag{3.8a}$$

$$\dot{u}(t_{zero}) > 0, \tag{3.8b}$$

$$z'(t_{zero}) \geq 0, \tag{3.8c}$$

where $t_{\mathrm{zero}} \in (t_0, t_{\mathrm{imp,res}})$ in terms of t, can be found by imposing the velocity equal to zero in Eq. (3.2a). Similarly, the condition required to ensure that the emitted electrons do not hit the opposite plate prior to the expected impact time $t_{\mathrm{imp,res}}$ can be expressed as follow:

$$u(t_{zero}) = 0, \tag{3.9a}$$

$$\dot{u}(t_{zero}) < 0, \tag{3.9b}$$

$$z'(t_{zero}) \leq d. \tag{3.9c}$$

Let us call the two conditions, described by Eqs. (3.8) and (3.9), as the ‘non-returning’ and the ‘non-advanced impact’ conditions, respectively.

In order to ensure resonance, the non-returning and the non-advanced impact conditions should be both satisfied for, at least, one of the initial resonant phases $a_{0,\mathrm{res}}^{(1)}$ and $a_{0,\mathrm{res}}^{(2)}$. The systems of Eqs. (3.8) and (3.9) can not be analytically solved and a numerical treatment is needed. It can be shown that the maximum voltage for which a resonance can occur, $V_{\mathrm{res,max}}$, is determined by the non-returning limit which is the solution of equation system (3.8) by

---

[*] Considering $\omega h > N\pi u_0$, which states for the most practical cases, both $a_{0,\mathrm{res}}^{(1)}$ and $a_{0,\mathrm{res}}^{(2)}$, as expressed in Eq. (3.7), belong to $[0, 2\pi]$ since $C_3 < 0$ and, consequently, $\sin^{-1}(C_3) \in [-\pi/2, 0)$. If $\omega h < N\pi u_0$, then, the phase $a_{0,\mathrm{res}}^{(1)}$ can be expressed as $a_{0,res}^{(1)} = \sin^{-1}(C_3) - \theta$ so that both $a_{0,\mathrm{res}}^{(1)}$ and $a_{0,\mathrm{res}}^{(2)} \in [0, 2\pi]$

forcing equality in Eq. (3.8c). For gap voltages higher than $V_{\text{res,max}}$, the retarding field is strong enough as to force the electrons to return to the wall of emission after a short lapse of time.

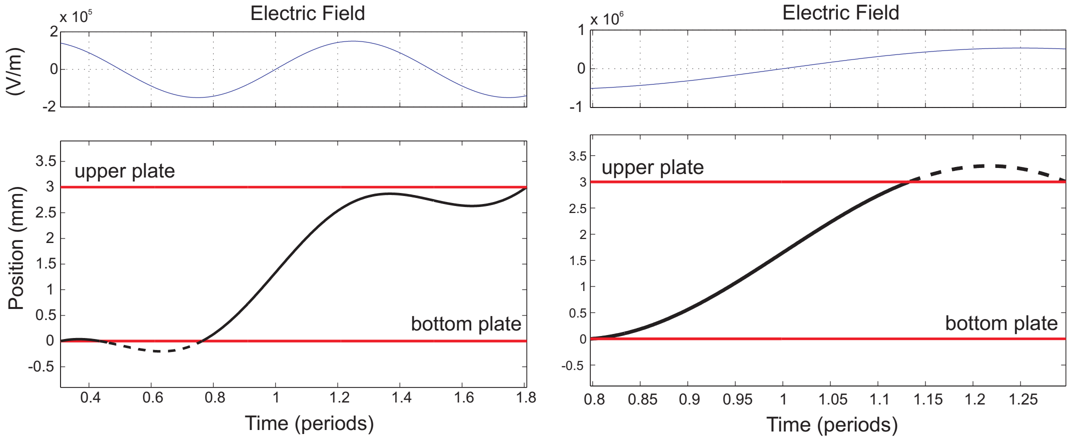

(a) (b)

Figure 3.2.: Theoretical resonant motion without considering the presence of the plates. a) The electron returns back to the initial plate before it reaches the opposite one. b) Advanced impact on the opposite plate before the predicted impact at $t_{\text{imp,res}}$.

3.3.2. Secondary Emission condition

In addition to resonance, multipacting also implies that the electrons hit the walls with sufficient energy in order to result in SEY values higher than unity. This requires that the impact velocity of the resonant electrons, u_{imp}, has to be between the first and the second crossover points of the SEY curve, namely u_1 and u_2. Let us call this condition as the 'secondary emission condition', expressed by the following equation

$$u_1 \leq u_{\text{imp}} \leq u_2. \tag{3.10}$$

In order to draw the multipactor susceptibility zones, we have to transform the above condition for impact velocity into a condition for the applied gap voltage. Substituting Eq. (3.4b) in Eq. (3.2a), yields

$$u_{\text{imp}} = \frac{2eV_{\text{res}}}{m\omega h} \cos a_{0,\text{res}} + u_0. \tag{3.11}$$

Then, by solving Eq. (3.11) in terms of the initial resonance phase, $a_{0,\text{res}}$, and substituting it in Eq. (3.5) one can find the voltage required so that a resonant electron hits the opposite wall with u_{imp} [58],

$$V_{\text{res},u_{\text{imp}}} = -\frac{m\omega h}{2e}\sqrt{\frac{(N\pi)^2+4}{4}\Delta_u^2 - N\pi\left(\omega h - N\pi u_0\right)\Delta_u + \left(\omega h - N\pi u_0\right)^2} \tag{3.12}$$

where $\Delta_{\mathrm{u}} = u_{\mathrm{imp}} - u_0$. An interpretation of Eq. (3.12) is given in Fig. 3.3. As expected, the $V_{\mathrm{res},u_{\mathrm{imp}}}$ is always above the minimum limit $V_{\mathrm{res,min}}$ since Eq. (3.12) incorporates resonance. However, for each curve, corresponding to different impact velocities, there is a crucial point where $V_{\mathrm{res},u_{\mathrm{imp}}}$ becomes equal to $V_{\mathrm{res,min}}$, as depicted in Fig. 3.3 with the points A and B. Using Eqs. (3.12) and (3.6) it can be shown that $V_{\mathrm{res},u_{\mathrm{imp}}}$ and $V_{\mathrm{res,min}}$ coincide for

$$(fh)_{\mathrm{c}} = \frac{\left(N^2\pi^2 + 4\right)\left(u_{\mathrm{imp}} - u_0\right)}{4N\pi^2} + \frac{Nu_0}{2}. \tag{3.13}$$

From Eq. (3.13), it can be obviously derived that as the impact velocity increases the corresponding $(fh)_{\mathrm{c}}$ increases, too. If $(fh)_{c,1} \leq fh \leq (fh)_{c,2}$, where $(fh)_{c,1}$ and $(fh)_{c,2}$ correspond to u_1 and u_2, respectively, there is always a point on the minimum resonant limit curve that corresponds to impact velocity, u_{imp}, such that $u_1 \leq u_{imp} \leq u_2$. Therefore, between $(fh)_{c,1}$ and $(fh)_{c,2}$ the lower multipactor threshold is determined by the minimum resonant limit, $V_{\mathrm{res,min}}$. For $fh < (fh)_{c,1}$ the secondary emission condition in no more satisfied on the minimum resonant limit and it is the V_{res,u_1} that determines the multipactor threshold, where V_{res,u_1} is given by Eq. (3.12) for $u_{\mathrm{imp}} = u_1$. On the other hand, for the upper multipactor threshold the voltage limit V_{res,u_2} that corresponds to the second crossover SEY point has to be take in into account. At the end the secondary emission condition, as described by Eq. (3.10) can be expressed in terms of gap voltage V as follows:

$$V \geq V_{\mathrm{res},u_1}, \quad \forall\, fh \leq (fh)_{\mathrm{c},1}, \tag{3.14a}$$

$$V \leq V_{\mathrm{res},u_2}, \quad \forall\, fh \leq (fh)_{\mathrm{c},2}. \tag{3.14b}$$

3.3.3. Stability Condition

Up to now, only the conditions for resonance and secondary emission have been considered in the above analysis. However, as discussed in Section 2.4.2, it is possible that an initial phase results in an unstable resonant motion. This means that if the secondary electrons are emitted with a small phase error with regard to the resonance phase, e.g. due to random emission velocity, they do not converge to the expected resonant motion. As a result, the electrons will follow a random-like motion and they will, most likely, be lost due to impacts with low velocities. In order to study whether a resonance phase is stable or not a stability factor, G, is introduced

$$G = \frac{{a'}_0 - a_{0,\mathrm{res}}}{a_0 - a_{0,\mathrm{res}}}, \tag{3.15}$$

where a_0 is the emission phase, ${a'}_0$ the emission phase after the impact on the opposite plate and $a_{0,\mathrm{res}}$ the examined resonant phase as defined in Eq. (3.4). As Eq. (3.15) describes, the stability factor represents the ratio between the initial and the final phase error. Then, the condition required for a stable resonant motion is posed as

$$|G| < 1, \tag{3.16}$$

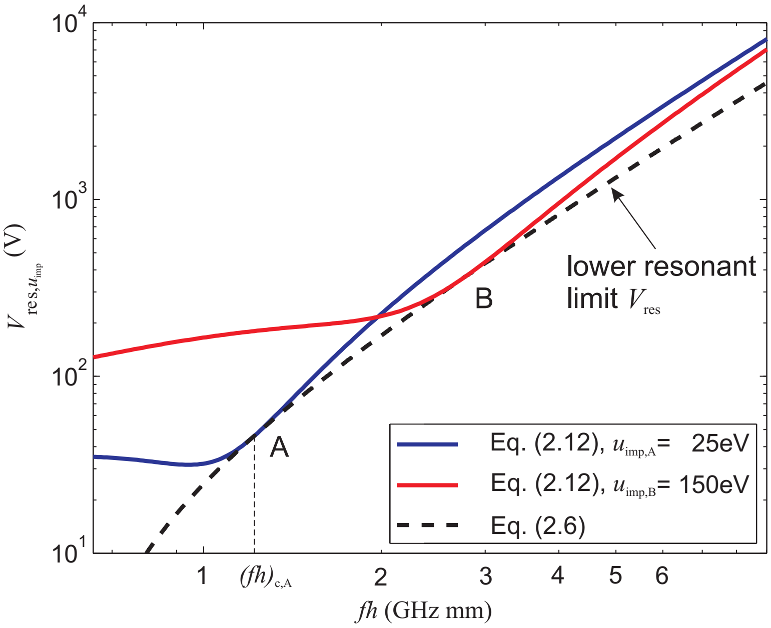

Figure 3.3.: Solid lines: Gap voltage required so that the resonant electrons hit the opposite plate with a certain impact energy. The dashed line corresponds to the minimum possible gap voltage needed for resonant motion, i.e. $V_{\mathrm{res,min}}$ as given in Eq. (3.6). The 1^{st} resonance mode is considered. The emission velocity is $u_0 = 4\mathrm{eV}$

which ensures that the phase error decreases after every impact and, consequently, the launch phase converges to the resonant phase. Following the stability analysis presented in [59] one can derive the range of initial phases that satisfy the stability condition as

$$\varphi_l \le a_{0,\mathrm{res}} \le \varphi_u \tag{3.17}$$

where

$$\varphi_l = \frac{\pi}{2} + \tan^{-1}\left[\frac{N\pi}{2}\left(\frac{u_{\mathrm{imp}} - u_0}{u_{\mathrm{imp}} + u_0}\right)\right] \tag{3.18a}$$

and

$$\varphi_u = \frac{3\pi}{2} - \tan^{-1}\left(\frac{N\pi}{2}\right). \tag{3.18b}$$

Next, let us study the stability condition assuming that

$$\omega h > N\pi u_0 \tag{3.19}$$

which holds for the most of the cases of practical interest since multipactor typically occurs for frequency-gap products higher than $N\pi u_0$, as will be shown later. A graphical representation of the stability condition is given in Fig. 3.4.

Considering Eq. (3.19), the upper limit φ_u coincides with the initial phase required for resonant motion with the minimum possible voltage $V_{\mathrm{res,min}}$. Indeed, according to Eqs. (3.6) and (3.7), when $V_{\text{res}} = V_{\text{res,min}}$ both initial resonance phases $a^{(1)}_{0,\text{res}}$ and $a^{(2)}_{0,\text{res}}$ are equal to $\frac{3\pi}{2} - \theta = \frac{3\pi}{2} - \tan^{-1}\left(\frac{N\pi}{2}\right) = \varphi_u$. Applying a, slightly, higher gap voltage, $V > V_{\text{res,min}}$, the two resonance phases start diverging from the phase φ_u. In particular, $a^{(2)}_{0,\text{res}}$ moves towards lower angles, thus, remaining in the valid stability range, while $a^{(1)}_{0,\text{res}}$ exceeds the upper limit φ_u resulting in non-stable resonant motion. As can be seen in Fig. 3.4, the resonant phase $a^{(1)}_{0,\text{res}}$ moves completely out of the valid stability area, resulting in non-stable resonant motions. Therefore, in the remainder we focus only on the resonance phase $a^{(2)}_{0,\text{res}}$.

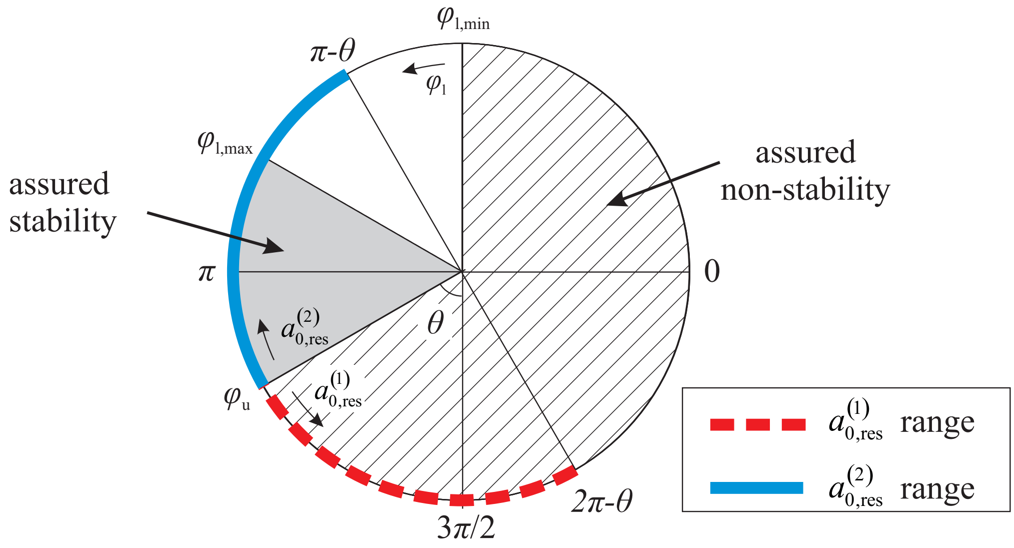

Figure 3.4.: Range of stable resonance phases according to Eq. (3.16). Stability is assured in the grey area, i.e. in the range $[\varphi_{\text{l,max}}, \varphi_u]$. Stability is possible under conditions in the white area i.e. in the range $[\varphi_{\text{l,min}}, \varphi_{\text{l,max}}]$, while stability is impossibe in the remaining, shadowed area. The phase range of the resonance phases $a^{(1)}_{0,\text{res}}$ and $a^{(2)}_{0,\text{res}}$ are also depicted, under the assumption $\omega h > N\pi u_0$. The arrows show the trend of $a^{(1)}_{0,\text{res}}$, $a^{(2)}_{0,\text{res}}$ and φ_{l} as the applied gap voltage increases.

As the applied voltage increases, the impact velocity increases, too. As a consequence, the φ_{l} moves towards higher angles approaching the limit $\varphi_{\text{l,max}}$ which is the maximum value that the lower limit φ_{l} can get. On the other hand, the resonance phase $a^{(2)}_{0,\text{res}}$ moves towards the opposite direction converging to $\pi - \theta$ which is the limit value it can theoretically get for $V_{\text{res}} \to \infty$ (see Eq. (3.7b)). It is obvious that there exists a voltage level, $V_{\text{st,max}}$, for which $a^{(2)}_{0,\text{res}}$ and φ_{l} meet in the phase interval $(\pi - \theta, \varphi_{\text{l,max}})$. Then, $V_{\text{st,max}}$ defines the voltage limit for stability and can be found by solving the following equation

$$a^{(2)}_{0,\text{res}}\left(V_{\text{res}}\right) = \varphi_l\left(V_{\text{res}}\right) \tag{3.20}$$

in terms of V_{res}, where $a^{(2)}_{0,\text{res}}\left(V_{\text{res}}\right)$ and $\varphi_l\left(V_{\text{res}}\right)$ are given by Eqs. (3.7b) and (3.18a), respectively.

3.3.4. Multipactor Chart

So far, we have defined the appropriate conditions required for multipacting. By imposing them, we can plot the multipactor chart which depicts the operation zones susceptible to multipactor effect, in terms of the applied voltage and frequency-gap product. First, let us discuss the conditions that determine the lower and the upper multipactor threshold of susceptibility zones through an example considering the 1^{st} resonance mode, as illustrated in Fig. 3.5.

As Fig. 3.5a depicts, the lower threshold is formed by the following two limits: first, the minimum resonance limit that is the minimum voltage required for resonant motion, and, second, the lower secondary emission limit which ensures impact velocities higher than the first SEY crossover point. Two distinguished areas, below and above $(fh)_{\mathrm{c},1}$, are observed, where the threshold follows different trends. Starting with low values of frequency-gap product, it can be seen that the minimum resonant limit is notably low, meaning that the electrons are able to achieve resonant motion with low electric field amplitude. However, they do not acquire sufficient energy in order to provoke the emission of new electrons until the voltage overcomes the secondary emission limit. Therefore, for small frequency-gap products the threshold is determined by the secondary emission condition. As fh increases, the two limits approach each other and, finally, they meet at a point corresponding to $fh = (fh)_{\mathrm{c},1}$. Above this point, it can be proved† that the contour of $u_{\mathrm{imp}} = u_1$ (dashed line with crosses) corresponds to unstable resonant phases. On the other hand, as described in Section 3.3.2, for $fh \geq (fh)_{\mathrm{c},1}$ the minimum resonance limit corresponds to resonant motions with impact velocities higher than the first SEY crossover point, satisfying, thus, the required multipacting conditions. Therefore, it is the minimum resonance limit that determines the multipactor threshold for frequency-gap products higher than $(fh)_{\mathrm{c},1}$.

Regarding the upper multipactor threshold, it is determined by three conditions, namely stability, non-returning and secondary emission, as illustrated in Fig 3.5b. For low frequency-gap products, it is the stability condition that is more restrictive. As fh increases, there is a point where the stability limit crosses the non-returning one. Above it, the threshold is determined by the non-returning limit as long as the upper secondary emission limit is satisfied. Then, the electric field is strong enough to provoke impact velocities higher than the second SEY crossover point, resulting in absorption of electrons. Therefore, multipaction is restricted for high voltages by the secondary emission condition. Similarly to the case of lower threshold, there is a crucial point, corresponding to $fh = (fh)_{\mathrm{c},2}$, where the secondary emission limit touches the minimum resonance limit. Above this point there can not exist stable resonant motions with impact velocity lower u_2. Therefore, the upper multipactor threshold is limited to $fh \leq (fh)_{\mathrm{c},2}$.

The area enclosed between the lower and the upper multipactor threshold, i.e. between the grey and the black solid lines in Fig. 3.5b, defines the susceptibility zone of the corresponding

---

[†] Equation (3.12) can be reformulated as $2eV_{\mathrm{res,imp}}/m\omega h = -y$ where y is equal to the square root of the right hand side. Then, substituting $2eV_{\mathrm{res,imp}}/m\omega h$, Eq. (3.10) can be rewritten as $\cos a_{0,\mathrm{res}} = -(u_{\mathrm{imp}} - u_0)/y$. As fh is getting higher, y increases too (see Eq. (3.12) for constant Δ_u). For $fh = (fh)_{\mathrm{c},1}$, $\alpha_{0,res} = 3\pi/2-\theta$, as discussed in Section 3.3.3. Therefore, for $fh \geq (fh)_{\mathrm{c},1}$, y increases, $a_{0,\mathrm{res}}$ decreases and, consequently, it enters to the non-stability area, as illustrated in Fig. 3.4.

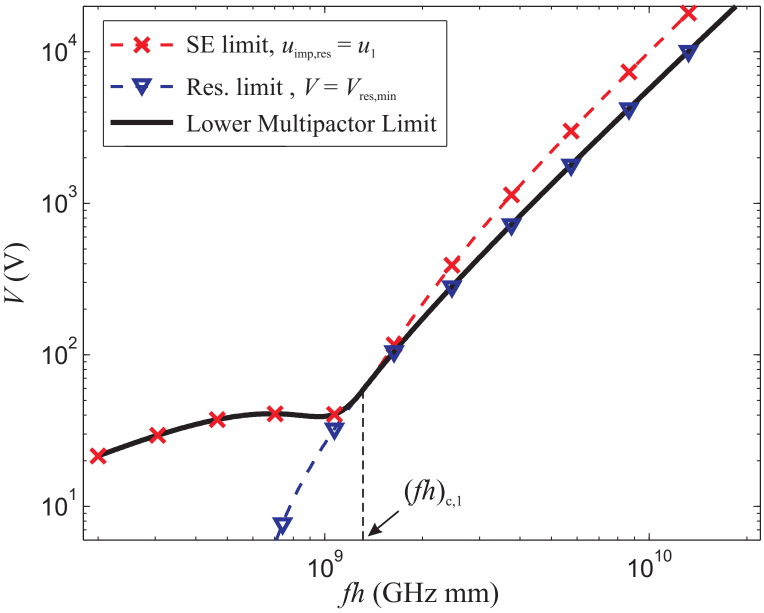

(a) Conditions that determine the lower multipactor threshold. The value $(fh)_{c,1}$ corresponds to the crucial frequency-gap product, as given in Eq. (3.13), for impact velocity equal to the first SEY crossover point, u_1.

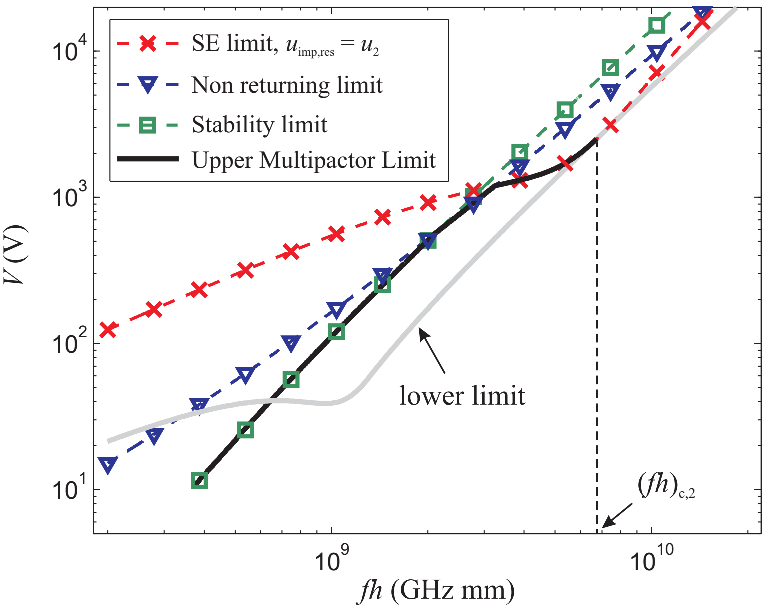

(b) Conditions that determine the upper multipactor threshold. The value $(fh)_{c,2}$ corresponds to the crucial frequency-gap product, as given in Eq. (3.13), for impact velocity equal to the second SEY crossover point, u_2. For comparison purposes the lower multipactor threshold of Fig. 3.5a has been added (grey line).

Figure 3.5.: a) Lower and b) upper multipactor threshold for the 1st multipactor mode. The parameters are: $u_0 = 3.68\text{eV}$, $u_1 = 30\text{eV}$ and $u_2 = 1000\text{eV}$.

resonance mode. Table 3.1 summarizes the conditions that have been imposed in order to obtain the multipactor thresholds. Similarly, we can enforce the same conditions in order to derive the susceptibility zones for higher resonance modes, too.

Figure 3.6 depicts the multipactor chart for the same parameters as in Fig. 3.5, taking into account the first four resonance modes. As can been seen, by increasing the order of the mode the stability condition becomes more restrictive resulting in very narrow susceptibility zones. This trend can be qualitatively explained through the diagram of Fig. 3.4 as following: As the order N increases, the angle θ increases, too, since $\theta = \tan^{-1}(N\pi/2)$ and consequently, the grey area in Fig. 3.4 that approximately defines the phase range of stability is getting significantly narrower.

In Section 3.3.1 we saw that for a certain mode there are two ways, for achieving a resonant motion, corresponding to two different initial phases. Here, through the multipactor chart, we notice that different resonance modes may overlap, e.g. modes corresponding to $N = 3$ and $N = 5$. This means that there may exist even more than two ways, corresponding to different resonance modes, that an electron achieves resonant motion. However, by imposing the stability condition, the zones are clearly separated, meaning that for certain operational parameters $(V,\, fh)$ there exists a unique manner to achieve a stable resonant motion.

3.4. Generalized Single Electron Model

The theoretical analysis described in the previous Section can provide a first, qualitative insight into the multipacting process. However, it is limited to parallel plates structures as well as to certain multipacting manners, like the fundamental, odd-order, resonance modes. Here, we present a generalized single electron model able to extent the multipactor analysis to any 1D configuration. The model is based on a numerical tracker able to analyze the electron dynamics under arbitrary unidirectional electric fields. Different secondary emission properties can be considered for the walls of the structure under study, allowing the analysis of any metal-metal, metal-dielectric or dielectric-dielectric configuration. Furthermore, by

Condition	Expression	Equation
Resonance, lower limit	$V \geq V_{\text{res,min}}$	Eq. (3.6)
Non-returning limit	$V \leq V_{\text{res,max}}$	Eq. (3.8)
Secondary emission, lower limit	$V \geq V_{\text{res},u_1}, \quad \forall fh \leq (fh)_{\text{c},1}$	Eq.(3.14a), Eq. (3.12), Eq. (3.13)
Secondary emission, upper limit	$V \leq V_{\text{res},u_2}, \quad \forall fh \leq (fh)_{\text{c},2}$	Eq.(3.14b), Eq. (3.12), Eq. (3.13)
Stability limit	$V \leq V_{st,max}$	Eq. (3.20)

Table 3.1.: Multipacting Conditions.

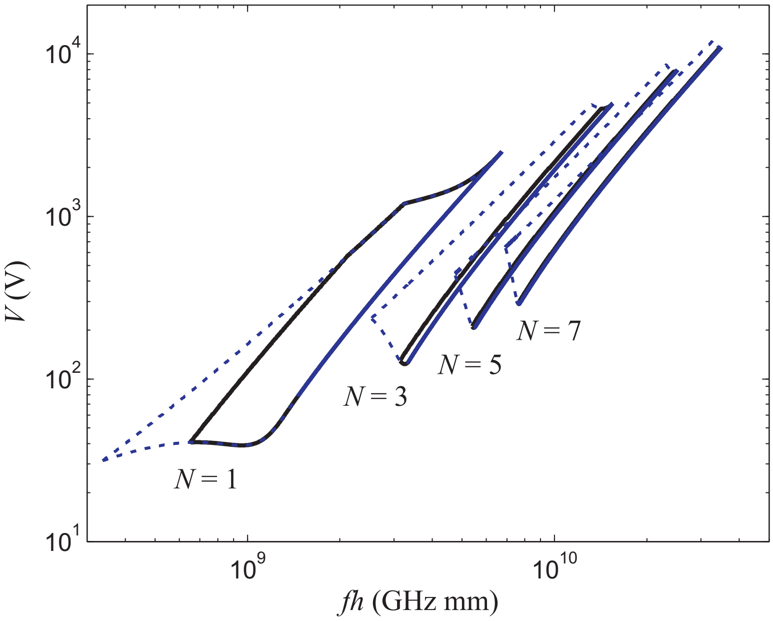

Figure 3.6.: Multipactor chart using the same parameters as in Figs. 3.5a and 3.5b. The first four, odd-order, resonance modes are considered. The zones delimited by solid lines indicate the areas within which phase-focusing is active (stable resonance). The dashed lines represent zones without considering the stability condition (unstable phases are also included).

applying realistic SEY models, the effect of the elastically reflected electrons, for low impact energies, can be taken into account as well. In the following numerical analysis, z coordinate is considered to be the direction of the unidirectional field.

3.4.1. Algorithm

The analysis starts by placing an effective electron in an arbitrary position, z_0, between the walls of the examined configuration, with a random initial velocity v_0. The effective electron represents the total electron population according to the single electron model. Let us assume that the initial number of electrons is $N_{\mathrm{e},0}$. Then, taking into account the Lorentz force, the electron position is tracked by solving the equation of motion,

$$\frac{d^2 z}{dt^2} = \frac{e}{m} E\left(z,t\right), \tag{3.21}$$

where $E\left(z,t\right)$ is the electric field along the examined 1D direction. In order to consider arbitrary field distributions, Eq. (3.21) is numerically solved by using a 4^{th} order Runge-Kutta differential scheme. More details about the numerical solver are given in the next Chapter for the more general, 3D case. When the tracker identifies a collision to any of the surfaces, a secondary emission model (SEM) is applied in order to update the state of the effective electron, that is the velocity and the electron population. Since the analysis is based on the monoenergetic approach, after an impact the effective electron is emitted with a fixed velocity, u_0, which can be different for the two considered surfaces. On the other hand, a secondary emission yield (SEY) model is used in order to estimate the electron population after impacts as follows:

$$N_{\mathrm{e}}^{i} = \delta\left(u_{\mathrm{imp}}^{i}\right) N_{\mathrm{e}}^{i-1}, \tag{3.22}$$

where u_{imp}^{i} is the impact velocity at the i^{th} impact, $\delta\left(u_{\mathrm{imp}}^{i}\right)$ the corresponding SEY value, N_{e}^{i} and N_{e}^{i-1} the number of electrons before and after the impact, respectively.

The above procedure continues until a preselected time period, t_{f}, is reached. Depending on the trend of the electron population it can be estimated if multipactor discharge is likely to occur or not. As a figure of merit, we introduce an exponential coefficient a assuming that the number of electrons is expressed as follows:

$$N_{\mathrm{e}}\left(t\right) = 10^{at}. \tag{3.23}$$

Then, if $N_{\mathrm{e,f}}$ is the number of electrons at time $t = t_{\mathrm{f}}$ the coefficient a yields

$$a = \frac{\log_{10} N_{\mathrm{e,f}} - \log_{10} N_{\mathrm{e},0}}{t_{\mathrm{f}} - t_0}. \tag{3.24}$$

By Eq. 3.23, it can be seen that the coefficient a expresses the rate of growth or decrease in case the discharge takes place or not, respectively. A multipactor criterion can be set as $a > 0$ since an increase of the electron population is, then, predicted.

	u_1 (eV)	$u_{\max}$ (eV)	$\delta_{\max}$	u_2 (eV)	$\varepsilon_{0,\text{elast}}$
Silver [2, 3]	30	165	2.22	1395	0.5
Copper [2, 3]	25	175	2.25	2940	0.5
Alodine [2, 3]	41	180	1.83	1455	0.5
Gold [3, 60]	25	288	2.56	5000	0.5

Table 3.2.: SEY properties for different materials applying SEY model of [3]

Simulation Parameters

In the following simulations the SEY model of Lara et. al [3] has been used. This model has been preferred among others since it takes into account both reflected and secondary emitted electrons as shown in Fig. 3.7. Table 3.2 summarizes the SEY properties of the materials used in the following examples. After impact events, the effective electron is emitted with an initial velocity $u_0 = 3.68$ eV. High accuracy of the electron motion is ensured by a sufficiently small time step in the Runge-Kutta integrator, equal to $T/1000$ where T is the period of the applied RF field. A preselected time period $t_\text{f} = 200\ T$ is considered for finishing the algorithm process. By performing several simulations with higher t_f it has been shown that 200 periods are sufficient to obtain a clear view regarding the multipactor evolution.

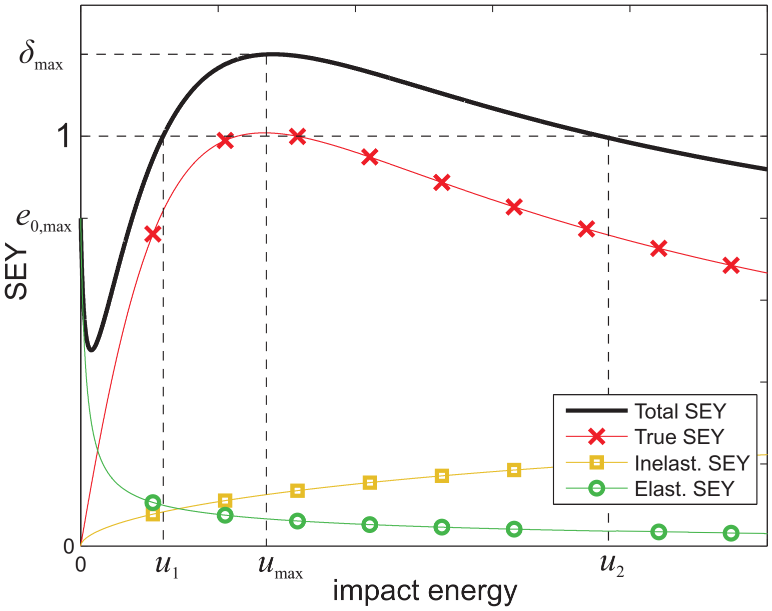

Figure 3.7.: Qualitative representation of the applied SEY model [3]. The SEY function (solid black line) considers additively all the secondary emission mechanisms.

3.4.2. Multipactor Chart Representation

Before continuing with numerical results, let us, first, discuss how the multipactor chart can be represented. Figure 3.8 depicts four different representations of the multipactor chart as obtained by the proposed technique.

The most straightforward way of representation is to depict the multipactor threshold, similarly to the chart of Fig. 3.6. In the case of the applied numerical model the multipactor threshold can be identified by the following condition

$$\log_{10}\left(\frac{N_{\mathrm{e},f}}{N_{\mathrm{e},0}}\right) \geq 0, \tag{3.25}$$

which implies an increase of the electron population. However, in this way all the information regarding the growth rate of electron population is omitted.

Looking for a way to illustrate high and low risk areas, i.e. zones where multipaction is more or less likely to occur, we could exploit the estimated number of electrons, N_{e}, as given in Eq. (3.22). Since saturation is not taken into account, the population, N_{e}, grows continuously and exponentially yielding huge, unrealistic, values. Instead, we could introduce a coefficient a_{T} expressing the multipacting rate per period as follows

$$N_{\mathrm{e}}(n) = 10^{a_{\mathrm{T}} n}, \tag{3.26}$$

where $N_{\mathrm{e}}(n)$ is the electron population after n periods. Then, one could expect that the discharge is more likely to occur in areas with higher a_{T}, i.e. areas with intense color in Fig. 3.8b. However, this representation underestimates the zones that correspond to high order multipactor modes. As the resonance order increases the coefficient a_{T} decreases due to the fact that less impact events occur per RF period, meaning that the phenomenon evolves after more periods. This trend, however, is not directly related with the likelihood of the breakdown to take place which is more connected with the impact energy of the collided electrons on the boundaries.

In order to consider more fairly the high order multipactor modes we can, alternatively, study how intense the secondary emission is after impact events. To this purpose, we introduce an effective secondary emission yield, δ_{eff}, given by the geometric mean value of the SEY at impact events

$$\delta_{\mathrm{eff}} = \left(\delta_1 \delta_2 \cdots \delta_{N_{\mathrm{imp}}}\right)^{\frac{1}{N_{\mathrm{imp}}}}, \tag{3.27}$$

where δ_{i} corresponds to the i^{th} impact and N_{imp} is the corresponding number of impacts. By its definition, the effective coefficient δ_{eff} expresses in a mean way the intensity of the secondary emission mechanism after impacts, providing, thus, a representative figure of likelihood the discharge to occur.

Finally, Fig. 3.8d illustrates a way to represent how fast the phenomenon is estimated to evolve by using the rate coefficient a defined in Eq. (3.24). Comparing to the coefficient a_{T} represented in the chart of Fig. 3.8b, a provides a figure of growth in absolute time and not normalized to the RF period time as in the case of a_{T}. This measure can be fruitfully used in saturation studies as a first estimation of the time the phenomenon takes to reach the steady

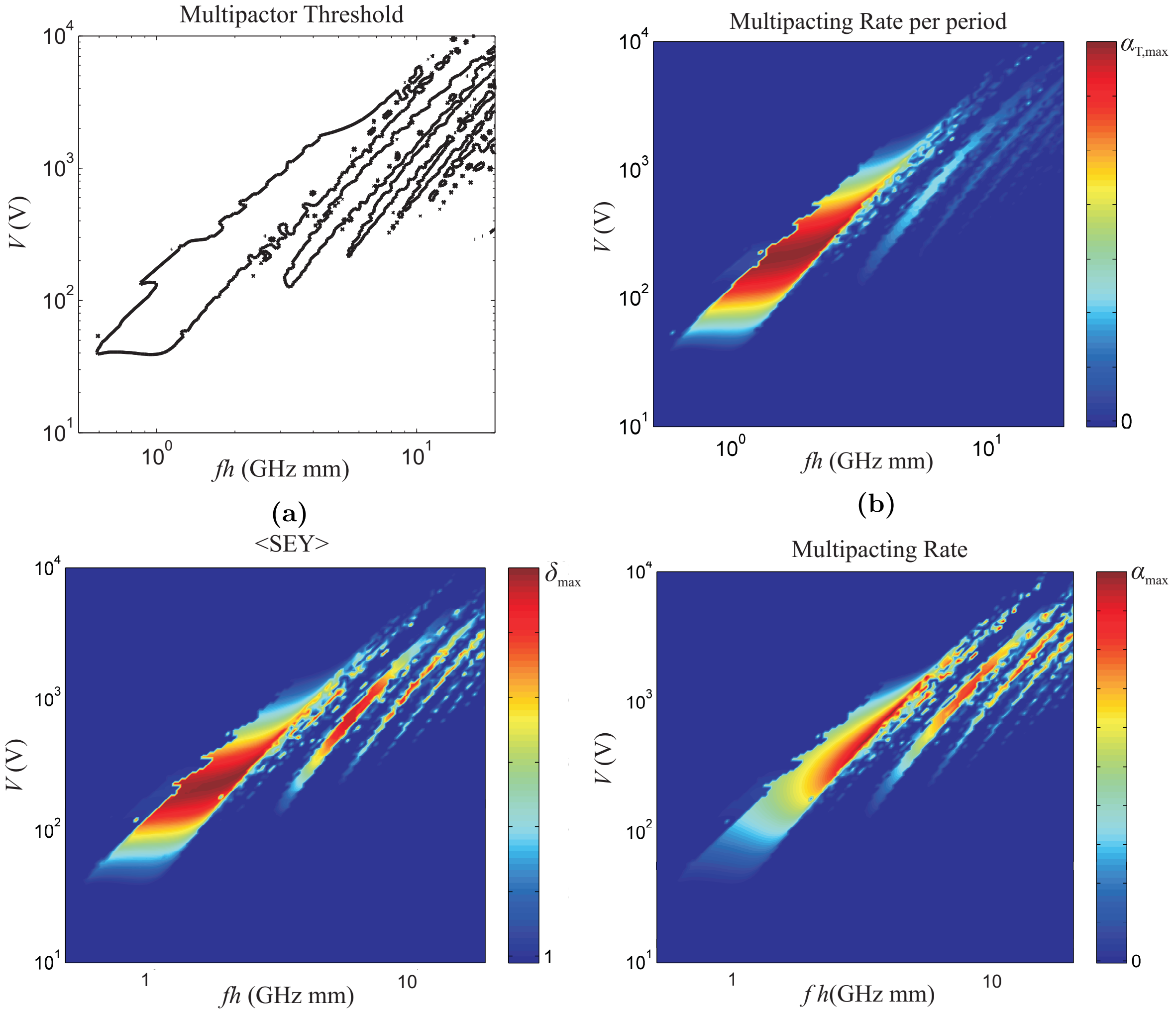

(a) (b) (c) (d)

Figure 3.8.: Different representations of multipactor chart. a) Multipactor threshold. b) Multipacting rate per period expressed by exponential coefficient a_{T} as given in Eq. (3.26). c) Geometric mean value of SEY at impacts. d) Multipacting rate expressed by exponential coefficient a as given in Eq. (3.23). The color scale is linear in all cases. Results have been obtained by considering SEY properties of silver. For the studied case the maximum values in the charts b), c) and d) are $a_{\mathrm{T,max}} = 0.8$, $\delta_{\max} = 2.22$ and $a_{\max} = 2\ \mathrm{ps}^{-1}$, respectively.

state.

3.4.3. Validation

First, the validity of the proposed numerical method has been tested through comparisons with the theoretical analysis as presented in Section 3.3. Figure 3.9 illustrates representative results regarding the multipactor threshold in parallel plates structures. As can be seen, all the fundamental multipactor modes, as set in theoretical analysis, are clearly identified by the proposed numerical approach. Nice agreement is noticed for the lower multipactor threshold, especially for low gap voltages. As the gap voltage increases, the numerical analysis predicts broader susceptibility zones compared to the ones obtained by theory. This is due to the generalized nature of the numerical approach that incorporates any manner which can lead to multipacting in addition to the fundamental multipactor modes.

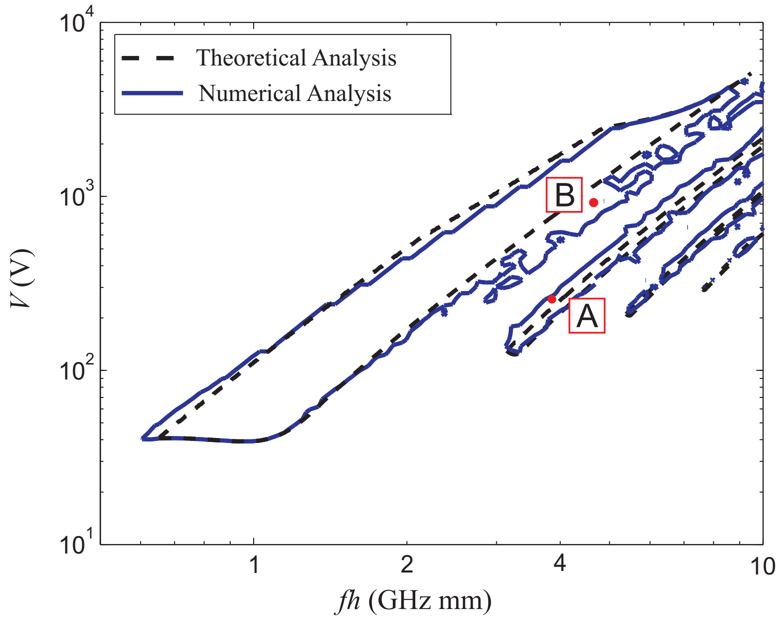

Figure 3.9.: Multipactor zones in parallel plates considering SEY parameters of silver.

Figure 3.10 depicts two representative cases where multipacting occurs in regions out of the classical multipactor zones as defined by the theoretical analysis. As observed, there exist hybrid resonance modes, as the one in Fig. 3.10b where periodicity is achieved after several subsequent impacts. Furthermore, multipacting can occur even if perfect periodicity is not achieved, as in Fig. 3.10a. In the depicted case, the electrons follow a 3^{rd} order resonant-like motion resulting in an electron population growth similarly to the classical 3^{rd} multipactor mode.

In order to further validate the proposed technique, we have compared it with experimental and numerical results in two examples studying multipaction in coaxial lines. First, we have considered a coaxial cable, made of copper electrodes, with a characteristic impedance equal to $Z = 50\ \Omega$. Figure 3.11a depicts the corresponding multipactor chart, as obtained

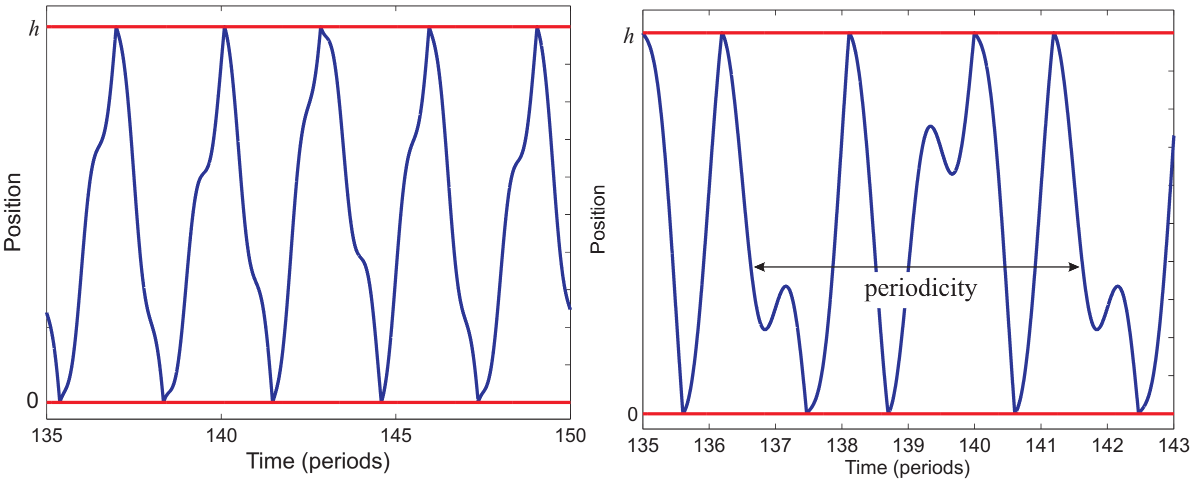

(a) **(b)**

Figure 3.10.: Electron motion corresponding to points A and B of Fig. 3.9. a) point A: $fh = 3.73$ GHz mm, $V = 240$ V, b) point B: $fh = 4.86$ GHz mm, $V = 1030$ V

by applying our numerical analysis, and the multipactor threshold as identified through measurements of Woo [61]. Fairly good agreement between numerical and experimental results is shown regarding the susceptibility zones. The slopes of both upper and lower thresholds are accurately identified by the numerical approach. In particular, the reduced slope of the lower multipactor threshold, as obtained by the measurements, is justified by the existence of high order multipactor modes, as predicted by the numerical model. The discrepancies observed in the left area of the multipactor chart, i.e. between the rounded threshold of measurements and the sharp shape of multipactor zone of numerical analysis, comes from the poor statistical representation of the single electron model. In general, the single electron model seems to overestimate multipaction especially close to the lower threshold. However, as can be seen, the parts of susceptibility areas placed beyond the measured threshold correspond to low risk zones as expressed by the geometric mean value of SEY.

Next, we have compared our technique with the work of Arter and Hook that was based on a particle-in-cell (PIC) code for predicting multipactor threshold in coaxial lines [62]. Comparative results for a coaxial line made of alodine material are given in Fig 3.11b. A very good agreement between the shape of the susceptibility zones and the threshold predicted by Arter and Hook is observed for a wide range of frequency-gap product. In particular, it can be seen that all the points corresponding to the multipactor threshold of [62] are placed on the edge of the multipactor zones, thus, confirming the validity of our approach.

3.5. Examples of Analysis

In this section, we apply the proposed method in order to study multipaction, both qualitatively and quantitatively, in two different examples including parallel plates and coaxial line configurations. First, we discuss the effect of the elastically reflected electrons in the evolution

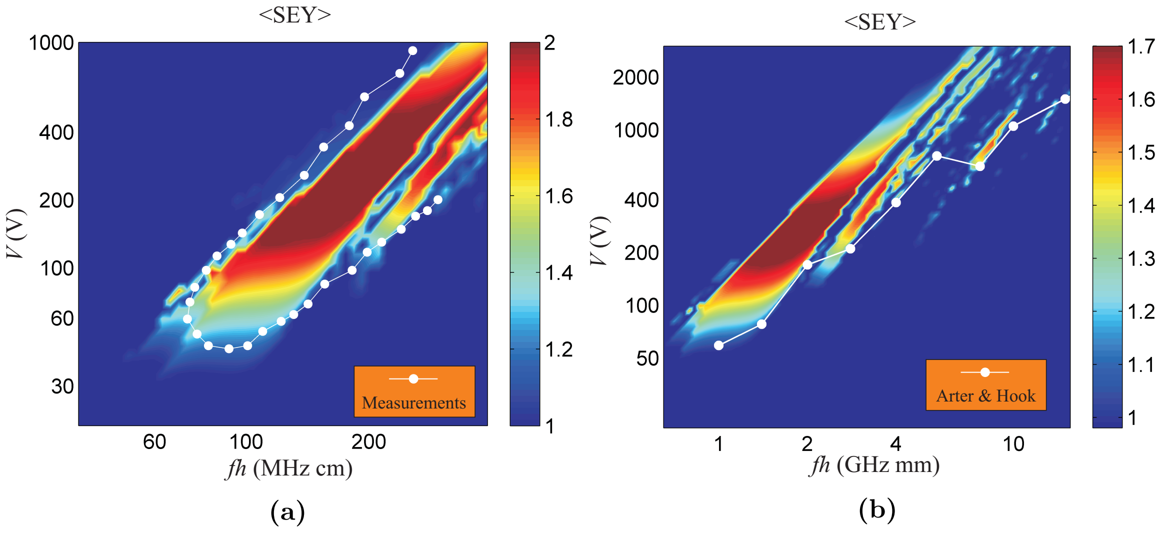

Figure 3.11.: Multipactor chart for coaxial lines compared with a) Woo experiments [61] for a coaxial line of copper and b) numerical results for a coaxial line of alodine [62]. In both cases the characteristic impedance is equal to $Z = 50\ \Omega$.

of the phenomenon. In particular, through parametric analysis we qualitatively study how the multipactor threshold is affected by considering different amount of elastically reflected electrons. As a second example, we study multipaction in coaxial lines focusing in two aspects with particular interest: first, the applicability of parallel plates approximation in coaxial lines and second, how the non-uniform fields in coaxial lines result in single-sided multipaction.

3.5.1. Effect of elastic reflection in multipactor evolution

Elastic reflection is one of the emission mechanisms that may follow electron collisions on a surface, especially at low impact energies. As already discussed in Chapter 2.1, for low impact velocities emission of true secondaries is significantly weak and, consequently, the total SEY curve is governed by the elastic reflection yield. In particular, the value of SEY in the limit of zero impact energy, $\varepsilon_{0,\mathrm{elast}}$, is defined by the ratio between the reflected and impinging electrons and can vary from zero to one, depending on how intense the elastic reflection mechanism is. Although SEY has been extensively studied, the evolution of the SEY as the impact electron energy decreases to zero remains still unclear. This is, essentially, due to the fact that SEY measurements for low impact energies constitute a particularly difficult process [63, 64]. Published results in the literature are sometimes contradictory. Some works have concluded that $\varepsilon_{0,\mathrm{elast}}$ is close to one [3, 50], thus, implying intense elastic reflection, whereas other works claim that SEY tends to zero for low impact energies [65, 66].

This ambiguity, related to the emission yield at low impact energies, has triggered particular interest in studying the effect of elastically reflected electrons in the mutlipacting process. Cimino *et al* [50] reported that low-energy electrons can notably affect multipacting in particle accelerators resulting in a significant increase of the surface heat load. The effect of elastic reflection mechanism has been also studied in parallel plates configurations [67, 68]. In particular, an extensive parametric analysis was performed in [68] regarding the effect the elastic reflection mechanism on the multipactor susceptibility zones. However, this work was based on significant simplifications regarding the SEY, considering constant emission yield for low impact energies.

Here, we apply the proposed numerical technique in order to investigate how the multipactor threshold is affected by the elastic reflection mechanism. Using the SEY model of Lara *et al* [3], we achieve a realistic representation of the SEY for low impact energies, consistent with experimental data. In particular, the applied SEY model considers a smooth transition for the total SEY curve between the first crossover point, u_1, and zero impact energy, as depicted in Fig. 3.7. SEY trends corresponding both to strong and to weak elastic reflection, as reported in literature [64], can be sufficiently approached by changing the parameter $\varepsilon_{0,\text{elast}}$.

Considering the fundamental parallel plates configuration, a comprehensive parametric analysis has been performed assuming different surface materials. A representative example, illustrating how the susceptibility zones are affected by elastic reflection, is shown in Fig. 3.12. As expected, broader multipactor zones are obtained when the amount of reflected electrons increases, since a significant portion of low energy electrons are reflected rather than absorbed. This is particularly highlighted in the right part of the chart which corresponds to high fh values. As can be seen, the discrete susceptibility zones, coming form the high order resonant modes, tend to be incorporated into a single uniform zone. A similar behavior has been also reported in [67]. On the other hand, very interesting behavior is revealed at low fh values: the elastic reflection affects only the upper threshold whereas the lower threshold remains almost unchanged. In the following, we focus our analysis on the left part of the multipactor chart which attracts the most interest in multipactor analysis since it, typically, includes the lowest voltage value for which the discharge may occur.

In order to understand the peculiar behavior of elastic reflection observed for low fh values, let us consider the multipactor threshold as obtained without considering elastic reflection (i.e. the inner blue line in Fig. 3.12) and study the multipactor evolution around it. In the regions above the upper threshold, e.g. at point A, a resonant pattern in the electron motion such as in Fig. 3.13a is established which can be qualitatively described as follows. Due to the strong electric field (area above the upper threshold) or, equivalently, due to the small gap between plates (low fh) the emitted electrons from one of the plates, e.g. the bottom one, traverse the gap within a time shorter than half of the RF period. As a consequence, the secondary electrons on the opposite plate (here the top one) are exposed to a strong retarding field that makes them return and hit the same plate with low impact energy. The emitted electrons are "stuck" on the same plate until the electric field changes polarity and becomes favorable for accelerating motion towards the opposite wall. Depending on how intense the elastic reflection is, this "stuck" mechanism may result in either a strong or a negligible absorption for low and high $\varepsilon_{0,\text{elast}}$, respectively, explaining why the upper threshold moves towards higher voltages as $\varepsilon_{0,\text{elast}}$ increases.

Moving counter-clockwise around the threshold, we, next, focus on the area below the lowest multipactor threshold, represented by point B in Fig. 3.12. This area corresponds to the 1st order resonant mode and, consequently, the electrons follow a periodic motion

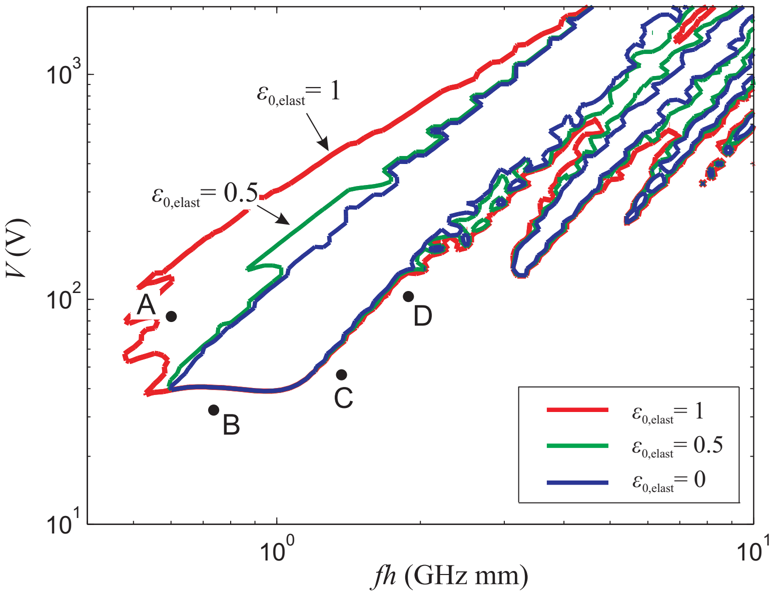

Figure 3.12.: Multipactor threshold considering different values for the elastic reflection coefficient $e_{0,\text{elast}}$. Parallel plates made of silver are considered.

traversing the gap after half a RF period, as depicted in Fig. 3.13b. However, since the secondary emission condition is not satisfied (area below the low secondary emission limit), the accelerated electrons do not acquire enough energy in order to initiate the emission of secondary electrons. Therefore, a resonant absorption mechanism governs the evolution of the phenomenon independently of how intense the elastic reflection is.

Moving further counter-clockwise, let us study the areas close to points C and D, where the threshold still remains unaffected. This region is placed below the minimum resonance limit required for achieving 1^{st} order periodic motion. As can be seen in Figs. 3.13c and 3.13d, the electrons follow a random-like motion and, consequently, they hit the boundaries with a spread spectrum of impact energies. Contrary to the areas above the upper threshold (point A) where the electrons are trapped and hit the surface of emission with very low velocity, here, the impact energy spectrum covers a broad range below the first crossover point, as Fig. 3.14 shows. As a consequence, a significant amount of electrons is absorbed even for the limiting case $\varepsilon_{0,\text{elast}} = 1$. Moving towards higher gap voltages, e.g. from point C to D, the impact energy spectrum spreads more, covering values that may be above the first crossover point, as can be seen in Fig. 3.14b. This implies that both absorption and secondary emission mechanism take place. For high voltages, the emission of true secondaries overcomes the absorption mechanism resulting in a global increase of the electron population. This trend becomes more intense as the elastic reflection coefficient, $\varepsilon_{0,\text{elast}}$, increases since absorption becomes weaker. This justifies the broad susceptibility zone achieved for $\varepsilon_{0,\text{elast}} = 1$ in the right part of the multipactor chart.

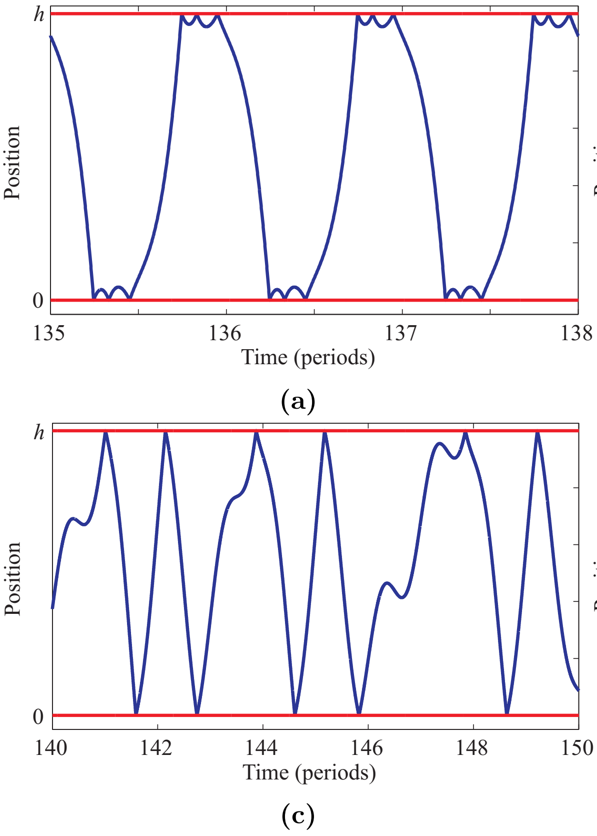

(a) (b)

(c) (d)

Figure 3.13.: Electron motion for the cases A, B, C and D as depicted in Fig. 3.12. a) point A: $fh = 0.65$ GHz mm and $V = 100$ V and b) point B: $fh = 0.75$ GHz mm and $V = 30$ V, c) point C: $fh = 1.35$ GHz mm and $V = 50$ V and d) point D: $fh = 1.9$ GHz mm and $V = 115$ V

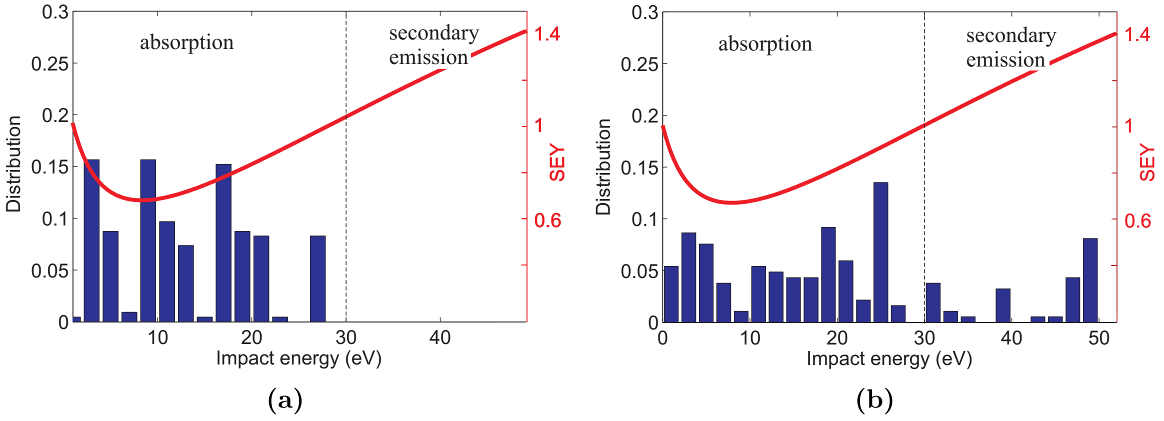

(a) (b)

Figure 3.14.: Distribution of impact energy for the cases C and D as depicted in Fig. 3.12. a) point C: $fh = 1.35$ GHz mm and $V = 50$ V and b)D: $fh = 1.90$ GHz mm and $V = 115$ V. For illustration purposes the SEY curve used in the example of Fig. 3.12 for $\varepsilon_{0,\mathrm{elast}} = 1$ is depicted, too. SEY values correspond to the right vertical axis.

3.5.2. Multipacting in coaxial lines

Among other structures, coaxial lines are essential parts in satellite systems. Typically, the space between the inner and the outer conductor is filled by a dielectric medium in order to mechanically support the coaxial structure. However, in many cases the dielectric medium is partially omitted in order to reduce the dielectric losses or the weight of the cable. Moreover, various gaps may appear in transitions between coaxial lines and connectors due to mechanical tolerances. In vacuum environments these air gaps may be evacuated exposing, thus, coaxial lines to the risk of a multipactor discharge

Considering the fundamental TEM mode, the electric field is unidirectional and, consequently, multipactor in coaxial lines can be fairly considered as a 1D problem. However, contrary to the 1D case of parallel plates, the field distribution in coaxial lines is not uniform. In particular, the electric field, E_r is proportional to the inverse of the radial position r, i.e $E_\mathrm{r} \propto 1/r$, meaning that it becomes stronger as approaching the inner conductor. Figure 3.15 depicts the field distribution in coaxial lines with different ratio between the outer and the inner radii, $r_\mathrm{o}/r_\mathrm{i}$. As can be seen, for small $r_\mathrm{o}/r_\mathrm{i}$ the electric field is relatively uniform resembling the field in parallel plates. However, as the ratio $r_\mathrm{o}/r_\mathrm{i}$ increases, the field becomes intensively inhomogeneous, especially near the inner conductor. Due to the inhomogeneous electric field, the electrons experience an average force that pushes them towards the outer conductor. This is the so called ponderomotive or Miller force that appears in inhomogeneous oscillating fields and makes charged particles drift towards weak field areas [69]. This mechanism may significantly affect multipacting in coaxial lines, especially when the ratio between the outer and the inner radii is high. As a result, single-side discharge may occur on the outer conductor in addition to the classical double-side multipacting between two surfaces [56].

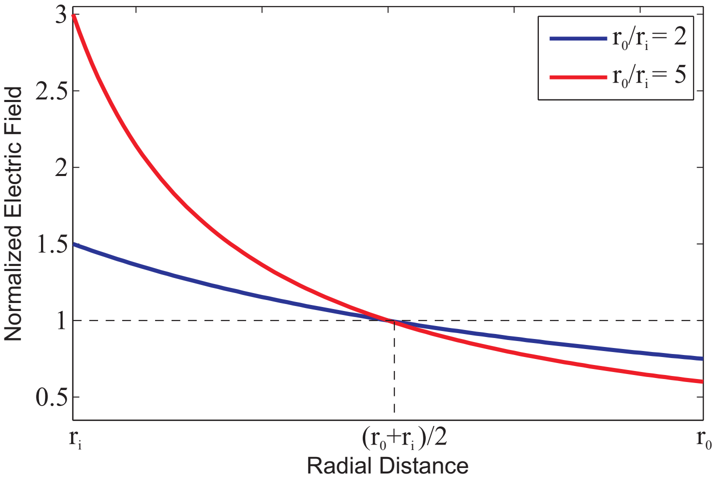

Figure 3.15.: Electric field distribution between the inner and the outer conductor in coaxial lines. The electric field component is normalized to the field at the middle point between the two conductors. The horizontal dashed line corresponds to the case of parallel plates.

Multipactor in coaxial lines has been studied in several works, numerically [57, 70–75], experimentally [61, 76, 77] and theoretically [56] as well. The main findings can be briefly described as follows. For small characteristic impedances, corresponding to low $r_\mathrm{o}/r_\mathrm{i}$, the discharge evolves like in parallel plates since the electric field is almost uniform [61, 73]. For instance, through experimental studies, Woo [61] showed that the multipactor threshold for a coaxial line of $Z = 50\ \Omega$ ($r_\mathrm{o}/r_\mathrm{i} = 2.3$) is pretty similar to the one obtained for parallel plates. As the characteristic impedance increases, the threshold is shifted towards higher values [61, 70, 73]. This means that the inhomogeneity of the electric field makes multipaction more difficult to occur. Moreover, another phenomenon has been reported for high Z: in addition to the classical double-side discharge single-side multipacting on the outer conductor may also occur due to the ponderomotive force [56, 71]. However, the 1st order double-side regime still remains the dominant multipactor mechanism for low frequencies, as shown in [57, 73].

Despite the clear qualitative overview provided in the literature, some aspects of the problem with particular interest has not been clarified yet. One of them is the effect of the characteristic impedance on the double-side discharges. Studies performed on the topic have derived different conclusions. By performing a theoretical study, Udiljak *et al* [56] argued that the voltage threshold of the 1st multipactor mode follows a $\propto (fh)^2$ scaling, where $h = r_\mathrm{o} - r_\mathrm{i}$, This implies negligible dependance on the characteristic impedance Z contrary to the measurement data of Woo [61] which revealed an increase on the threshold for higher Z. On the other hand, Somersalo *et al* [71] performed numerical studies and suggested a different scaling law as $\propto (fr_\mathrm{o})^2 Z^{3/2}$. However, this relation is only accurate for high values of $r_\mathrm{o}/r_\mathrm{i}$. Another subject that provoked debate in the literature is related with the single-side multipacting on the outer conductor. More specifically, although single-side discharge has been reported in numerical and theoretical studies it has not been detected by experiments, even for high $r_\mathrm{o}/r_\mathrm{i}$. Kossyi *et al* [77] stated that, due to the spread of emission velocities, a hybrid regime which combines both single- and double- side discharges occurs instead of a pure single-side multipacting.

Both topics, mentioned in the previous paragraph, trigger particular interest. Next, we apply the proposed numerical model in order to get a better insight on these subjects. Moreover, our analysis reveals a new resonant regime, not mentioned in literature, that may notably affect multipaction for high characteristic impedances.

fh dependance principle

Before continuing with the analysis of the phenomenon, let us, first, discuss the following issue: *can multipacting in coaxial lines be scaled with regards to the frequency-gap product?* Through the theoretical analysis of Section 3.3, we have seen that in the case of parallel plates the gap voltage, corresponding to certain multipactor modes, depends directly on the frequency-gap product, fh. Apparently, this is confirmed by the equations which describe the threshold limits, e.g. Eqs. (3.6) and (3.10). Qualitatively, such a dependance means that if the gap and the RF period increase with the same rate (e.g. both of them become double), the profile of the electron motion will remain the same. Therefore, for constant frequency-gap product , fh, the discharge will evolute under the same manner. Reasonably, a question raises whether a similar dependance also occurs in the case of coaxial lines.

Considering a certain $r_\mathrm{o}/r_\mathrm{i}$, the profile of the electric field, normalized to the gap between the electrodes, remains the same for different h. Our intuition for a similar fh dependance in the case of coaxial lines, as in parallel plates, is raised by the theoretical study of Woo and Ishimaru [78]. By normalizing the equation of motion, they proposed a similarity principle which demonstrates that a dependance of fh, as in parallel plates, should state for the case of coaxial lines, too. In order to confirm this statement, we performed several numerical experiments considering different gaps h. A representative example is illustrated in Fig. 3.16, depicting the multipactor threshold for three different gaps. As can be seen, although the gap between the inner and the outer conductor changes the multipactor threshold remains the same in terms of the frequency-gap product. Therefore, considering a certain characteristic impedance, multipacting depends directly on the fh product. Let us call this as the 'fh dependance principle'. The utility of this principle is reflected in the multipactor chart since the dimensions of the structure (gap) are incorporated in addition to the electric field parameters (frequency and voltage). Moreover, fh dependance allows the derivation of practical scaling laws regarding the multipactor threshold, as discussed later.

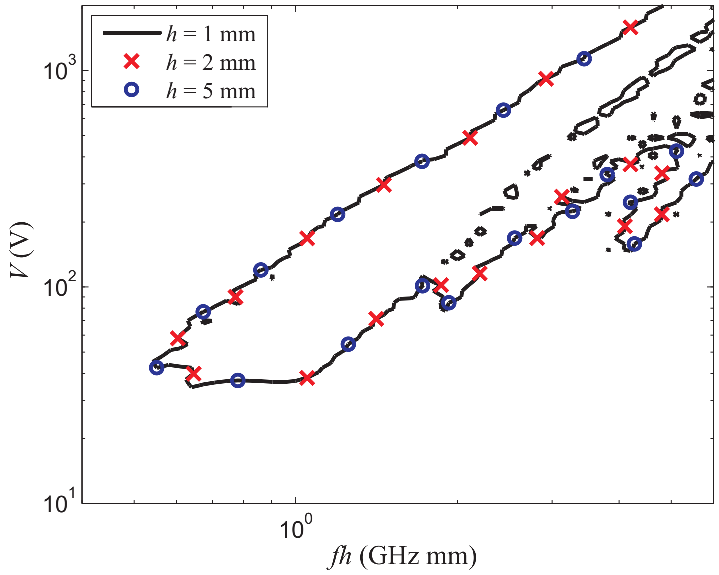

Figure 3.16.: Multipactor threshold for different gaps. A coaxial line made of copper, with a characteristic impedance equal to $Z = 50\ \Omega$, is considered.

Multipactor Chart

An overview of the discharge can be obtained through the multipactor chart. Due to the fh dependance principle, as described previously, the susceptibility zones in coaxial lines can be expressed as a function of the applied voltage and the frequency-gap product. This allows proper comparisons between coaxial lines with different characteristic impedances as well as comparison between coaxial lines and parallel plates. Figure 3.17 illustrates the multipactor chart as derived for three different characteristic impedances. For demonstration purposes, the case of parallel plates is also included.

First, let us try to figure out the main differences between multipacting in parallel plates and multipacting in coaxial lines. For this, we focus on the chart corresponding to the lowest characteristic impedance, i.e. $Z = 50\ \Omega$, and we compare it with the corresponding chart of parallel plates (see Figs. 3.17a and 3.17b). Starting from the left part of the chart, it can be seen that the fundamental mode results in pretty similar multipacting areas in both cases, noted as c_1 in the graphs. Both multipacting boundaries and intensity are in good agreement. The main differences seem to appear beyond the 1^{st} order mode, as moving towards higher fh values. As can be observed, different multipactor zones appear in the case of the coaxial line. These zones correspond to hybrid modes, as the one denoted with $h_{1,3}$ in Fig. 3.17b. The main reason of the occurrence of hybrid modes instead of high order classical modes is the fact that the hybrid modes fit well with the non-symmetrical profile of the electric field inside coaxial lines. As the characteristic impedance increases, we can notice that the lower threshold of the fundamental mode is shifted to higher voltage values. This implies that multipaction becomes more difficult to occur as the ratio between the outer and the inner radii increases since the increasing non-uniformity of the electric field for higher Z makes multipaction more difficult to occur. In addition, single-sided multipaction starts to appear as the characteristic impedance increases. As Fig. 3.18 illustrates, for high characteristic impedances, the multipactor zones corresponding to high frequency-gap products as well as to high gap voltages are dominated by single-sided multipaction.

Above all, what we observe for coaxial lines with high characteristic impedances, is the existence of a isolated multipactor zone below the fundamental mode. This zone corresponds to the hybrid mode $h_{1,3}$. A possible existence of this isolated zone means that the multipactor threshold in that area is getting significantly lower. To the author's best knowledge, it is the first time that this multipactor zone is reported for high characteristic impedances. However, we should mention that the color intensity corresponding to this isolated zone is relatively low, meaning that depending on the sensitivity of the SEY properties of the surface materials this multipactor regime probably does not appear.

3.6. Summary

In this chapter, we, first, reviewed the single electron approach underlying the assumptions behind it. Then, based on the single electron model, a theoretical analysis has been presented for the parallel plates case in order to get a physical insight to the multipactor mechanisms. As a result, the multipactor chart that depicts the susceptibility zones for different multipactor modes has been obtained. Special emphasis was given to explaining the mechanisms affecting the multipactor threshold. After the theoretical analysis, we have developed a generalized technique, based on the single electron approach. The proposed numerical technique was validated through comparisons with theoretical, numerical results as well as with measurements. Very good agreement with the theoretical and numerical results has been observed, while a fair agreement with the measurements has been noticed for the upper and the lower threshold. By applying the proposed method, two topics of particular interest in multipactor analysis have been studied: first, the effect of electric reflection of impact electrons on the multipactor onset and, second, multipactor in coaxial lines focusing on the effect of the characteristic

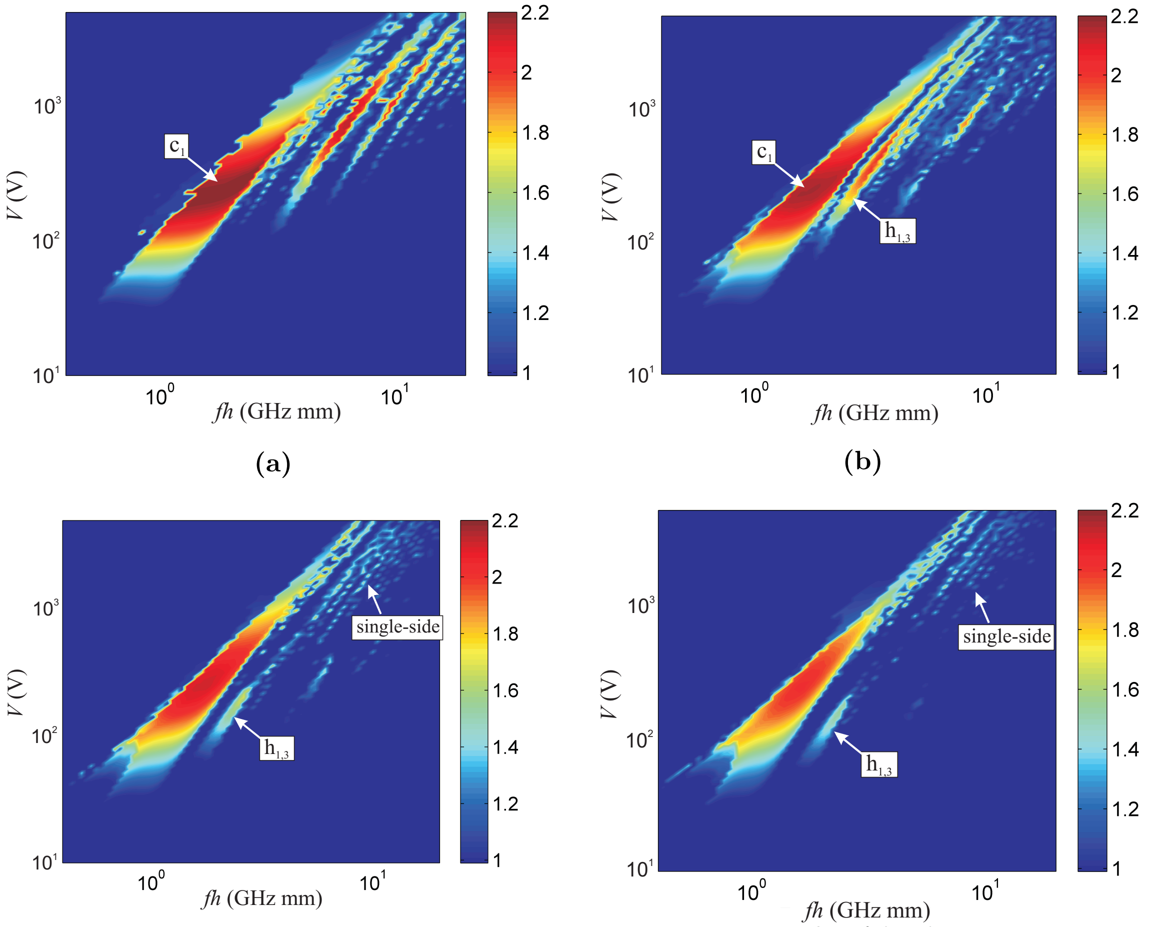

(a) **(b)** **(c)** **(d)**

Figure 3.17.: Multipactor chart in coaxial lines. Color intensity represents the geometric mean SEY value. Both electrodes are made of copper. Different characteristic impedances, Z are considered: a) parallel plates ($Z \to 0\ \Omega$), b) $Z = 50\ \Omega$, c) $Z = 75\ \Omega$ and d) $Z = 100\ \Omega$.

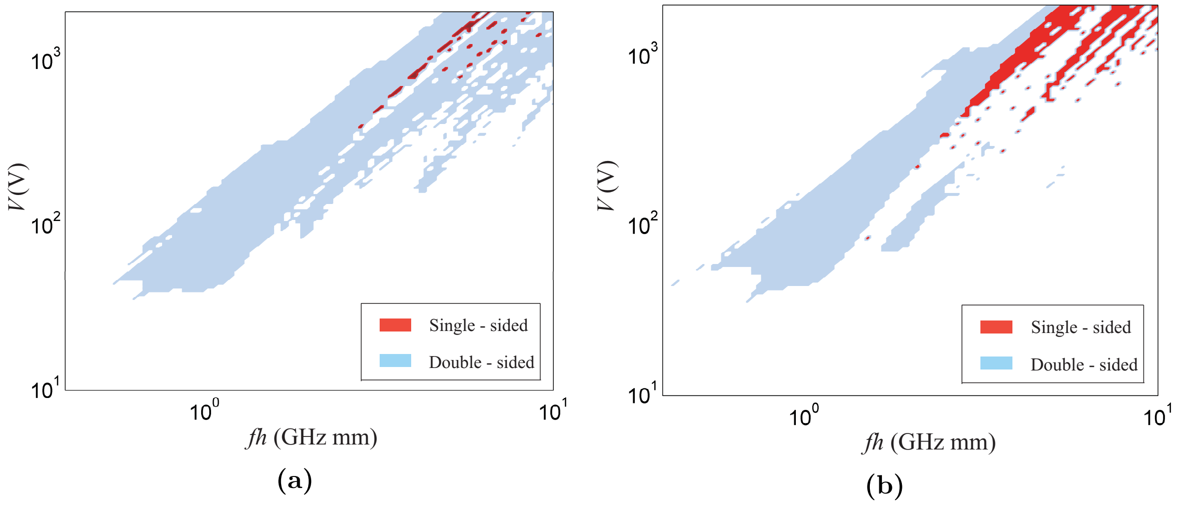

(a) **(b)**

Figure 3.18.: Single-sided multipaction in coaxial lines considering a characteristic impedance of a) $Z = 50\ \Omega$ and b) $Z = 100\ \Omega$. The SEY parameters of silver have been used (see Table 3.2).

impedance. it has been shown that the lower multipactor threshold corresponding to the 1st order multipactor mode is not affected by the elastic reflection mechanism. The developed 1D technique is used in Chapter 4 in order to investigate multipactor in the presence of dielectrics.

4. Multipactor in the Presence of Dielectrics

4.1. Introduction

Dielectric materials are commonly met in microwave components of modern satellite systems. Coaxial connectors as well as transitions between microstrip lines and monolithic microwave integrated circuits (MMICs) are typical examples where various gaps between metallic and dielectric surfaces appear. Under vacuum conditions, like in space environment, these components are exposed to the risk of a multipactor discharge.

Multipacting in the presence of dielectrics involves the following peculiarity: as the discharge evolves, a surface charge is developed on the dielectric walls [25]. As a consequence, a DC-like electric field, changing after electron collisions on the dielectric surfaces, occurs. If a large amount of charge is accumulated on the dielectric surfaces, this field can significantly affect the electron dynamics and, consequently, the evolution of the discharge.

The effect of dielectrics on multipacting has triggered intense interest in the particle accelerators community. More specifically, the DC-like field due to the surface charge may result in a single-surface discharge in dielectric RF windows, as has been reported in several studies [11, 22–27]. A similar single-sided regime may also appear in dielectric loaded accelerator (DLA) structures [28–30]. The underlined feature of these applications is the existence of a RF electric field component parallel to the dielectric surface that constitutes the dominant mechanism responsible for the oscillating motion of the electrons. On the other hand, little is known about multipactor discharges in loaded microwave components that operate in quasi-TEM or TE modes. Such configurations are of particular interest for the satellite community, as mentioned in the first paragraph. Contrary to the above mentioned cases of RF windows and DLA structures, transverse electric field modes imply that the electrons motion is dominated by a RF field component perpendicular to the dielectric surface. Some works have numerically dealt with multipactor discharge inside a parallel-plate waveguide partially loaded by a dielectric slab [31, 32]. Results revealed an interesting self-extinguishing mechanism that affects the long-term evolution of the phenomenon. However, these studies were based on a critical simplification by neglecting the induced charges on the metallic walls due the surface charge on the dielectric.

As already mentioned in Section 2.5 the induced charge is one of the factors that can significantly affect the long-term evolution of a multipactor discharge. Motivated by this fact, here we revise the problem of multipactor in parallel-plates loaded by a single dielectric layer taking into account the effect of the induced charges. Special emphasis is given to the long-term evolution of the discharge. Two different approaches are followed. First, the generalized single electron model, as proposed in the Chapter 3, is properly modified in order to consider the saturation mechanisms including the effect of the surface charge on the dielectric. By applying it, a global overview of the phenomenon is obtained. However, by its nature, the single electron model does not account for the statistics of the secondary emission. As a second approach, a 3D multipactor model taking into account the stochastic behavior of the secondary emission mechanism is developed. In order to include the space charge effects, a novel image method, able to evaluate the Green Function (GF) in multilayer shielded media, is proposed (see Chapter 5). The image method is incorporated in the 3D multipactor solver in order to investigate the long-term evolution of the discharge.

4.2. Theory

The configuration under study is depicted in Fig. 4.1. The free electrons are accelerated in the vacuum space due to the transversal component of the RF field and under certain resonant conditions they oscillate between the upper metallic surface and the dielectric slab. When impinging on a surface, they can be reflected, absorbed or even cause the emission of secondary electrons depending on the impact energy. A special phenomenon takes place when the electrons impact on the dielectric surface. The surface can be locally charged positively or negatively in case of a secondary emission or an electron absorption, respectively. For example, when an electron is absorbed on the dielectric slab, it remains very close to the surface since dielectrics are very good isolators. Then, after many impact events, a charged sheet is composed on the dielectric surface.

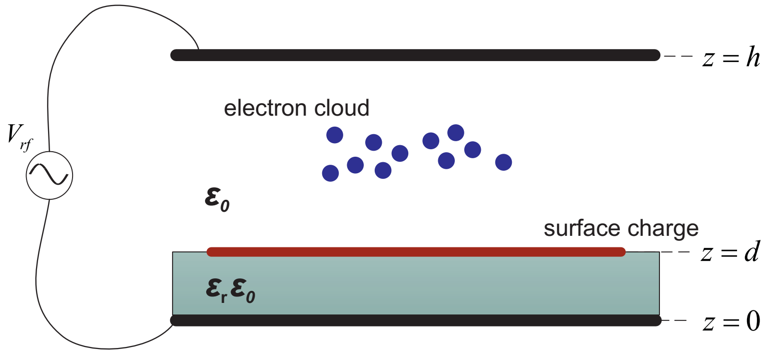

Figure 4.1.: Configuration under study: A parallel-plate waveguide loaded by a single dielectric layer.

During the multipactor onset, i.e. the phase when the electron population increases, the electron motion is dominated by the RF electric field. However, as the electron cloud augments, the surface charge density on the slab also increases since more and more electrons impinge on the dielectric surface. The electric field produced by the surface charge introduces an asymmetry to the total electric field, thus, perturbing the resonant motion of the electrons. Moreover, as the electron population increases, there are two other saturation mechanisms that prevent the infinite augmentation of the electron cloud. First, an induced charge occurs on the metallic surfaces due to the free electrons. In addition, the mutual interaction between the free particles affects the electron motion, too. The aforementioned mechanisms can be briefly described in the following expression for the total electric field,

$$\mathbf{E}_{\text{total}} = \mathbf{E}_{\text{rf}} + \mathbf{E}_{\text{diel}} + \mathbf{E}_{\text{induced}} + \mathbf{E}_{\text{coulomb}}, \tag{4.1}$$

where $\mathbf{E}_{\text{diel}}$ is the electric field produced by the surface charge on the dielectric, $\mathbf{E}_{\text{induced}}$ the electric field due to the induced charges on the metal plates and $\mathbf{E}_{\text{coulomb}}$ the field due to the direct mutual interaction between electrons.

4.3. 1D Approach

In Chapter 3 we developed a 1D model in order to investigate the initial phase of the multipactor evolution, i.e. the existence of an electron avalanche or not. Despite its simplicity, the developed method is characterized by a generalized concept since it is able to consider any 1D electric field distribution. Therefore, in addition to the applied RF field, the electric field due to space charge effects or due to the surface charge on the dielectric could be also incorporated in a multipactor analysis. This allows us to advance a step further and to use the single electron model in order to investigate the long-term evolution of the discharge by considering the saturation mechanisms.

Let us discuss how the long-term multipactor evolution can be modeled by applying the single electron approach. Three distinguishable saturation mechanisms may occur in the investigated problem, namely the electric field due to the induced charges, due to the mutual interactions between electrons (Coulomb field) and due to the surface charge on the dielectric. As discussed in Chapter 3, the single electron approach assumes that all electrons move together with the same speed composing an infinitesimally thin sheet. This involves an inherent limitation in considering the mutual interaction between electrons: due to the repelling nature of the Coulomb force, the mutual interaction between electrons would imply a spreading of the thin electron sheet, contrary to the principle of the single electron model. Therefore, the mutual interactions cannot be modeled in the single electron approach. However, the space charge effect* can be approached by considering the induced charges as have been suggested in some previous works which have studied the steady state in case of empty parallel plates [18, 79]. Then, the long-term evolution can be modeled by taking into account the electric field due to the surface charge on the dielectric and due to the charges induced on the metal plates, corresponding to $\mathbf{E}_{\text{diel}}$ and $\mathbf{E}_{\text{induced}}$ of Eq. (4.1), respectively.

Based on the single electron approach, we properly modify the 1D numerical technique presented in Section 3.4.1 in order to investigate the multipactor steady-state in parallel plates partially loaded by a dielectric layer. For this, the electric field due to the surface charge and due to the induced charges are taken into account as discussed in the next Section. A schematic representation of the applied model is given in Fig. 4.2.

4.3.1. Formulation

The analysis starts by placing an effective electron between the dielectric surface and the upper metal plate. Similarly to the analysis of Section 3.4.1, the effective electron represents the total electron population that is assumed to compose an electron sheet, as Fig. 4.2 illustrates. Then, the effective electron is forced by a total electric field coming from the applied RF

---

[*] As mentioned in Section 2.5, the space charge effect includes both the effect due the direct mutual interaction and due the induced charges.

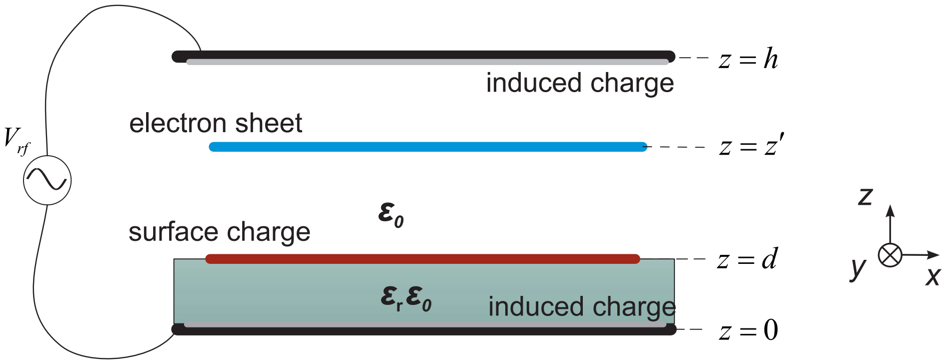

Figure 4.2.: The proposed 1D model for the investigation of the long-term multipactor evolution in parallel plates loaded by a single dielectric slab. The electron population is represented by an electron sheet, according to the single electron approach (see Chapter 3). A homogeneous surface charge is considered on the dielectric surface. Its intensity changes after electron collisions with the dielectric slab. Saturation is modeled by considering the field due to the surface charge and due to the charges induced by the electron sheet on the metal plates

excitation, the surface charge on the dielectric and the induced charges on the metal plates. This field can be expressed by the following equation

$$\mathbf{E}_{\text{total}} = \mathbf{E}_{\text{rf}} + \mathbf{E}_{\text{diel}} + \mathbf{E}_{\text{induced}}, \tag{4.2}$$

where $\mathbf{E}_{\text{rf}}$ is the input RF field, $\mathbf{E}_{\text{induced}}$ the field produced by the image of the electron sheet through the plates and $\mathbf{E}_{\text{diel}}$ the field produced by the surface charge on the dielectric. It should be noted that $\mathbf{E}_{\text{induced}}$ is the field that the electron sheet causes on itself through the charges it induces on the plates. Hence, let us call this field as 'self-field'. Moreover, note that, compared to Eq. (4.1), the Coulomb field has been omitted as explained in the introduction of Section 4.3.

In order to evaluate the electric field we make use of the superposition principle considering the two following problems: a) in the first problem the RF excitation is considered while the electron sheet and the surface charge are omitted and b) in the second one the electron sheet and the surface charge are considered while the RF excitation is set to zero. Note that in the second problem the two metal plates are both on the same potential since $V_{\text{rf}} = 0$. Without loss of generality, let this common potential be equal to zero.

Let us start with the second problem, that is considering only the electron sheet and the surface charge on the dielectric. The field due to the surface charge can be considered as a DC-like electric field the density of which changes after collisions of the electron sheet on the dielectric. Regarding the field due to the electron sheet, although the accelerated electrons result in a time-dependent distribution of the induced charges, the retardation effects can be fairly neglected since the velocity of the moving electrons is typically much lower than the speed of light and the distance between the metal plates is sufficiently small. Therefore, an electrostatic approach can be followed in order to evaluate both the self-field, $\mathbf{E}_{\text{induced}}$ and the DC-like field due to the surface charge, $\mathbf{E}_{\text{diel}}$.

To simplify our analysis, let us assume a single sheet, with a charge density σ, placed between the dielectric surface ($z = d$) and the upper metal plate ($z = h$). Then, if the considered sheet is placed at $z_{\text{sheet}} = z'$ it corresponds to the moving electron sheet while if it is placed at $z_{\text{sheet}} = d$ it corresponds to the surface charge on the dielectric. Applying the Poisson equation, which takes the following form in the considered 1D case,

$$\frac{\partial^2 \varphi}{\partial z^2} = -\frac{\sigma_{\text{sheet}}}{\varepsilon_0} \delta \left(z - z_{\text{sheet}} \right), \tag{4.3}$$

as well as the appropriate boundary conditions,

$$\varphi \left(h \right) = 0 \tag{4.4a}$$

$$\varphi \left(0 \right) = 0 \tag{4.4b}$$

$$\varphi \left|_{z=d^-} = \varphi \right|_{z=d^+} \tag{4.4c}$$

$$\varepsilon_r \frac{\partial \varphi}{\partial z} \left|_{z=d^-} = \frac{\partial \varphi}{\partial z} \right|_{z=d^+}, \tag{4.4d}$$

one can evaluate the potential $\varphi(z)$ between the plates. Then, by applying the negative gradient to the potential for $d < z < h$ we obtain the electric field in the vacuum space as follows:

$$\mathbf{E}_{\text{sheet}} = \begin{cases} \mathbf{E}_{\text{below}} = \frac{\sigma}{\varepsilon_0} \frac{\varepsilon_r (h - z_{\text{sheet}})}{\varepsilon_r h - (\varepsilon_r - 1) d} \hat{\mathbf{z}}\,, & \text{if } d < z < z_{\text{sheet}} \\ \mathbf{E}_{\text{above}} = \frac{\sigma}{\varepsilon_0} \frac{\varepsilon_r z_{\text{sheet}} - (\varepsilon_r - 1) d}{\varepsilon_r h - (\varepsilon_r - 1) d} \hat{\mathbf{z}}\,, & \text{if } h > z > z_{\text{sheet}} \end{cases} \tag{4.5}$$

Using the above expression, the next step is to evaluate the field on the electron sheet due to the electron sheet itself as well as due to the surface charge developed on the dielectric. Since the electron sheet moves above the dielectric interface, the field due to the surface charge, $\mathbf{E}_{\text{diel}}$, can be directly obtained by the expression $\mathbf{E}_{\text{above}}$ of Eq. (4.5) substituting $z_{\text{sheet}} = d$ and $\sigma = \sigma_{\text{diel}}$, where σ_{diel} is the density of the surface charge on the dielectric. Then, the electric field component $\mathbf{E}_{\text{diel}}$ gets the following form:

$$\mathbf{E}_{\text{diel}} = \frac{\sigma_{\text{diel}}}{\varepsilon_0} \frac{d}{\varepsilon_r h - \left(\varepsilon_r - 1 \right) d} \hat{\mathbf{z}}. \tag{4.6}$$

On the other hand, the evaluation of the self-field, $\mathbf{E}_{\text{induced}}$, is not as straightforward as the evaluation of $\mathbf{E}_{\text{diel}}$. In the case of the self-field, the electric field needs to be evaluated on the position of the source, that is the position of the electron sheet. As can be noticed in Eq. (4.5), the electric field is discontinuous at the electron sheet position. In order to manipulate this discontinuity let us express the field $\mathbf{E}_{\text{sheet}}$ as the sum of the field that the electron sheet produces in the free space, $\mathbf{E}_{\text{sheet,fs}}$, plus the field due to its image charge $\mathbf{E}_{\text{sheet,imag}}$:

$$\mathbf{E}_{\text{sheet}} = \mathbf{E}_{\text{sheet,fs}} + \mathbf{E}_{\text{sheet,imag}}. \tag{4.7}$$

Then, the electric field component $\mathbf{E}_{\text{sheet,fs}}$ is discontinuous at z_{sheet}. Indeed, an infinite surface charge in the free space, with charge density σ, produces an electric field $\mathbf{E}$ so that $2\varepsilon_0 \mathbf{E} = \sigma \hat{\mathbf{n}}$, where $\hat{\mathbf{n}}$ is the normalized vector pointing to the 'outer' side of the surface. This means that the field below and above the surface charge in the free space has the same amplitude but different direction,

$$\mathbf{E}_{\text{sheet,fs}}\left(z_{\text{sheet}}^{+}\right) = -\mathbf{E}_{\text{sheet,fs}}\left(z_{\text{sheet}}^{-}\right). \tag{4.8}$$

On the other hand, the field due to the image charge at the sheet position is continuous since no sources are placed at z_{sheet}. Therefore,

$$\mathbf{E}_{\text{sheet,imag}}\left(z_{\text{sheet}}^{+}\right) = \mathbf{E}_{\text{sheet,imag}}\left(z_{\text{sheet}}^{-}\right) = \mathbf{E}_{\text{induced}}, \tag{4.9}$$

where $\mathbf{E}_{\text{induced}}$ is the self-field, as defined in Eq. (4.2) that coincides with the field due to the image charges, $\mathbf{E}_{\text{sheet,imag}}$, when the observation point is the electron sheet position, i.e. $z_{\text{sheet}} = z'$. Taking into account Eq. (4.7) we can derive the expressions for the field above and below the sheet as

$$\mathbf{E}_{\text{sheet,imag}}\left(z_{\text{sheet}}^{+}\right) = \mathbf{E}_{\text{sheet}}\left(z_{\text{sheet}}^{+}\right) - \mathbf{E}_{\text{sheet,fs}}\left(z_{\text{sheet}}^{+}\right) \tag{4.10a}$$

and

$$\mathbf{E}_{\text{sheet,imag}}\left(z_{\text{sheet}}^{-}\right) = \mathbf{E}_{\text{sheet}}\left(z_{\text{sheet}}^{-}\right) - \mathbf{E}_{\text{sheet,fs}}\left(z_{\text{sheet}}^{-}\right). \tag{4.10b}$$

Substituting the expressions of Eqs. (4.8) and (4.9) in Eq. (4.10) and, then, adding the corresponding parts of Eqs. Eq. (4.10a) and Eq. (4.10b) we can easily evaluate the self-field, $\mathbf{E}_{\text{induced}}$, on the electron sheet as:

$$\mathbf{E}_{\text{induced}} = \frac{1}{2}\left(\mathbf{E}_{\text{above}} + \mathbf{E}_{\text{below}}\right), \tag{4.11}$$

where $\mathbf{E}_{\text{above}}$ and $\mathbf{E}_{\text{below}}$ are given by Eq. (4.5). Finally, substituting $z_{\text{sheet}} = z'$ and $\sigma = \sigma_{\text{el}}$ in the expressions of $\mathbf{E}_{\text{above}}$ and $\mathbf{E}_{\text{below}}$ as given by Eq. (4.5), the self-field of Eq. (4.11) yields

$$\mathbf{E}_{\text{induced}} = \frac{\sigma_{\text{el}}}{2\varepsilon_0}\frac{2\varepsilon_r z' - (\varepsilon_r - 1)\,d - \varepsilon_r h}{\varepsilon_r h - (\varepsilon_r - 1)\,d}, \tag{4.12}$$

where σ_{el} is the charge density of the moving electron sheet.

Up to now, we have evaluated the electric field on the moving electron sheet due to electron sheet itself ($\mathbf{E}_{\text{induced}}$, as given in Eq. (4.12)) and due to the surface charge on the dielectric ($\mathbf{E}_{\text{diel}}$, as given in Eq. (4.6)). The final step in order to evaluate the total electric field, $\mathbf{E}_{\text{tot}}$, is to derive the expression for the RF field, $\mathbf{E}_{\text{rf}}$. For this, let us, now, consider only the RF excitation omitting the effect of the electron sheet and the surface charge on the dielectric. Contrary to the empty parallel plates, the filled parallel plates waveguide cannot support TEM modes due to the inhomogeneity introduced by the dielectric slab. In fact, the examined structure supports hybrid modes, called longitudinal section magnetic (LSM) and electric (LSE) modes, with zero transverse component of magnetic and electric field, respectively [80]. Since we focus on double-sided multipaction, we assume that the fundamental LSM mode is excited so that the transverse electric field forces the motion of electrons along the z axis. Assuming a small dielectric contrast between the vacuum and the dielectric slab, ε_{r}, or low RF frequency, the profile of the electric field in the transverse plane fairly resembles the one of the classical TEM-mode in empty parallel plates waveguide. Then, an electrostatic approach can be followed in order to evaluate the transverse electric field component, as has been proposed in [31], meaning that the electric potential satisfies the Laplace equation.

Let us consider a time varying voltage between the metal plates as $V_{\mathrm{rf}} = V \sin(\omega t)$. Then, under the electrostatic approximation as described in the previous paragraph, the electric potential φ satisfies the Laplace equation in each uniform area (vacuum and dielectric):

$$\frac{\partial^2 \varphi_{\mathrm{i}}}{\partial z^2} = 0, \quad \mathrm{i} = 1, 2, \tag{4.13}$$

where the index i refers to the vacuum ($i = 1$) and to the dielectric space ($i = 2$). By integrating Eq. (4.13) in terms of z, one can easily show that the electric field is spatially constant in each area i. Focusing on the vacuum area, (which is the area of our interest since the electron sheet moves there) the electric field can be, then, expressed as follows:

$$\mathbf{E}_{\mathrm{rf}} = \frac{V_{\mathrm{gap}}}{h-d} \sin(\omega t)\, \hat{\mathbf{z}}, \quad d < z < h, \tag{4.14}$$

where V_{gap} is the peak voltage between the upper metal plate and the dielectric surface. By applying the boundary conditions, the gap voltage V_{gap} is obtained as

$$V_{\mathrm{gap}} = V \frac{\varepsilon_{\mathrm{r}} (h-d)}{\varepsilon_{\mathrm{r}} h - d(\varepsilon_{\mathrm{r}} - 1)}. \tag{4.15}$$

Once the expressions for the electric field components are known the total field on the moving electron sheet, $\mathbf{E}_{\mathrm{tot}}$, can be evaluated by the sum of $\mathbf{E}_{\mathrm{rf}}$, $\mathbf{E}_{\mathrm{diel}}$ and $\mathbf{E}_{\mathrm{induced}}$ as given in Eqs. (4.14), (4.6) and (4.12), respectively. Then, the motion of the effective electron is numerically tracked using a Runge-Kutta differential scheme as in the 1D numerical technique that was presented in Section 3.4.1. What changes here is that the saturation mechanisms are taken into account in addition to the RF excitation.

When a collision of the effective electron with a boundary is detected, the SEY model of [3] is applied in order to estimate the electron population. In particular, after an impact, either on the metallic or on the dielectric plate, the charge density of the electron sheet, σ_{el}, is updated as follows:

$$\sigma_{\mathrm{el}}^{i} = \delta_i \sigma_{\mathrm{el}}^{i-1}, \tag{4.16}$$

where δ_i is the SEY value at the i^{th} impact event and σ_{el}^{i} the updated charge density after the impact. On the other hand, when the electron sheet impinges on the dielectric slab, the density of the surface charge, σ_{diel}, also changes in addition to the charge density of the electron sheet. As explained in Section 4.2, an absorption of electrons ($\delta < 1$) in the dielectric slab yields a negative charge on the dielectric, $\sigma_{\mathrm{diel,add}}$ in addition to the existing one on the surface, σ_{diel}. In terms of charge density, this charge can be expressed as

$$\sigma_{\mathrm{diel,add}}^{j} = \sigma_{\mathrm{el}}^{i-1} - \sigma_{\mathrm{el}}^{i}, \tag{4.17}$$

where the index j refers only to impact events on the dielectric surface while the index i

refers to any impact event (either on the upper metal plate or on the dielectric surface)[†]. Substituting Eq. (4.16) into Eq. (4.17) yields

$$\sigma^{j}_{\text{diel,add}} = (1 - \delta_i)\, \sigma^{i-1}_{\text{el}}. \tag{4.18}$$

The above expression also holds for the case that there is emission of secondary electrons instead of absorption. Indeed, a secondary emission after an impact on the dielectric surface ($\delta > 1$) results in a positive charge on the dielectric which compensates the loss due to the emitted electrons. If $\sigma_{\text{el,add}}$ is the increase of the charge density of the moving electron sheet, then the corresponding positive charge on the dielectric will be exactly the opposite, i.e. $\sigma_{\text{diel,add}} = -\sigma_{\text{el,add}}$. Since $\sigma^{i}_{\text{el,add}} = \sigma^{i}_{\text{el}} - \sigma^{i-1}_{\text{el}}$ is the increase of charge density of the electron sheet after the i^{th} impact on the dielectric, the corresponding $\sigma_{\text{diel,add}}$ density will be again given by Eqs. (4.17) and (4.18). Therefore, when the electron sheet impinges on the dielectric slab, the density of the surface charge on the interface, σ_{diel}, changes according to the formula:

$$\sigma^{j}_{\text{diel}} = \sigma^{j-1}_{\text{diel}} + (1 - \delta_i)\sigma^{i-1}_{\text{el}}. \tag{4.19}$$

Summarizing, the algorithm starts by placing the effective electron (i.e. the electron sheet) at a random position in the vacuum area. In this analysis, the dielectric surface is assumed to be uncharged at $t = 0$, i.e. $\sigma^{0}_{\text{diel}} = 0\ e/m^2$, while the moving electron sheet has a low initial charge density $\sigma^{0}_{\text{el}} = 1\ e/\text{m}^2$, where e is the charge of a single electron ($e \approx -1.602 \times 10^{-19}$C). Then, the numerical integrator tracks the motion of the effective electron taking into account the RF electric field, $\mathbf{E}_{\text{rf}}$ plus the self-field of the moving electron sheet, $\mathbf{E}_{\text{induced}}$ as well as the field due to the surface charge on the dielectric, $\mathbf{E}_{\text{diel}}$. The charge density of the electron sheet, σ_{el}, changes after any impact event according to Eq. (4.16), while the density of the surface charge σ_{diel} is only updated after collisions of the moving sheet with the dielectric slab according to Eq. (4.19). The updated values of charge densities σ_{el} and σ_{diel} are, then, used in order to evaluate the total electric field. This procedure continues until a preselected time period, t_{f} is reached. Typically, a few hundreds of RF periods (200-500 RF cycles) are fairly sufficient in order to study the long-term evolution of the phenomenon.

4.3.2. Analysis

In this section we apply the above described model in order to study the effect of the surface charge, developed on the dielectric, on the long-term multipactor evolution. Before continuing with the analysis, let us briefly summarize what has been derived by previous works. To the author's best knowledge, the considered configuration has been studied in a few works by Torregrosa, Coves and their group in [31, 32, 81]. Their studies have reported that the surface charge on the dielectric leads to a self-extinguishing mechanism that makes the electron cloud disappear after its population reaches a maximum level. On the other hand, the dielectric surface remains charged. A qualitative overview of the results that have been presented in their studies is given in Fig. 4.3.

[†] Note that for each j there is a corresponding index i, i.e. $j \to i$. However, the opposite does not hold since the impact events i compose a superset of impact events j.

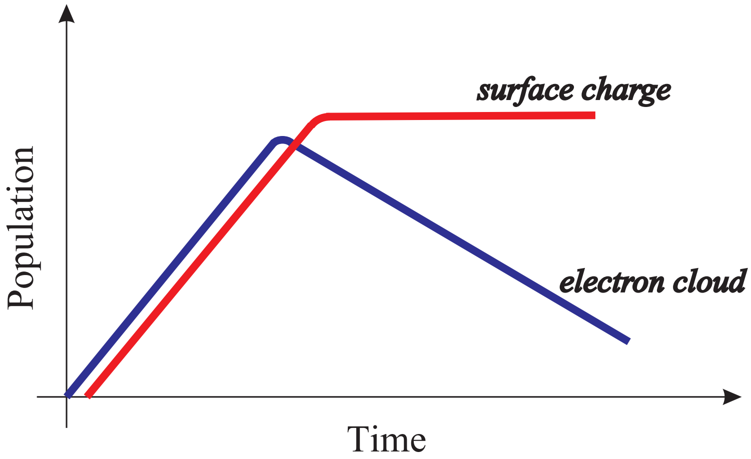

Figure 4.3.: Qualitative representation of the results reported in literature [31, 32],. The electron population and the surface charge on the dielectric are simultaneously increasing. When the surface charge becomes high the DC-field due to the surface charge leads to the decrease of the electron population. Note, that both positive and negative net charge on the dielectric surface has been reported in the literature. However, for both cases result the electron cloud disappears at the end.

The behavior illustrated in Fig. 4.3 can be explained as follows. Assume that the conditions needed for multipacting are satisfied. Then, as the free electrons hit the boundaries they provoke the emission of secondary electrons. On the other hand, a positive surface charge develops on the vacuum-dielectric interface which is augmented after impacts of the electrons on the dielectric slab. This yields a DC-like electric field that attracts the electrons on the dielectric slab. During the first phase of the multipactor evolution, (positive slope in Fig. 4.3), the motion of the electrons is dominated by the RF field, since the DC-field is relatively weak (due to low surface charge). However, as the electron population increases, the surface charge on the dielectric increases, too, and, consequently, the attractive force due to the DC-field becomes considerable. Then, the electrons tend to hit the dielectric surface with higher impact energy and, in parallel, the upper metal plate with lower energy. This results in the following mechanism: a decrease of electron population after impacts on the metal plate and an increase after impacts on the dielectric slab. Due to this mechanism the positive surface charge becomes even stronger and the process is self-sustained. At the end, the DC-like field leads to the break of the conditions needed for multipacting and, consequently, the free electrons disappear.

The above description provides an explanation how the DC-like field due to the surface charge on the dielectric can affect the long-term evolution of the phenomenon. However, as already mentioned, apart from the surface charge, other mechanisms, like the induced charges, may also affect the long-term multipactor evolution. The works that have reported the trend illustrated in Fig. 4.3 have neglected the induced charges. In particular, Torregrosa *et al* in [31] have used a single electron approach neglecting any space charge effect. In order to incorporate the effect of the the dielectric slab, they have considered the electric field due to the surface charge on the dielectric, however, evaluating it without considering the boundaries of the problem. Later, Coves *et al* [32] improved the previous model of Torregrosa by considering many particles instead of a single effective electron. By this, the statistics of the multipactor discharge have been better modeled. However, the electric field coming either from the electron cloud or from the surface charge on the dielectric has been approximated by considering the free space, neglecting, thus, the induced charge on the plates.

Next, we analyze the effect of the surface charge on the dielectric taking into account the induced charge, as described in Section 4.3.1. Comparing to the above mentioned studies, which were based on the free-space assumption, in our analysis the DC-like field due to the surface charge on the dielectric is properly evaluated by considering the boundaries of the examined configuration. Let us consider the following configuration: a parallel-plate waveguide with a distance between the plates equal to $h = 1.1$mm loaded by a dielectric slab of $d = 0.1$mm. The secondary emission properties of silver (see Table 3.2) have been chosen for the upper metallic plate. A relative permittivity of $\epsilon_r = 3$ has been considered for the slab, while the same SEY properties of silver have been considered for the dielectric surface, too [‡].

As a first step, we focus our analysis only on the initial phase of the phenomenon, namely the multipactor onset, in order to study under which conditions the discharge occurs. During the multipactor onset, the electron population is supposed to evolve as in the case of empty parallel plates. Indeed, the saturation mechanisms can be considered negligible since the electron population and the surface charge on the dielectric are both low at the very beginning (the dielectric is assumed to be initially uncharged, as mentioned in section 4.3.1). Therefore, the DC-like field due to the surface charge on the dielectric is expected not to affect the initial phase of the phenomenon. As a consequence, the analysis presented in Chapter 3 for the case of empty parallel plates can be also applied here as a first step in our study. To do so, the considered configuration including the dielectric slab has to be transformed into an equivalent one of empty parallel plates. This can be done as following: we consider that a parallel plates waveguide with a gap equal to $h' = h - d$ that is excited by an RF voltage equal to $V'_{\mathrm{rf}} = V_{\mathrm{gap}} \sin(\omega t)$. Then, an overview regarding the multipactor onset in the considered configuration can be obtained through the multipactor chart, as Fig. 4.4 depicts.

Once the susceptibility zones are obtained the next step is to study the long-term evolution of the phenomenon by taking into account the saturation mechanisms. For this, we can focus on specific operation points, belonging to the susceptibility zones, (points with $\langle \mathrm{SEY} \rangle > 1$ in Fig. 4.4), and study in more depth how the phenomenon evolves. Let us consider two operation points, A and B in the chart of Fig. 4.4, corresponding to a low and a high multipacting rate, respectively.

Starting with the case A, Fig. 4.5 depicts the evolution of the charge density of the moving electron sheet and of the surface charge on the dielectric. The plot shows that the phenomenon evolves in three different stages. During the first stage (multipactor onset), both electron population and surface charge increase until a saturation is reached. During the saturation state, i.e. between the 130th and 180th RF period, the electron population remains almost

---

[‡] In this example we use the same SEY properties for both metal and dielectric surface in order to focus on the effect of the surface charge on the dielectric.

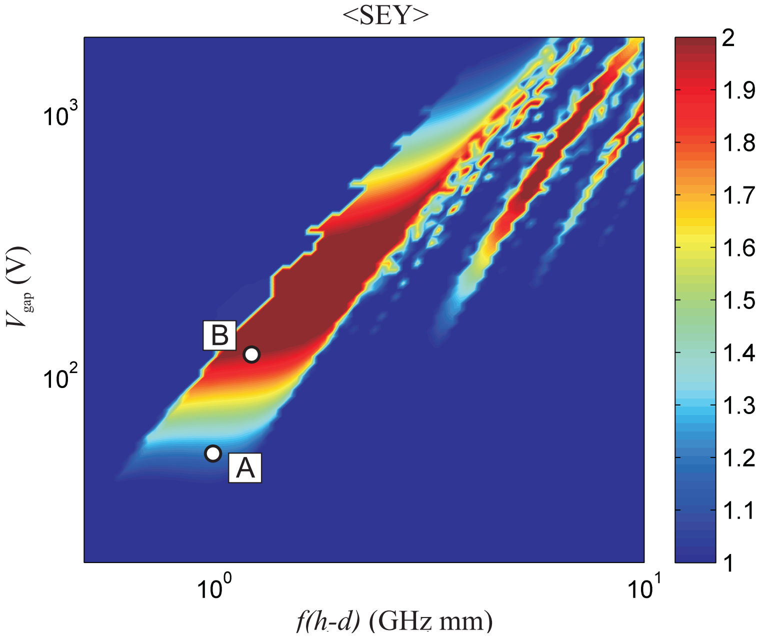

Figure 4.4.: Short term evolution: Mulipactor chart for parallel plates loaded by a single dielectric slab. The color intensity represents the geometric mean SEY value at impacts, $\langle \text{SEY} \rangle$, for the first phase of the multipactor evolution (multipactor onset). The following parameters have been considered: $h = 1.1$mm, $d = 0.1$mm and $\epsilon_r = 3$. The SEY properties of silver, as given in Table 3.2, have been assumed for both metal and dielectric surfaces. Long-term multipaction will be studied later for the points A and B. A: $V = 45$ V, $f = 1$ GHz, B: $V = 110$ V, $f = 1.2$ GHz

constant. A similar trend is also observed for the surface charge on the dielectric. However, this state breaks after a few periods. At the end, the electron cloud disappears while the dielectric surface remains charged, similarly to what has been reported in literature (see Fig. 4.3). In order to figure out the mechanisms that result in this behavior let us study the evolution of the phenomenon stage by stage.

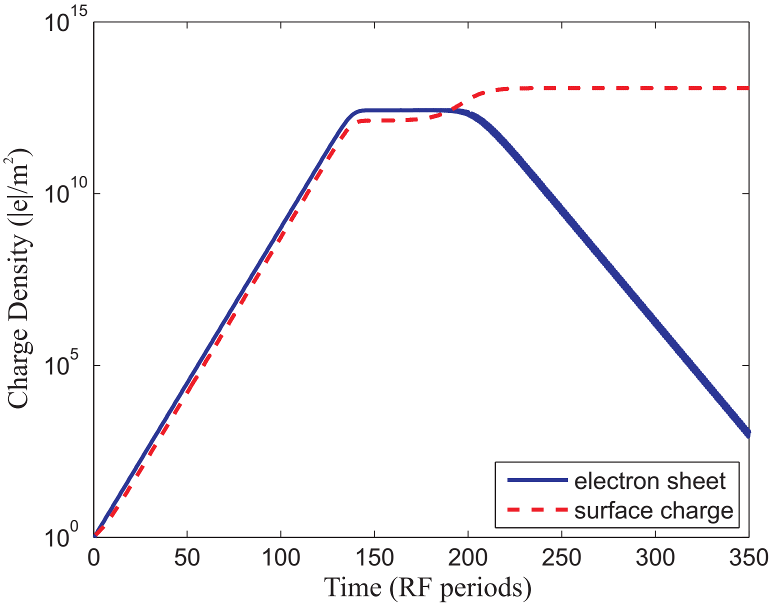

Figure 4.5.: Time evolution of the charge density (amplitude) of the electron sheet, $|\sigma_{\rm el}|$ and of the surface charge on the dielectric, $|\sigma_{\rm diel}|$. The results correspond to the operation point A in Fig. 4.4. Note, that the vertical axis represents the amplitude of the charge densities, given in $|e|/{\rm m}^2$, where e is the charge of a single electron. For the depicted case, the surface charge on the dielectric is positive.

During the growth of the electron population, the electron dynamics are dominated by the RF field, whereas the effects of the induced charge and the surface charge are negligible. This can be confirmed by the results illustrated in Fig. 4.6. In this plot, the evolution of the electron population obtained by taking into account the saturation mechanisms (blue solid line) is compared with the corresponding evolution obtained by considering only the applied RF field (marked dashed line). As can be observed, the two lines are in perfect agreement during the first phase of the phenomenon, i.e. before saturation is achieved. From the same plot, we can also see that the dielectric is continuously charged during the multipactor onset, in parallel to the growth of the electron population. Although, the charge density of the dielectric surface is always lower than the one of the moving electron sheet [§], it should be noted that both densities are of similar order of magnitude. Indeed, the charge on the dielectric increases with the same rate as the charge of the moving electron sheet, as illustrated in the subplot of Fig. 4.6 (parallel lines in logarithmic scale). Hence, the ratio between the two charge

---

[§] This is expected since the population of the electron sheet increases after each impact (either on the metal plate or on the dielectric slab), whereas the charge on the dielectric increases only after impacts on the slab.

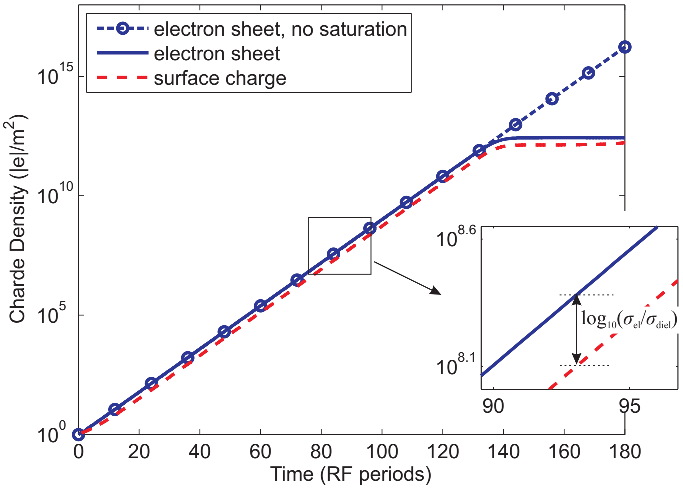

Figure 4.6.: Evolution of the charge density (amplitude) of the electron sheet and of the surface charge on the dielectric during the multipactor onset for the same case as in Fig. 4.5. Results obtained by neglecting the saturation mechanisms are also included for comparison reasons. The ration between the charge density of the electron sheet and the density of the surface charge on the dielectric is equal to $|\sigma_{\text{diel}}/\sigma_{\text{el}}| = 0.528$.

densities, $|\sigma_{\text{diel}}/\sigma_{\text{el}}|$, remains almost constant during the multipactor onset. For the examined case A this ratio is approximately equal to $|\sigma_{\text{diel}}/\sigma_{\text{el}}| = 0.528$, meaning that the dielectric acquires a significant net charge, comparable to the charge of the electron sheet. Therefore, both the induced charge and the surface charge are expected to affect the saturation stage.

A better view of how intense is the effect of each saturation mechanism can be obtained by comparing the corresponding field components, $\mathbf{E}_{\text{induced}}$ and $\mathbf{E}_{\text{diel}}$. Figure 4.7 depicts the profile of the electric field components with respect to the position of the moving electron sheet. As can be seen, although the dielectric surface and the electron sheet have comparable charge densities ($|\sigma_{\text{diel}}/\sigma_{\text{el}}| \approx 0.5$), the corresponding field components differ notably. In particular, the self-field, $\mathbf{E}_{\text{induced}}$, is much higher than the field due to the surface charge on the dielectric, $\mathbf{E}_{\text{diel}}$, for a wide range of the electron sheet positions. What gives rise to the importance of the induced charge is the fact that the self-field governs the total saturation field, $\mathbf{E}_{\text{sat}}$, especially when the moving sheet is close to the boundaries. At these areas, i.e. close to the boundaries, the saturation field is supposed to have its major influence on the electron dynamics since it obtains its maximum amplitude. To show the significance of the induced charge we have simulated the evolution of the electron population following two different approaches: first, taking into account only the induced charge and, second, considering only the surface charge on the dielectric. As shown in Fig. 4.8, the saturation stage, as it is predicted by the full model, can be achieved by considering only the self-field. On the other hand, the effect of the surface charge, omitting the self-field, becomes evident for a charge density higher than the one corresponding to the saturation level. Therefore, the mechanism that is responsible for the transition from the onset to the saturation is the induced charge.

Up to now, we have analyzed the evolution of the phenomenon till the moment that the

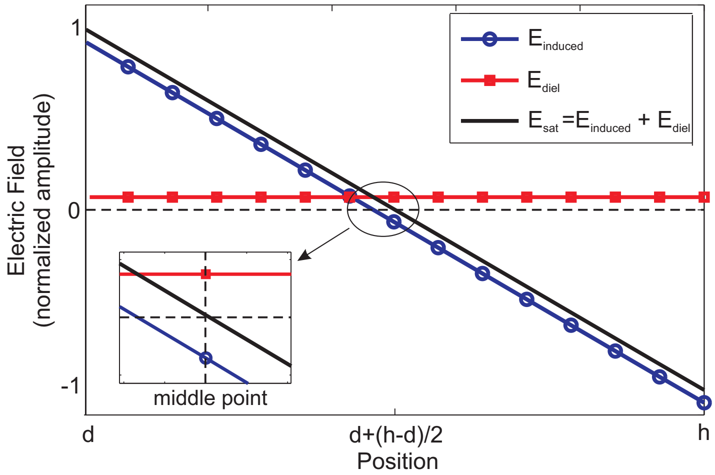

Figure 4.7.: Electric field due to the saturation mechanisms (induced charge and surface charge) as a function of the position of the moving electron sheet, z'. The same configuration as in Fig. 4.4 is considered. The ratio between the density of the surface charge and the density of the electron sheet corresponds to the one of Fig. 4.6, i.e. $\sigma_{\text{diel}}/\sigma_{\text{el}} = -0.528$ ($\sigma_{\text{el}} < 0$ and $\sigma_{\text{diel}} > 0$).

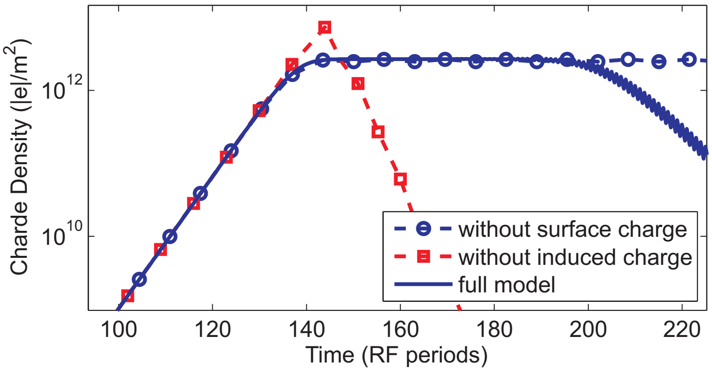

Figure 4.8.: Evolution of the electron population for the examined case A (see Fig. 4.4). Three different models have been considered regarding the saturation mechanisms. Dashed line marked with circles: only the induced charge is taken into account. Dashed line marked with rectangles: only the surface charge on the dielectric is taken into account. Solid line: Full model taking into account both the induced charge and the surface charge both the induced charge and the surface charge (same as in Fig. 4.5).

saturation stage starts to take place. Next, we focus our analysis on the saturation stage in order to study how the mechanisms of the induced charge and of the surface charge on the dielectric affect the long-term evolution of the phenomenon. Looking again at the plot of Fig. 4.5 we can notice that during the saturation phase the surface charge on the dielectric remains almost unchangeable. This implies that the electron sheet hits the dielectric slab with an energy equal to the first crossover point, so that the SEY is equal to unity. Indeed, as Figs. 4.9 and 4.10 illustrate, during the saturation phase the electrons follow a resonant motion hitting both the metallic and dielectric surface with an impact energy that yields an SEY close to unity.

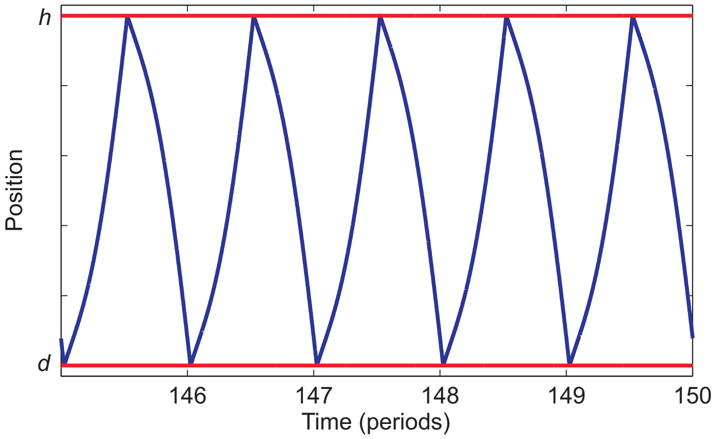

Figure 4.9.: Motion of the electron sheet during the saturation stage. The case A of Fig. 4.4 is considered.

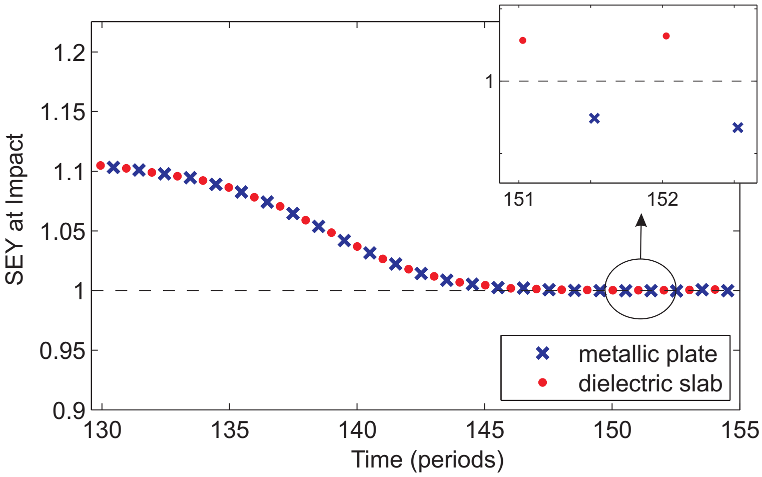

Figure 4.10.: SEY at impact events during the transition from the multipactor onset to the saturation. The case A of Fig. 4.4 is considered.

As Fig. 4.5 depicts, the saturation phase does not result in a permanent state but it breaks after some RF periods. The reason is that the above described saturation manner constitutes an unstable process. Let us try to qualitatively explain why saturation in the examined case is not stable. Assume, for instance, that the electrons hit the dielectric with a slightly higher impact energy than the one with which they hit the metal plate. This is, in fact, what happens in the examined case, as can be seen in the subplot of Fig. 4.10. Then, the DC-like field due to the positive surface charge on the dielectric will slightly increase (since SEY > 1 at impact on the dielectric yields an increase at the density of the surface charge). Consequently, the moving electron sheet will feel a net force which is attractive towards the dielectric slab. As a result, the sheet will collide with the dielectric slab with even a higher impact energy. This process results in a continuously increasing surface charge on the dielectric that attracts more and more the electron sheet. On the other hand, an absorption process takes place on the metal plate since the DC-like electric field decreases the velocity of electrons when they move towards the metal plate. At the end, the evolution stabilizes at a state where the absorption rate on the metal plate overcomes the secondary emission rate on the dielectric. As a consequence, an overall absorption process takes place resulting in the disappearance of the free electrons. A schematic representation of the unstable saturation process is given in Fig. 4.11. In a similar way, it can be demonstrated that the saturation process is also unstable if the impact energy on the dielectric is slightly lower than the one on the metal plate. In such a case, a negative surface charge is developed on the dielectric slab.

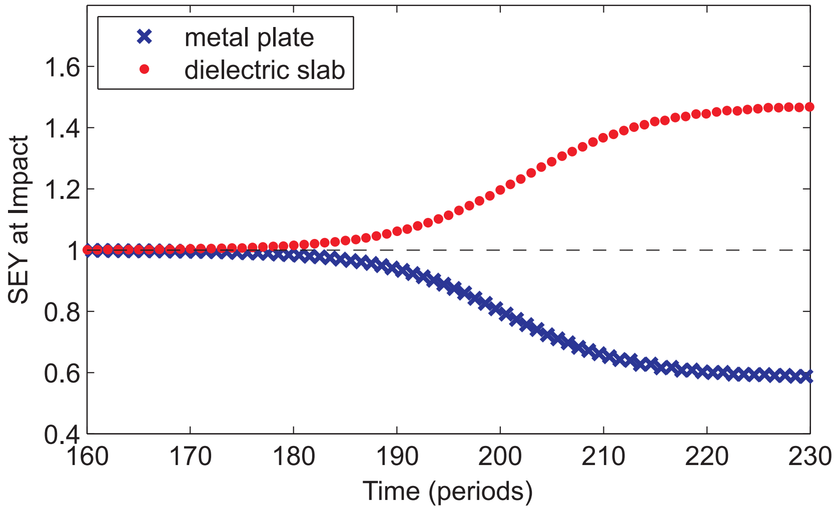

Figure 4.11.: SEY at impact events during the transition from the saturation stage to the final extinguishing stage.

Summarizing our analysis for the case A, the phenomenon starts with an exponential growth of the electron population. During this phase, (multipactor onset), the dominant mechanism is the external RF field that makes electrons hit the surfaces with sufficient impact energy to provoke the emission of secondary electrons. In parallel, a surface charge is developed on the dielectric, which increases with a rate similar to the one of the electron population. As the electron population reaches high levels, a saturation stage is achieved. As have been shown, the mechanism that is responsible for the transition from the multipactor onset to the saturation is due to the charge induced on the plates by the moving electron sheet. However, the saturation stage is temporary since the presence of the surface charge on the dielectric results in an unstable saturation process. Soon, the phenomenon passes to the final stage that is the extinction of the electron population. On the other hand, the dielectric surface remains charged.

Next, we study the long-term evolution of the phenomenon for the case B in the chart of Fig. 4.4. Comparing to the case A, here, the applied gap voltage is notably higher ($V_\mathrm{B} = 110\mathrm{V}$ instead of $V_\mathrm{A} = 45\mathrm{V}$ in case A). As it will be shown later, this results in a completely different long-term multipactor evolution.

Figure 4.12 illustrates the evolution of the charge density of the moving electron sheet and of the surface charge on the dielectric. As can be seen, the phenomenon evolves in two distinguishable stages. First, both the electron population and the surface charge on the dielectric grow exponentially until a saturation is reached. Then, during the saturation, the corresponding charge densities of the electron sheet and the surface charge oscillate around a mean value that remains fairly constant. Opposed to the case A, here, the long-term evolution of the phenomenon is defined by the saturation stage. As a consequence, an electron cloud sustains between the dielectric and the upper metal plate.

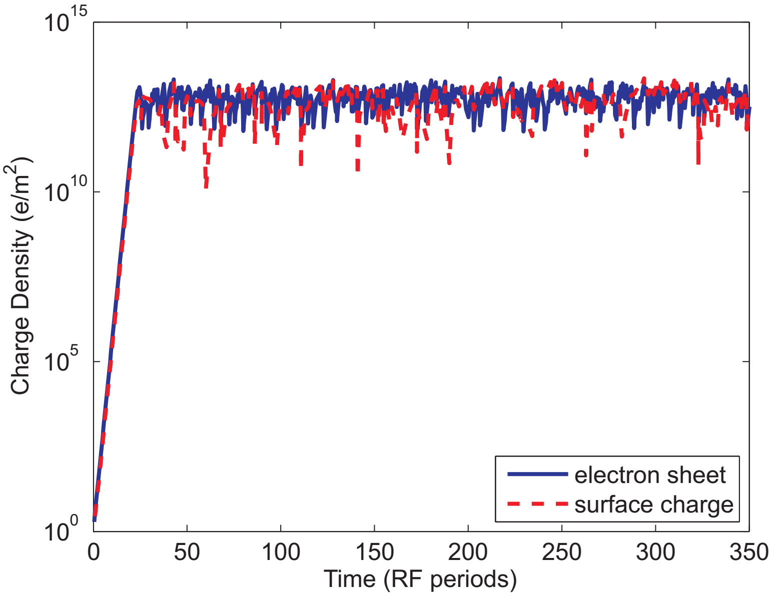

Figure 4.12.: Time evolution of the charge density (amplitude) of the electron sheet, $|\sigma_\mathrm{el}|$ and of the surface charge on the dielectric, $|\sigma_\mathrm{diel}|$. The results correspond to the operation point B in Fig. 4.4. Note, that the vertical axis represents the amplitude of the charge densities, given in $|e|/\mathrm{m}^2$, where e is the charge of a single electron.

Let us try to explain the above described behavior regarding the long-term evolution. What attracts most of our attention in the plot of Fig. 4.12 is the intense oscillatory behavior of the electron population (or equivalently, of the charge density). This trend implies that there is a fast alteration between subsequent secondary emission and absorption events. A first insight on this behavior can be obtained by plotting the motion of the electron sheet. As Fig. 4.13 reveals, there is a 'stuck' mechanism that makes the electron sheet come back to the surface of emission very fast. This mechanism is expected to come from a strong saturation field that forces electron towards the wall of emission. As mentioned before, the applied RF excitation is remarkably higher in the case B than in the case A. Therefore, a strong saturation field needs to oppose the RF electric field. Indeed, as Fig. 4.14 illustrates, the effect of the induced charge is remarkably intense so that the self-field partially overcomes the peak-value of the applied RF field. Similarly to the case A, the self-field is clearly the dominant component in the total saturation field. Therefore, the mechanism that determined the saturation level is again the induced charge.

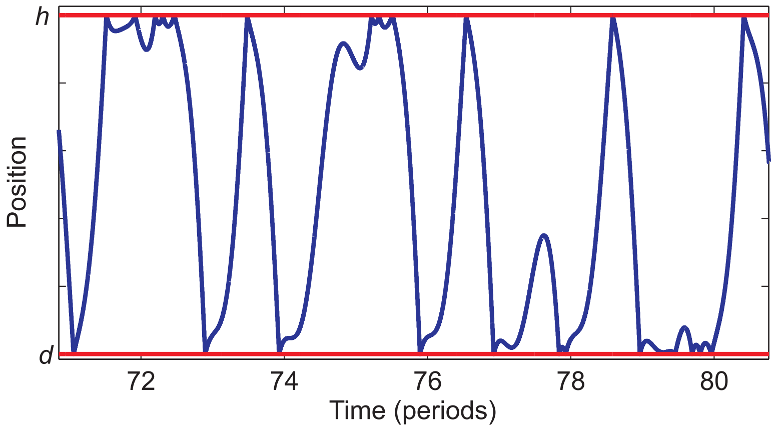

Figure 4.13.: Motion of electron sheet during the saturation stage. The case B of Fig. 4.4 is considered.

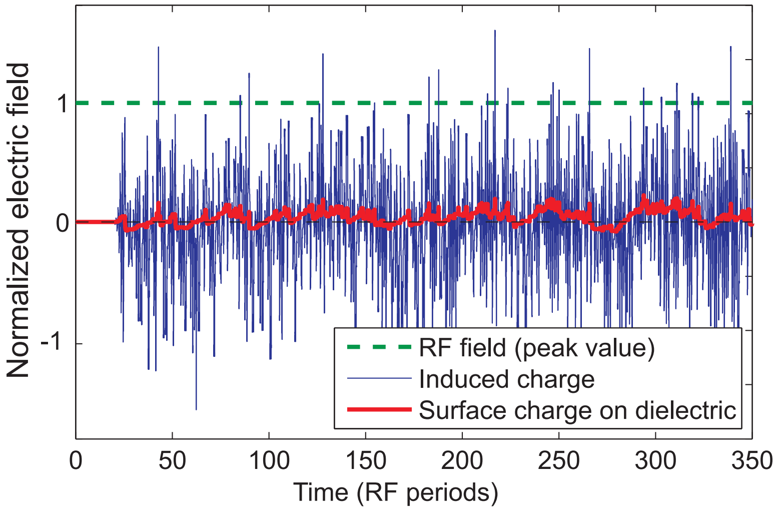

Figure 4.14.: Electric field (normalized to the peak value of the RF field) as a function of time.

Taking into account the previously mentioned statements, the long-term evolution in the case B can be described as following. During the multipactor onset, the electron dynamics are dominated by the applied RF field. As in the classical multipactor onset, the electrons follow a resonant motion, hitting the walls with sufficient impact energy so that they provoke the emission of secondary electrons. As a result, an exponential increase of the electron population and of the surface charge on the dielectric occurs. Due to the strong electric field, a proportionally strong self-field is needed so that the saturation stage is achieved. After the saturation is reached, the resonant motion that was taking place during the multipactor onset breaks. In particular, the electrons are stuck on the surface of emission due to the strong field coming from their image charge. After few impacts on the same plate, some electrons are absorbed since they come back to the surface of emission very fast without gaining enough energy. Then, since the electron population decreases, the saturation field decreases, too, and the electrons manage to transverse the gap. Due to the 'stuck' mechanism, the surface charge on the dielectric remains almost constant during the saturation stage, following a similar behaviour as the electron population. However, as it has been shown, its effect on the evolution of the electron population is minor comparing to the effect of the induced charge.

Summarizing our analysis, we can conclude that the essential difference between the cases A and B is that in the case B the RF field is strong enough to maintain the electron population.

4.3.3. Summary

In this Section, long-term multipactor evolution in a parallel plates waveguide partially loaded by a dielectric slab has been investigated. In order to consider the saturation mechanisms, a new model able to take into account the induced charge in the configuration under study has been developed. Moreover, the effect of the dielectric has also been taken into account by considering a surface charge developed on the dielectric-vaccum interface. For the first time, both the effects of the surface charge on the dielectric and of the induced charge have been considered for the examined configuration.

By applying the developed model, the analysis revealed original results regarding the long-term evolution of the phenomenon. Through numerical examples, it has been reported that two different mechanisms may occur resulting in remarkable different behaviors regarding the evolution of the electron population. These mechanisms can be briefly described as following:

- **self-extinguishing mechanism:** This mechanism occurs when the applied gap voltage is relatively small, i.e. the operation point is close to the lower multipactor threshold. When this mechanism takes place the electron population reaches a saturation stage, which is, however, unstable. Then, after few periods the mechanism results in the disappearance of the electron population. On the other hand the dielectric surface remains charged. This mechanism is characterized by two-sided multipaction, meaning that the electrons return back to the same wall after a integer number of periods.

- **self-sustaining mechanism:** This mechanism typically occurs for relatively high gap voltages, i.e. when the multipacting rate during the multipactor onset is relatively high. Contrary to the self-extinguished mechanism, the electron population is self-sustained close to a saturation level. The underlined process behind this manner is a

> ‘stuck’ mechanism, implying that during the saturation stage, the electrons are stuck on the plate of emission due to the strong force coming from their induced charge. In this case the effect of the dielectric surface charge on the long-term evolution of the electron population is almost negligible. However, as in the case of the self-extinguishing mechanism the dielectric surface remains charged.

A representative overview regarding the multipactor zones in which of the above mechanisms take place is provided in Fig. 4.15.

Through the analysis performed in this chapter, a qualitative overview regarding the long-term multipactor evolution in partially loaded waveguides has been achieved. For the first time, the existence of a saturation stage has been reported for the considered configuration. Despite the simplifications of the developed model, the analysis performed can constitute the basis for an extensive 3D model that takes into account the stochastic behavior of the secondary emission process as well as the space charge effects, as discussed in the next Section.

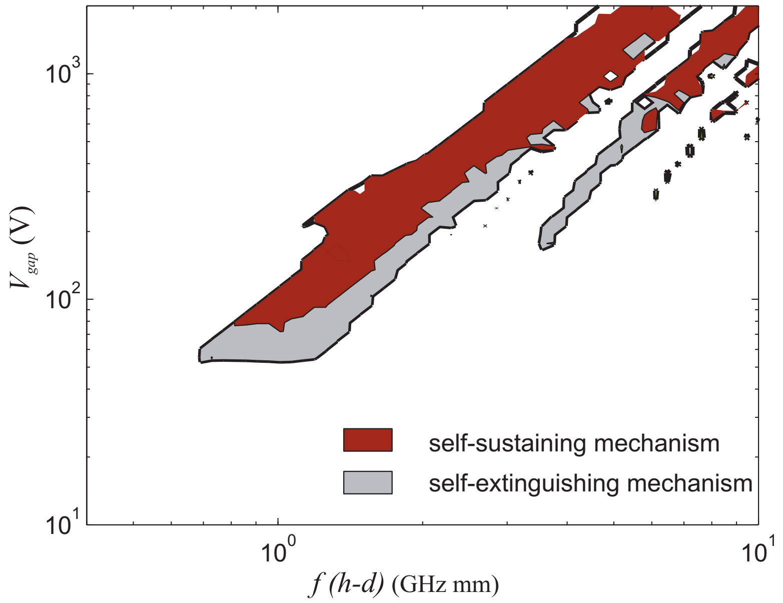

Figure 4.15.: Long term evolution: Multipactor chart showing in which area each of the two long-term evolution mechanism occurs. The same parameters as in the Fig. 4.4 have been considered.

4.4. 3D Approach

The analysis presented in the previous section provides a first, qualitative overview of the long-term multipactor evolution in partially loaded waveguides. However, the corresponding 1D model implies some limitations, mainly related with the representation of the distribution of the electrons. As mentioned before, the single electron model assumes that the electrons are all travelling with the same speed composing a thin electron sheet. As a consequence, the space charge effect is approached by considering only the induced charge, omitting, thus, the direct Coulomb interactions between the moving electrons (see the introduction of 4.3). Due to its repelling nature, the Coulomb force makes the electrons spread so that they compose a thick electron sheet. The spread of electrons is even more reinforced by the randomness of the initial velocity of the emitted electrons. This trend of the electrons to spread has been highlighted by Riyopoulos et al. who have studied multipactor steady-state in the fundamental case of empty parallel plates [59]. As it has been reported in their work, the electrons compose an electron cloud rather than a thin electron sheet during the saturation phase. It becomes clear that the single electron model that assumes a deterministic emission velocity and neglects the Coulomb interactions is limited to a poor representation of the electron distribution, especially with respect to the long-term evolution of the discharge.

The spread on the electron positions and velocities could notably affect the long-term evolution of the discharge. The importance of the representation of the electron distribution is raised in the case of dielectric walls since a spread of electrons could potentially affect the evolution of the surface charge on the dielectric surfaces. Consider, for instance, the case A as it has been described in Section 4.3.2. In that example, the electron sheet was following a resonant motion even after the saturation had been reached (see Fig. 4.9). Due to this resonance, the dielectric surface was continuously charged positively after every impact of the electron sheet on the dielectric slab. However, in realistic conditions, the electrons are expected to follow a random-like motion due to the spread of emission velocities and due to the mutual Coulomb interactions. Hence, it is most probable that the dielectric material is charged heterogeneously, sometimes positively and sometimes negatively in case of secondary electron emission or electron absorption, respectively.

The above mentioned statements motivate us to extend the 1D analysis by developing a more advanced model able to consider the spread of the electrons. For this purpose, a multiple particle 3D model is, following, presented which takes into account the Coulomb interactions as well as the stochastic behavior of the secondary emission process in addition to the effects of the induced charge and the surface charge on the dielectric.

4.4.1. Modeling

Modeling the statistics of the secondary emission process as well as the mutual interactions between electrons constitutes a particularly challenging problem. First, in order to take the statistics of the secondary emission into account the electrons have to be modeled individually. This implies a complexity proportional to the number of the moving electrons, $O(N_{\mathrm{el}})$, where N_{el} is the number of the electrons. The complexity increases much more by including the Coulomb interactions between electrons. Since every electron interacts with all the others, the mutual interactions between them entail a N-body problem with a corresponding complexity of $O\left(N_{\mathrm{el}}^2\right)$. Taking into account that the electron population grows exponentially in case the discharge occurs, the number of electrons reaches soon huge levels and, as a result, the complexity of the problem becomes prohibitive. This makes indispensable the need for applying approximation techniques in order to manipulate the huge complexity due to the space charge effect.

Electron Distribution

A technique for decreasing the complexity of multipactor analysis, that has been widely used in the literature, is the macroparticle approach [52, 71, 82–86]. The underlined concept behind this technique is that a single particle (macroparticle) can represent a group of electrons which are assumed to follow a similar motion. The single electron approach, that has been previously followed for the 1D modeling, can be considered as a particular case of the macroparticle technique since a single particle represents the whole population of electrons assuming that they compose a thin electron sheet. Contrary to the 1D case, in 3D modeling multiple particles need to be considered in order to take into account the stochastic behaviour of the secondary emission, the 3D motion of the electrons as well as the mutual interaction between them. Differently to the 1D macroparticle that represents a plane distribution of electrons, a macroparticle in 3D represents a group of electrons distributed in a spherical area, close to a central point. This point is the position of the macroparticle. Then, the electrons, represented by the corresponding macroparticle, are assumed to move all together and, consequently, their motion is represented by the motion of the macroparticle. Each macroparticle is characterized by a weight function that represents the total number of electrons corresponding to the macroparticle. Let $N_{\mathrm{el,i}}$ be this number corresponding to the i^{th} macroparticle. Then, the effective charge and mass of the macroparticle is equal to the total charge and mass of the corresponding electrons, that is $q_{\mathrm{macro,i}} = N_{\mathrm{el,i}}e$ and $m_{\mathrm{macro,i}} = N_{\mathrm{el,i}}m$, where e and m is the charge and the mass of a single electron, respectively. After an impact event on the device walls, the weight function of the macroparticle is updated as follows

$$N'_{\mathrm{el,i}} = \delta_{\mathrm{imp}} N_{\mathrm{el,i}}, \tag{4.20}$$

where δ_{imp} is the SEY value of the corresponding impact event.

The macroparticle approach can significantly reduce the complexity of the multipactor analysis. By fixing the number of the considered macroparticles, one can control the complexity of the problem independently of the increase of the electron population. Although the macroparticle approach implies assumptions regarding the representation of the electron distribution it can be efficiently used in order to take the statistics of the secondary emission into account. Considering a high number of macroparticles, a sufficient number of independent impact events can be modeled, providing, thus, a proper representation of the stochastic behavior of the secondary emission process. The more macroparticles are considered the better is the representation of the secondary emission statistics, since more independent events can be taken into account.

Focusing only on the 1st phase of the phenomenon, i.e. the multipactor onset, the macroparticle approach can provide a precise estimation of the electron evolution. The efficiency of the macroparticle approach weakens when the saturation stage is studied. As the discharge evolves and approaches saturation, the space charge effect becomes significant and the electrons tend to repel between them due to the mutual Coulomb force. An effective point charge cannot precisely represent a huge number of electrons and, therefore, the efficiency of the macroparticle approach is limited. To handle this weakness, an adaptive manipulation of the macroparticle size ¶ has been applied in order to prevent a huge increase of the macroparticle size and, consequently, a bad representation of the electron distribution.

Space Charge Effect

As mentioned above, the complexity required for the evaluation of the space charge effect becomes huge as the electron population increases since it is in the order of power to 2, i.e. $O\left(N_{\text{el}}^2\right)$. Even by applying the macroparticle approach the complexity remains high enough, that is $O\left(N_{\text{macro}}^2\right)$, where N_{macro} is the number of the considered macroparticles. Many works in the literature have applied the Particle-in-Cell (PIC) method in order to evaluate the space charge effect [59, 87–89]. According to this method, the charge of the particles is projected on a spatial grid. Then, the Maxwell equations can be solved by applying common finite difference schemes. In this way, the electric field, coming from both the RF excitation and the charged particles, is evaluated with a complexity similar to the one of the finite difference solver that is typically significantly lower than $O\left(N_{\text{macro}}^2\right)$. However, the PIC method is known to be inaccurate regarding the near interactions, including both the repelling force when two particles are approaching themselves as well as the interaction of the charged particles with their induced charge (image charge) when they approach a boundary. Since the near interactions are expected to affect most the particle dynamics (strong force between close particles), in this work the space charge effect is modeled by evaluating directly all the particle-to-particle interactions, through the Coulomb force. In order to compensate the enormous computational effort required for the calculation of all N_{macro} by N_{macro} interactions (including the interactions of the particles with the induced charge) efficient parallelization programming techniques have been applied.

Surface Charge on the Dielectric

When an electron collides with the dielectric surface the surface is locally charged by a negative or positive amount of charge, in case an absorption or a secondary emission occurs, respectively. Since the dielectric is supposed to be a perfect isolator, the additional charge on the dielectric surface remains very close to the impact point. An excessively precise modeling of the surface charge implies that an additional charge (approximately a point charge) has to be considered after every impact event at the collision point. Let us call them "surface point charges". Such a model would result in a dramatic increase of the complexity of the problem. Since every electron may impinge several times at any point of the dielectric surface a huge number of surface point charges would need to be considered.

[¶] In this thesis, the macroparticle size is referred to the number of the electrons represented by the macroparticle, i.e. the value of the weight function

In order to tackle the above described difficulty an alternative approach is proposed. The dielectric is discretized into surface patches, as Fig. 4.16 illustrates. The surface charge density of a single patch is assumed constant simplifying notably the calculation of the electric field due to the whole surface charge on the dielectric. Despite its simplicity, the model can provide a fair representation of the surface charge distribution. Taking many patches into account, the proposed model is able to represent a potential inhomogeneity of the surface charge on the dielectric. On the other hand, the complexity required for the calculation of the corresponding electric field can be significantly lower comparing to the one that would be needed if surface point charges were considered. Setting a certain number of patches, the complexity introduced by including the effect of the surface charge on the dielectric can be controlled.

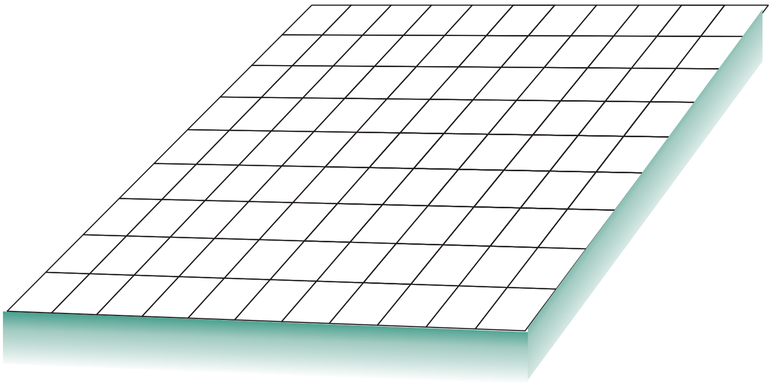

Figure 4.16.: Discretization of the dielectric surface into patches. The surface charge density on a single patch is considered constant. After every impact event, the total charge of the corresponding patch changes according to the charge added at the collision point.

Lateral Limits

In the 1D approach the two metallic plates as well as the dielectric slab were considered infinite in terms of the lateral directions x, y. In order to tackle this non-realistic artifact, we have developed the corresponding 1D by considering the charge density of the electron sheet, which is finite, instead of the absolute number of electrons. Here, in the 3D analysis, we have to consider separate particles instead of charge densities in order to model the spread of electrons. If we assumed infinite plates, as in the 1D case, no saturation would be reached. Indeed, due to the repelling nature of the mutual force between the electrons the electron cloud would infinitely augment towards the lateral directions. For this reason, the boundaries are truncated towards the lateral directions x and y, as illustrated by the example of Fig. 4.17. Therefore, the electrons that exceed the lateral limits are considered lost. Let us call this approximation as "lateral loss approach".

This approach can be considered as a fair approximation for multipactor studies in several realistic structures. For instance, in a rectangular waveguide, assuming the fundamental TE_{10} mode, the electric field tends to zero as approaching the lateral walls. As a consequence, the movings electrons located close to the lateral walls are most possible to be absorbed on the boundaries since the do not gain sufficient kinetic energy in order to provoke the emission of secondary electrons. In addition to rectangular waveguides, waveguide irises constitute another example where the lateral loss approach could be fairly applied. In such a case, when moving electrons exceed the lateral gap of the iris they normally pass from a high electric field to a low electric field area. Therefore, these electrons tend to be lost and only a small portion of them could contribute in multipacting process [90].

4.4.2. Formulation

The 3D solver starts by placing a certain number of macroparticles between the plates, randomly distributed (in terms of position and velocity). Then, each macroparticle moves according to a 3D tracker which is based on the 4th order Runge-Kutta differential scheme. Comparing to the corresponding 1D tracker, the 3D one considers all the 3D field components. Since both the induced charge and the Coulomb field are taken into account, additionally to the applied RF field and the field coming from the surface charge on the dielectric, the total electric field considered by the tracker is given as follows:

$$\mathbf{E}_{\text{total}} = \mathbf{E}_{\text{rf}} + \mathbf{E}_{\text{diel}} + \mathbf{E}_{\text{induced}} + \mathbf{E}_{\text{coulomb}}, \tag{4.21}$$

where $\mathbf{E}_{\text{rf}}$ is the applied RF field, $\mathbf{E}_{\text{diel}}$ the field due to the surface charge on the dielectric, $\mathbf{E}_{\text{induced}}$ the field due to the charges induced on the boundaries and $\mathbf{E}_{\text{coulomb}}$ the field coming from the direct mutual interactions between the electrons.

Let us, now, discuss how each of the electric field components of Eq. (4.21) can be evaluated. Neglecting the fringing fields close to the plates edges, the RF field can be evaluated as in the 1D case, that is assuming infinite parallel plates. Under this assumption, that fairly holds when the plates width is much bigger than the distance between the plates, the RF field component is given by the following expression,

$$\mathbf{E}_{\text{rf}} = \frac{V_{\text{gap}}}{h-d} \sin(\omega t)\, \hat{\mathbf{z}}, \quad d < z < h, \tag{4.22}$$

where d is the thickness of the dielectric slab and V_{gap} is given by Eq. (4.15), as in the 1D case.

Regarding the remaining field components, the most difficult part lies on the evaluation of the field due the induced charge which entails the following peculiarity: the evaluation of the electric field on a source position, that is the field that a point charge results on itself through the induced charge. Searching for an efficient Green Function (GF) method that fits to this feature, the image series approach attracts most our interest since it provides a straightforward separation of the singular source term and the remaining, regular part of the GF. Moreover, image series provide an efficient calculation of the close-to-the-source field, which is of the most importance regarding the evaluation of the space charge effect. For this purpose, a novel image method for the GF evaluation in multilayered shielded media has been developed, as will be presented in Chapter 5. The electrostatic GF can be expressed in an image series as follows:

$$4\pi\varepsilon_0 \mathbf{G}_{\mathrm{E}}\left(\mathbf{r},\mathbf{r}'\right) = \sum_{n=-\infty}^{\infty} \frac{w_n d\mathbf{r}_n}{\left|\mathbf{r}-\mathbf{r}'_{1,n}\right|^3} - \frac{w_n d\mathbf{r}_n}{\left|\mathbf{r}-\mathbf{r}'_{2,n}\right|^3}, \tag{4.23}$$

where $\mathbf{r} = \rho\hat{\rho} + z\hat{\mathbf{z}}$ and $\mathbf{r}' = \rho_0\hat{\rho} + z_0\hat{\mathbf{z}}$ are the positions of the observation and the source point, respectively, $\mathbf{r}'_{1,n}$ and $\mathbf{r}'_{2,n}$ the positions of the images, w_n the charge of the corresponding images and $d\mathbf{r}_n = \mathbf{r} - \mathbf{r}'_n$ is the distance (vector) between the source point and the corresponding images. The position and the charge of the images are evaluated in Chapter 5 and are summarized in Table 5.1.

Once the electric field GF is known, both the Coulomb field and the field coming from the induced charge can be evaluated. In particular, the zero-*th* term of the first sum in Eq. (4.23) corresponds to the Coulomb field effect of a point charge to another point charge, while all the remaining infinite terms provide the corresponding field due to the induced charge. Since the space charge effect is typically intense when the particles are close, a few terms of the infinite sum of (4.23) provide a sufficient accuracy. For the remaining simulations, the first 8 image charges have been used.

Having the knowledge of the image series representation of the GF, it is straightforward to evaluate the field coming from the surface charge on the dielectric, $\mathbf{E}_{\mathrm{diel}}$. As has been mentioned in Section 4.4.1, the dielectric surface is discretized into patches with constant charge density. Then, the field coming from a single patch is the free-space contribution of the patch itself in addition to the contribution of its image patches. The position and the density of the image patches can be straightforwardly found by the corresponding image series representation of the GF.

4.4.3. Example of Analysis

In this section we apply the above described 3D model for the analysis of the long-term multipactor evolution in parallel-plate waveguides partially loaded by dielectric. As an example, we consider the same configuration as in the 1D analysis, that is a parallel-plate waveguide with a distance between the plates equal to $h = 1.1$mm loaded by a dielectric slab of $d = 0.1$mm and $\varepsilon_{\mathrm{r}} = 3$. The secondary emission properties of silver are considered for both the metallic plate and the dielectric surface. The configuration under study is depicted in Fig. 4.17. Note, that differently to the 1D analysis, here, the plates are laterally truncated (in x and y directions) so that an infinite increase of electron population is prevented.

Since the configuration is the same as in the example of the 1D analysis (in terms of dimensions and SEY properties) multipactor is expected to occur inside the susceptibility zones as they are shown in the multipactor chart of Fig. 4.4. Let us study the case A, as depicted in the chart of Fig. 4.4, which presents particular interest since it is close to the lower multipactor threshold. For this case, the applied RF voltage and frequency are equal to $V = 45$ V and $f = 1$ GHz, respectively.

Figure 4.18 shows the evolution of the electron population and of the accumulated surface charge on the dielectric. Comparing to the results obtained by the 1D analysis (see Fig. 4.5), one can observe that the same qualitative behavior is obtained by applying the 3D

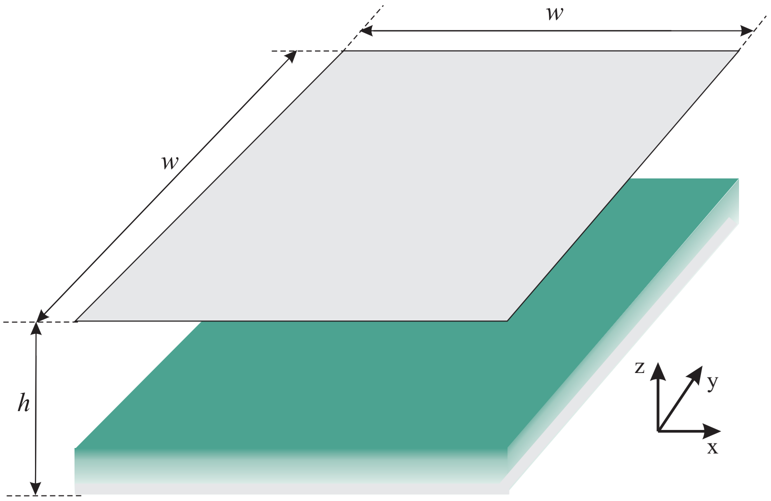

Figure 4.17.: Configuration under study in the 3D analysis. The following dimensions are considered: $h = 1.1\text{mm}$, $d = 0.1\text{mm}$, $w = 5\text{mm}$. The dielectric constant of the slab is equal to $\varepsilon_\mathrm{r} = 3$ The SEY properties of silver are considered for both metallic and dielectric surfaces (see Table 3.2). The moving electrons that exceed the lateral limits are considered as lost.

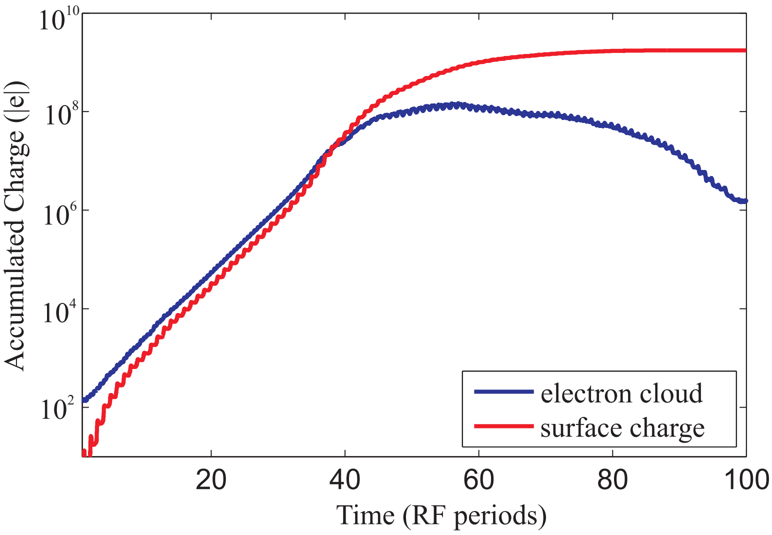

Figure 4.18.: Time evolution of the electron population (electron cloud) and of the accumulated charge on the dielectric (given in $|e|$, where e is the charge of a single electron). The results correspond to the operation point A in Fig. 4.4. The following simulation parameters have been considered: $N_\mathrm{macro} = 20000$, $\Delta x = 0.1$ mm and $\Delta y = 0.1$ mm, where N_macro is the number of the macroparticles, Δx and Δy the dimensions of each surface patch.

model. In particular, the phenomenon evolves in three different stages. First, the multipactor onset takes place during which both electron population and surface charge increase. As the phenomenon evolves, the electron population reaches a maximum level, around the 50th RF period. Then, a saturation-like phase is achieved during which the electron population remains almost constant, however, slightly decreasing. On the other hand, during this phase, the surface charge on the dielectric is continuously increasing, but with a lower rate comparing to the one during the multipactor onset. This behavior has been also remarked in the 1D analysis. The saturation-like phase breaks after a few periods (until the 75th RF period). At the end, the electron cloud disappears while the dielectric surface remains positively charged.

A better overview of multipactor evolution can be obtained through the spatial distribution of the moving electrons as well as the distribution of the surface charge on the dielectric. Figures 4.19 and 4.20 depict the electron cloud distribution and the surface charge density on the dielectric, respectively, at the end of the simulation (100th RF period). Let us start our discussion with the surface charge distribution. As can be observed in Fig. 4.20 the dielectric surface has been charged fairly homogeneously with a positive charge. The slight discrepancies observed come from the stochastic nature of the secondary emission process. Due to the positive surface charge, the electrons are attracted towards the dielectric surface. This can be, clearly, seen in the electron cloud distribution, as shown in Fig. 4.19.

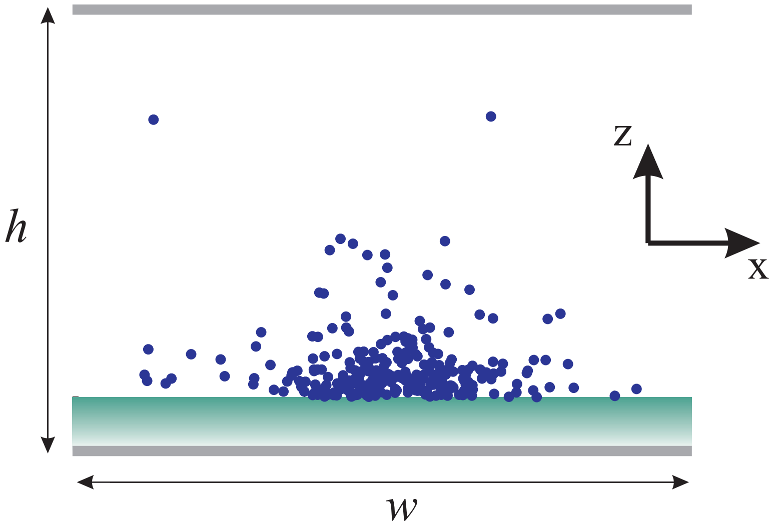

Figure 4.19.: Electron cloud distribution at the end of the simulation of the studied case (same parameters as in Fig. 4.18).

4.5. Summary

In this chapter, the long term evolution in parallel-plates waveguides loaded by a single dielectric slab has been investigated. After a brief review of the theory as well as of the literature, a 1D model able to take into account both the induced charge and the surface charge on the dielectric has been developed. The proposed model provides a qualitative overview of

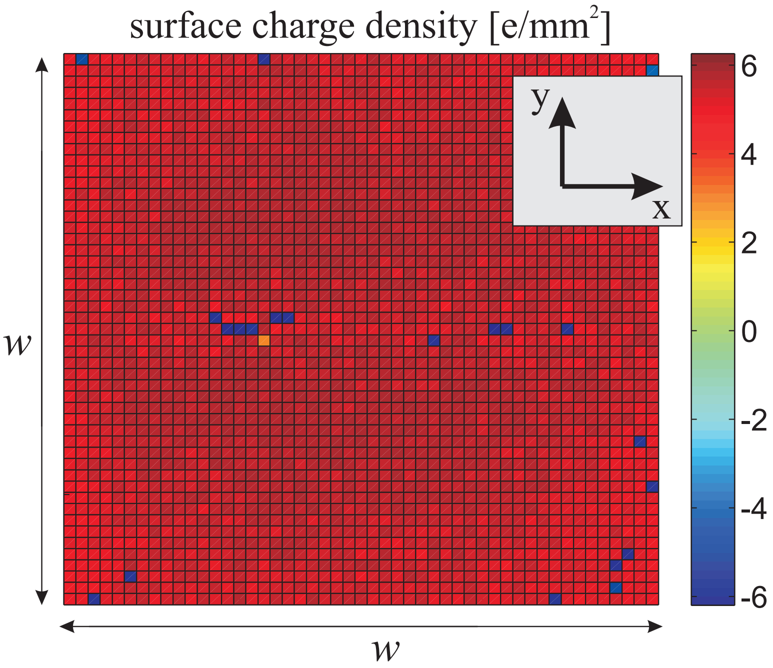

Figure 4.20.: Charge density on the dielectric surface at the end of the simulation of the studied case (same parameters as in Fig. 4.18)

the phenomenon through the long-term multipactor chart. Two different mechanisms have been reported: first, the self-extinguishing mechanism which occurs for, relatively, low gap voltages, close to the lower multipactor threshold, and, second, the self-sustaining mechanism that takes place for higher gap voltages. For the first time a saturation stage in parallel with the development of a surface charge on the dielectric has been reported. Since the 1D model cannot consider the spread of electrons due to secondary emission statistics as well as due to mutual Coulomb force between electrons, a advanced 3D model able to take into account all the long-term evolution mechanisms has been proposed. Results, obtained by the 3D approach, are in good agreement with the qualitative behavior of the electron population evolution as predicted by the 1D model. Additionally, the 3D analysis provides a deeper insight on the phenomenon through the electron cloud distribution as well as through the surface charge density on the dielectric.

The work presented in this Chapter triggers intense motivation for further studies both in terms of modeling and analysis of the phenomenon for the examined configuration. As a future step, the 3D solver could be efficiently boosted by applying accelerating techniques for N-body systems, like the fast multipole method (FMM). On the other hand the analysis of the phenomenon presents particular interest. A future step could be a comprehensive 3D study in order to verify the existence of the self-sustaining mechanism. Moreover, parametric studies regarding the effect of the dielectric slab properties (thickness and dielectric constant) will provide a deeper insight on the long-term multipactor evolution under the presence of dielectrics.

5. Image Method for Multilayered Shielded Media

5.1. Introduction

A robust analysis of the long-term multipactor evolution requires the calculation of all mutual interactions between electrons, included the effect of the charges induced on the component walls. As has been discussed in the Chapter 4, the induced charges can significantly affect the electron motion, especially when electron approaching the boundary walls. Their inclusion in the multipactor analysis involves the following peculiar issue: the evaluation of the electrostatic field on a source due to the charges induced by the source itself. Such a calculation can be achieved by the extraction of the singular source contribution from the Green Function (GF).

This work has been motivated by the exploration of a GF method that fits well to the above described feature in the case of multilayered shielded media, a configuration which has triggered extensive interest in multipactor analysis [32], [91]. Sommerfeld integration [92, 93], modal expansion (eigefunction expansion) [80, 94, 95] and image method (real image series) [96, 97] are three well-known approaches for evaluating the GF. Among them, the image method attracts most our interest since it provides a straightforward separation between the singular source term and the remaining, regular part of the GF. The extraction of the source term is naturally infeasible in the modal expansion since the singularity is incorporated in an infinite number of modes. On the other hand, the evaluation of the Sommerfeld integral is known to be a time consuming task. Alternatively, the complex image method (CIM) express the GF as a sum of the source term and a finite series series of complex images, i.e. images with complex position and charge [98, 99]. Comparing to real image series, CIM offers extra degrees of freedom arising from the complex representation of images. However, contrary to CIM, real images provide an exact, unique GF representation and a clear physical insight of the electrostatic problem as well.

Here, we focus on the derivation of the real image series in multilayered shielded media. Traditionally, an iterative procedure is applied in order to find the image charges in configurations with parallel boundaries, by using the image theory. A typical example is the image expansions for the problems of parallel plates. By following the same iterative procedure, the image series has been, also, derived for the case of a dielectric plate [100, 101] and of a grounded dielectric slab [102]. However, this process becomes a cumbersome task in case of multiple dielectric layers. To the author best knowledge, there is no work in the literature related to the image series problem in multilayered shielded media.

In this work, a new approach is proposed in order to derive the image series. The underlined concept is as follows: the image series are obtained by the modal expansion through the

Poisson summation formula [103]. In order to simplify the procedure, all the manipulations are performed in spectral domain. The strength of this approach is the fact that the modal expansion is relatively easy to be found in spectral domain. Then, by performing few manipulations, the Poisson summation formula is applied, transforming the modal expansion into an image series, in a closed form. As a first step, the case of a two layers shielded structure is studied. The method follows a generic process and it can be used as a base for future studies of cases with more than two layers.

The image series for the studied configuration can be also applied to a broader range of electrostatic problems. For example, consider a printed circuit board, shielded for electromagnetic compatibility purposes [104–106]. An electrostatic analysis can be, typically, performed by applying the well-established method of moments (MoM) [107], requiring efficient evaluations of the GF. The image method can be beneficially combined with modal expansion in order to efficiently fill the MoM matrix. This, in fact, is the main concept of the Ewald method which exploits the local efficiency of the image and modal expansion to close- and far-to-the-source distances, respectively [108–110].

The formulation of the proposed image method is presented in Section 5.2. The method is validated and studied in terms of convergence through numerical results in Section 5.3. Moreover, in Section 5.3, the utility of the derived image series is demonstrated in cases of practical importance. Finally, a brief summary and a discussion on possible extensions of the current work are included in Section 5.4.

5.2. Image Series Formulation

5.2.1. Green Function Derivation

As it has been already mentioned, in the proposed approach the main idea is to derive the image charges from the modal expansion by applying the Poisson Summation formula. In order to simplify the procedure, the potential Green function is manipulated in the spectral domain. After the image charges are found, both the potential and the electric field Green functions are directly derived. The problem of a parallel plate structure partially loaded by a dielectric slab is considered, as it is depicted in Fig. 5.1.

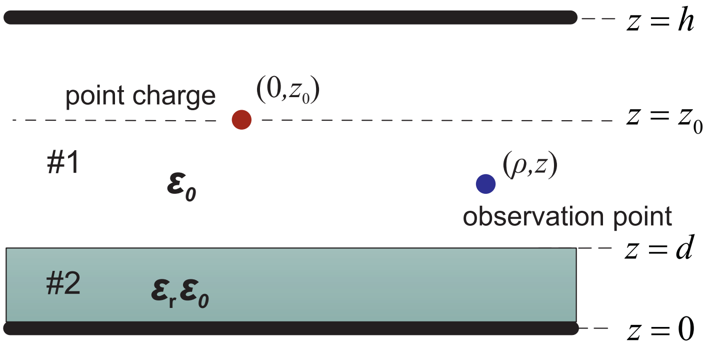

Figure 5.1.: Parallel plates waveguide partially loaded by a dielectric slab.

In electrostatics, the electric potential satisfies Poisson's Equation,

$$\nabla^2 V = -\frac{\rho_f}{\varepsilon_0}, \tag{5.1}$$

where ρ_f is the volume charge density. In order to simplify the calculations, a point source with a normalized charge of $q = -\varepsilon_0$ is considered. Hence, the volume charge density is given in cylindrical coordinates as $\rho_f = -\varepsilon_0 \frac{\delta(\rho)}{2\pi\rho} \delta\left(z - z_0\right)$.

By applying the Hankel Transform (HT), Eq. (5.1) is transformed to the spectral domain,

$$\frac{\partial^2 \tilde{V}}{\partial z^2} + \lambda^2 \tilde{V} = \frac{\delta\left(z - z_0\right)}{2\pi}, \quad \lambda^2 = -k_\rho^2 \tag{5.2}$$

where $\tilde{V}\left(k_\rho, z\right) = \mathrm{HT}\left\{V\left(\rho, z\right)\right\}$ is the Hankel Transform of the potential function. The corresponding homogeneous differential equation of Eq. (5.2) provides solutions $\tilde{f}\left(z\right)$, i.e eigenfunctions, which are linear combination of sines and cosines,

$$\tilde{f}\left(z\right) = \begin{cases} \tilde{f}_1 = a_1 \sin \lambda z + b_1 \cos \lambda z \\ \tilde{f}_2 = a_2 \sin \lambda z + b_2 \cos \lambda z \end{cases}, \tag{5.3}$$

where $\tilde{f}_1$ and $\tilde{f}_2$ correspond to the areas #1 and #2, respectively. The coefficients a_i, b_i, where $i = \{1, 2\}$, as well as the eigenvalues λ are determined by the boundary conditions,

$$\tilde{V}\left(h\right) = 0 \tag{5.4a}$$

$$\tilde{V}\left(0\right) = 0 \tag{5.4b}$$

$$\tilde{V}\,|_{z=d^-} = \tilde{V}\,|_{z=d^+} \tag{5.4c}$$

$$\varepsilon_r \frac{\partial \tilde{V}}{\partial z}\,|_{z=d^-} = \frac{\partial \tilde{V}}{\partial z}\,|_{z=d^+}. \tag{5.4d}$$

By applying them, it can be demonstrated that the eigenvalues satisfy the following characteristic equation,

$$\cot \lambda\left(d - h\right) - \varepsilon_r \cot \lambda d = 0 \tag{5.5}$$

which results in a set of discrete values λ_k, $k \in N$. The corresponding eigenfunctions have the following form:

$$\tilde{f}_k\left(z\right) = \begin{cases} \tilde{f}_{k,1} = C \frac{\sin \lambda_k (z-h)}{\sin \lambda_k (d-h)} \\ \tilde{f}_{k,2} = C \frac{\sin \lambda_k z}{\sin \lambda_k d} \end{cases}, \tag{5.6}$$

where C is an arbitrary constant. For simplicity, we choose $C = 1$.

The next step is to expand the normalized Green function $\tilde{V}\left(k_\rho, z\right)$ into a series of eigenfunctions,

$$\tilde{V} = \sum_{k=1}^{\infty} a_k \tilde{f}_k. \tag{5.7}$$

For this purpose, we define the following inner product between two eigenfunctions

$$\begin{aligned}\left\langle \tilde{f}_i, \tilde{f}_j \right\rangle &= \int_0^h \varepsilon_r(z)\, \tilde{f}_i(z)\, \tilde{f}_j(z)\, dz \\ &= \int_d^h \tilde{f}_i(z)\, \tilde{f}_j(z)\, dz + \varepsilon_{r,2} \int_0^d \tilde{f}_i(z)\, \tilde{f}_j(z)\, dz.\end{aligned} \tag{5.8}$$

Then, it can be shown that the eigenfunctions form an orthogonal basis, i.e.,

$$\left\langle \tilde{f}_i, \tilde{f}_j \right\rangle = 0 \quad \text{if} \quad i \neq j. \tag{5.9}$$

Substituting the expansion of Eq. (5.7) into the spectral Poisson Equation (5.2), and applying the inner product (5.8), one can find the expansion coefficient a_k. Finally, the spectral Green function is

$$\tilde{V}(k_\rho, z) = -\frac{1}{2\pi} \sum_{k=1}^{\infty} \frac{1}{\|f_k\|^2} \frac{\tilde{f}_k(z_0)\, \tilde{f}_k(z)}{\lambda_k^2 + k_\rho^2}, \tag{5.10}$$

which represents, in fact, the modal expansion in spectral domain, as will be discussed later.

The transcendental equation (5.5) cannot be solved analytically apart from very specific cases, that is for certain values of ε_r, d and h. However, it can be significantly simplified under the following assumption: the ratio between the plates gap and the slab width is a rational number. For practical cases, this always holds, since the geometrical dimensions are decimal numbers with a finite number of digits. Then, we can find two coprime integers p and q satisfying the following relation,

$$\frac{h}{h-2d} = \frac{p}{q}. \tag{5.11}$$

With this assumption, the solutions of the characteristic equation can be grouped into sets which are repeated with a period equal to

$$T = 2\pi \frac{p}{h} = 2\pi \frac{q}{h-2d}. \tag{5.12}$$

More specifically, it can be proved that there are $N = 2p$ solutions in the interval $(0, T]$, which compose a fundamental set of solutions (see the Appendix). Each of these fundamental solutions are repeated with the period T. A representative example of the periodic distribution of the eigenvalues into sets is illustrated in Fig. 5.2. Then, the eigenvalues can be described in the following form,

$$\lambda_{l,i} = \lambda_{0,i} + lT, \tag{5.13}$$

where $\lambda_{0,i}$ are the eigenvalues of the fundamental set, with $i = \{1, \cdots, 2p\}$, and $l \in \mathbb{Z}$. Taking into account the above form of eigenvalues the Green function of Eq. (5.10) can be written as a double summation over the indices i and l.

For demonstration purposes and without loss of generality, we continue the analysis focusing

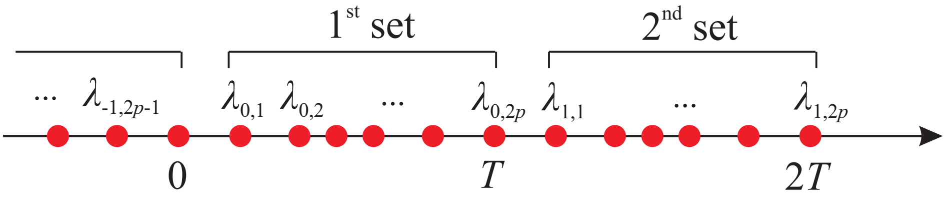

Figure 5.2.: Eigenvalues of the characteristic equation (5.5). The following configuration has been considered: $h = 1.5\,\mathrm{mm}$, $d = 0.25\,\mathrm{mm}$ and $\varepsilon_{r,2} = 9$. The corresponding integer coefficients of Eq. (5.11) are $p = 3$ and $q = 2$ while the fundamental period of the eigenvalues is equal to $T = 4\pi$.

on the area #1, i.e. $z, z_0 \in (d, h)$. Then, the Green function gets the following form,

$$\tilde{V}\left(k_\rho, z\right) = -\frac{1}{2\pi} \sum_{i=1}^{N} \sum_{l=0}^{\infty} U\left(\lambda_{l,i}\right) S\left(\lambda_{l,i}, z, k_\rho\right) \tag{5.14}$$

where the auxiliary functions U and S are given by

$$U\left(\lambda_{l,i}\right) = \frac{1}{a + b\cos 2\lambda_{l,i}\left(d - h\right)} \tag{5.15a}$$

and

$$S\left(\lambda_{l,i}, z, k_\rho\right) = \frac{\sin \lambda_{l,i}\left(z_0 - h\right) \sin \lambda_{l,i}\left(z - h\right)}{\lambda_{l,i}^2 + k_\rho^2}. \tag{5.15b}$$

The coefficients a and b depend only on the dimensions and the dielectric permittivity and are given by $a = (h - d)/2 + d\left(\varepsilon^2 + 1\right)/4\varepsilon$ and $b = -d\left(\varepsilon^2 - 1\right)/4\varepsilon$. Taking into account Eqs. (5.12) and (5.13) one can prove that the function U is independent of the index l and, thus, it can quit the inner sum. On the other hand, the product between the sines of the function S can be written as a sum of exponentials. Hence, the Green function can be rewritten as,

$$\begin{aligned} \tilde{V}\left(k_\rho, z\right) = &- \frac{1}{8\pi} \sum_{i=1}^{N} U\left(\lambda_{0,i}\right) \sum_{l=-\infty}^{\infty} \frac{e^{j\lambda_{l,i}(z - z_0)}}{\lambda_{l,i}^2 + k_\rho^2} \\ &+ \frac{1}{8\pi} \sum_{i=1}^{N} U\left(\lambda_{0,i}\right) \sum_{l=-\infty}^{\infty} \frac{e^{j\lambda_{l,i}(z + z_0 - 2h)}}{\lambda_{l,i}^2 + k_\rho^2}. \end{aligned} \tag{5.16}$$

The next step in order to derive the image expansion is to apply the Poisson Summation formula to the inner double-infinite sums of Eq. (5.16), i.e. the sums of index l. After some manipulations, the Green function takes on the form

$$\begin{aligned}\tilde{V}\left(k_\rho, z\right) = &-\frac{1}{8T}\sum_{i=1}^{N} U\left(\lambda_{0,i}\right) \sum_{m=-\infty}^{\infty} \frac{e^{-k_\rho\left|y_1+m\frac{2\pi}{T}\right|}}{k_\rho} e^{-jm\lambda_{0,i}\frac{2\pi}{T}} \\ &+\frac{1}{8T}\sum_{i=1}^{N} U\left(\lambda_{0,i}\right) \sum_{m=-\infty}^{\infty} \frac{e^{-k_\rho\left|y_2+m\frac{2\pi}{T}\right|}}{k_\rho} e^{-jm\lambda_{0,i}\frac{2\pi}{T}}, \end{aligned} \tag{5.17}$$

where $y_1 = z - z_0$ and $y_2 = z + z_0 - 2h$. The inner sums of index m correspond, in fact, to image expansions in the spectral domain, since $\mathrm{IHT}\left\{e^{-k_\rho z}/k_\rho\right\} = 1\Big/\sqrt{\rho^2+z^2}$. Then, the image series in spatial domain, extracting the normalization factor, is given by

$$V\left(\rho, z\right) = \frac{1}{4\varepsilon_0\pi}\sum_{n=-\infty}^{\infty}\left(\frac{w_n}{\sqrt{\rho^2+\left(z-Z_1^n\right)^2}} - \frac{w_n}{\sqrt{\rho^2+\left(z-Z_2^n\right)^2}}\right), \tag{5.18}$$

where the weights w_n and the image positions Z_1^n and Z_2^n are given in Table 5.1.

The modal expansion in spatial domain can be derived by applying the Inverse Hankel Transform to Eq. (5.10). Then, the Green function, extracting again the normalization factor, is given by the following modal series,

$$V\left(\rho, z\right) = \frac{1}{2\varepsilon_0\pi}\sum_{k=1}^{\infty} g_k G_k\left(\rho, z\right), \tag{5.19}$$

where

$$g_k = \frac{\sin\lambda_k\left(z_0 - h\right)}{a + b\cos 2\lambda_k\left(d-h\right)} \tag{5.20a}$$

and

$$G_k\left(\rho, z\right) = \sin\lambda_k\left(z-h\right)K_0\left(\lambda_k\rho\right) \tag{5.20b}$$

are the weight and the profile, respectively, of the modes, while K_0 is the modified Bessel function of the second kind. Note that the set of eigenvalues λ_k in Eqs. (5.20) corresponds to the one of eigenvalues $\lambda_{l,i}$ in Eq. (5.13) under the relation of $k = 2pl + i$.

A summary of the proposed technique for deriving the image series is given in Fig. 5.3.

Image Positions	Image Charges
$Z_1^n = z_0 - n\frac{h}{p}$	$w_n = -\frac{\pi}{2T}\sum_{i=1}^{2p}\frac{e^{-j2\lambda_{0,i}(d-h)\frac{n}{p+q}}}{a+b\cos 2\lambda_{0,i}(d-h)}$
$Z_2^n = 2h - z_0 - n\frac{h}{p}$	

Table 5.1.: Positions & Charges of the images.

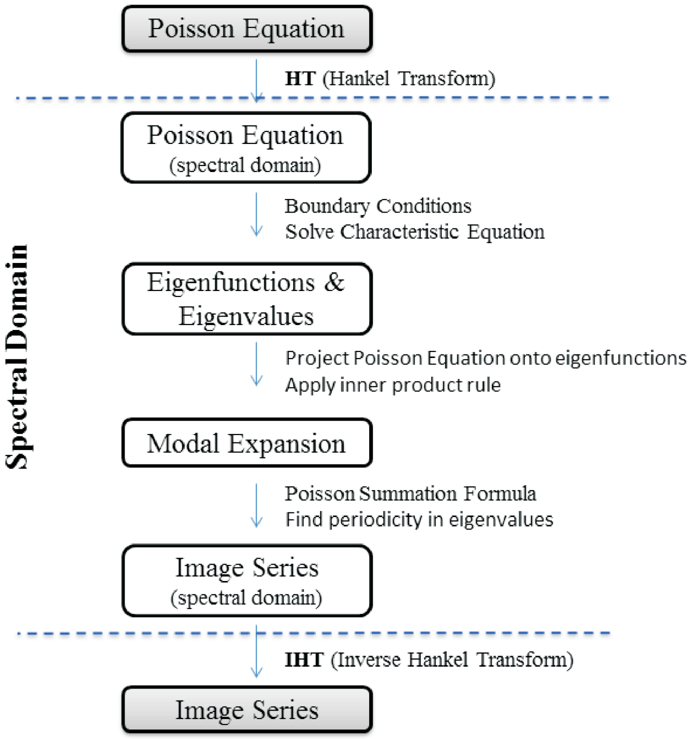
Poisson Equation
HT (Hankel Transform)
Poisson Equation
(spectral domain)
Boundary Conditions
Solve Characteristic Equation
Eigenfunctions &
Eigenvalues
Project Poisson Equation onto eigenfunctions
Apply inner product rule
Modal Expansion
Poisson Summation Formula
Find periodicity in eigenvalues
Image Series
(spectral domain)
IHT (Inverse Hankel Transform)
Image Series
Spectral Domain

Figure 5.3.: Main steps of the proposed image method.

5.2.2. Extraction of Singular Images

As can be shown using the image positions of Table 5.1, some images, corresponding to low values of index n, can fall into the observation area, i.e. into the interval (d, h). This would result in artificial electric potential singularities in positions where there are no sources. Consider, for example, the following configuration: parallel-plates of $h = 2$mm loaded by a dielectric slab of $\varepsilon_{r,2} = 2$ and $d = 0.25$mm. Figure 5.4 depicts the image charges, both position and amplitude, for this configuration. As can be seen, there are images located between the dielectric interface and the upper metallic plate. However, they all have zero charge. In particular, there are $p + q - 1 = 6$ images, around the main image ($n = 0$) of each set, which do not contribute. This can be generalized for any configuration parameters of h, d and $\varepsilon_{r,2}$. By applying Monte Carlo simulations, it has been verified that the first $p + q - 1$ images around the main ones have zero charge. This is a necessary and sufficient condition so that there is no artificial singularity for the electric potential in the observation area. Therefore, in the proposed method, all the images with $1 \leq |n| \leq p + q - 1$ are eliminated.

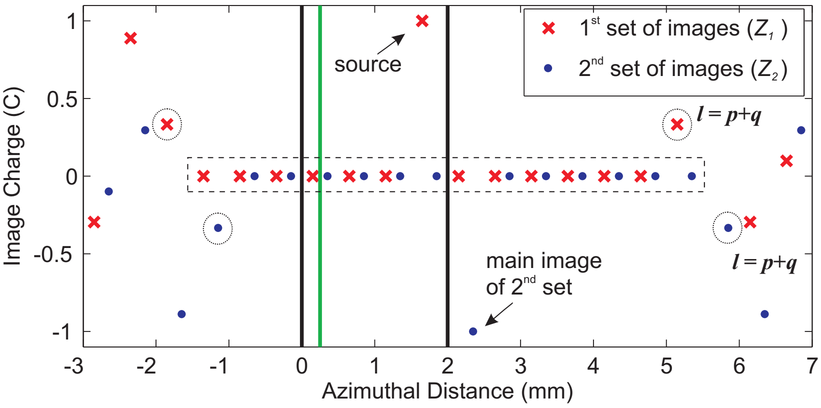

Figure 5.4.: Charges of the images for both set of images as defined in Table 5.1. The following configuration has been considered: $h = 2$mm, $d = 0.25$mm, $\varepsilon_{r,2} = 2$ and $z_0 = 1.65$mm. The vertical lines correspond to the margins of the structure: the two black lines represent the lower and the upper metallic plate, the green one the limit of the dielectric slab. The first images with zero charge are marked by the rectangular dashed box. The first images with non zero charge (excluding the main images of both sets, i.e. for $n = 0$), are marked with dashed circles.

5.3. Numerical Examples

In this section the validity and the performance of the proposed image method is discussed through some numerical examples. For this purpose, two other approaches for the evaluation of the GF have been applied, too. The first one is the modal expansion, as it has been derived in Eq. (5.19), the second one is based on the Sommerfeld integration [92].

According to this, the Green function is first evaluated in the spectral domain in a closed form. Then, the spatial domain Green function is calculated by applying the Sommerfeld integration, i.e.

$$V(\rho, z) = \int_0^\infty J_0(k_\rho \rho)\, k_\rho \tilde{V}(k_\rho, z)\, dk_\rho, \tag{5.21}$$

where J_0 is the zero order Bessel function of the first kind. By applying the boundary conditions in the configuration under study, the potential Green function $\tilde{V}$ in the spectral domain is given in a closed form as

$$4\pi\varepsilon_0 \tilde{V}(k_\rho, z) = \frac{e^{-k_\rho |z-z_0|}}{k_\rho} - \frac{e^{-k_\rho (z-z_0)}}{k_\rho} + C \sinh k_\rho (z-h), \tag{5.22}$$

where

$$C = -\frac{2}{k_\rho} \frac{\varepsilon_{r,2} \frac{\sinh k_\rho (z_0-d)}{\cosh k_\rho (h-d)} + \frac{\cosh k_\rho (z_0-d)}{\cosh k_\rho (h-d)} \tanh k_\rho d}{\varepsilon_{r,2} \tanh k_\rho (h-d) + \tanh k_\rho d}. \tag{5.23}$$

Then, the electric field GF can be obtained as

$$\mathbf{E}(\rho, z) = -\nabla V = E_\rho \hat{\rho} + E_z \hat{\mathbf{z}} \tag{5.24}$$

where the components E_ρ and E_z are given by the following equations

$$E_\rho = \int_0^\infty J_1(k_\rho \rho)\, k_\rho^2 \tilde{V}(k_\rho, z)\, dk_\rho \tag{5.25a}$$

and

$$E_z = -\int_0^\infty J_0(k_\rho \rho)\, k_\rho \frac{\partial \tilde{V}(k_\rho, z)}{\partial z} dk_\rho. \tag{5.25b}$$

A numerical evaluation of the Sommerfeld integrals of Eqs. (5.21) and (5.25) is performed by applying the Weighted Averages (WA) algorithm, as described in [111].

In the next examples, the following configuration has been considered: the distance between the metal plates is equal to $h = 1$mm while the dielectric slab has a width of $d = 0.3$mm and a dielectric constant equal to $\varepsilon_{r,2} = 2$. The results have been obtained utilizing MATLAB R2013a on a PC with an Intel Core i7 CPU at 3.40 GHz, running on Windows 7 Professional x64 operating system. Table 5.2 provides data about the CPU time needed for the evaluation of the elementary elements for each of the applied methods, e.g. the potential GF evaluation due to a single mode for the modal expansion method. As can be seen, the CPU time needed for the evaluation of the contribution due to a single mode is more than 60 times higher than the corresponding one for a single image. This difference comes, in fact, from the time consuming evaluation of the Bessel functions needed in the modal series. The difference becomes even more evident for the case of Sommerfeld integration, since the evaluation of every partial integral requires several calls of the Bessel function.

	CPU time per single term	
	G_v	G_e
Image Series	$\tau_{ref} \simeq 10^{-4}$ms	1.5 τ_{ref}
Modal Series	65 τ_{ref}	95 τ_{ref}
Sommerfeld Integration	620 τ_{ref}	–

Table 5.2.: CPU time for the calculation of a single term of each method.

5.3.1. Validation

Several tests have been performed in order to prove the validity of the developed image method. Figure 5.5 depicts representative results for the potential GF, for a case in which the observation point approaches radially the source. As it is shown, the image series follows very well the other two approaches through the major radial range. The discrepancies noticed for high values of radial distance come from the fact that the image series converge, in general, very slowly when the observation and the source point are far away. As can be seen, by increasing the number of calculated terms, the differences observed for high radial distances diminish, validating, thus, the proposed image technique.

The agreement between the methods is confirmed by results for the electric field GF, too. Figure 5.6 illustrates results for a case where the source and the observation points are located at different z levels. As shown, the three methods are in a nice consistency for both $z-$ and $\rho-$components. As expected, due to the symmetry of the problem, the $\rho-$component is diminished as the observation point approaches the azimuthal axis and the total electric field is dominated by the $z-$ component.

5.3.2. Convergence

After validating the proposed method, we have performed a numerical study of the convergence of the image series. Figure 5.7 depicts results on the number of terms needed in order to achieve a certain accuracy. Two cases are presented: one where the source is close to the dielectric slab and one where it is close to the metal plate. In both cases the image series present similar asymptotic behavior as the error becomes very low. As can be seen, for high accuracy ($err < 10^{-5}$) the number of images needed is proportional to $N \propto err^{-1/2}$ or, equivalently, the potential GF converges with a rate of $\propto 1/N^2$. On the other hand, the modal expansion presents a faster asymptotical convergence. This makes it a better choice in case a very high accuracy is required. However, a fair comparison between the two methods requires to consider the CPU time needed for each term. Taking into account the data of Table 5.2 the image method outperforms the modal expansion in the studied cases for errors larger than $err > 10^{-8}$.

In the case of electric field GF a different trend is noticed for the convergence of the image series. As Fig. 5.8 shows, the image series converge faster in the case that the source is located close to the metal plate. In particular, when the source is near to the dielectric slab the electric field GF converges with the same rate as the potential GF, i.e. $\propto 1/N^2$, while,

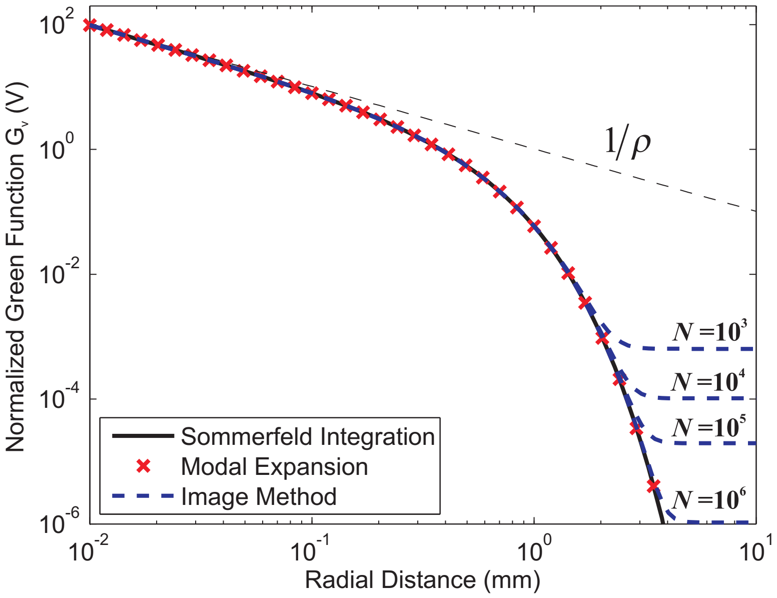

Figure 5.5.: Potential Green function as a function of the radial distance between the source and the observation point. The source and the observation point are placed on the same altitude position of $z_0 = z = 0.5$mm. A number of $N_{\mathrm{mod}} = 1000$ modes and $N_{\mathrm{WA}} = 35$ partial integrals has been used for the modal expansion and the Sommerfeld integration, respectively, while several simulations with different number of images have been performed.

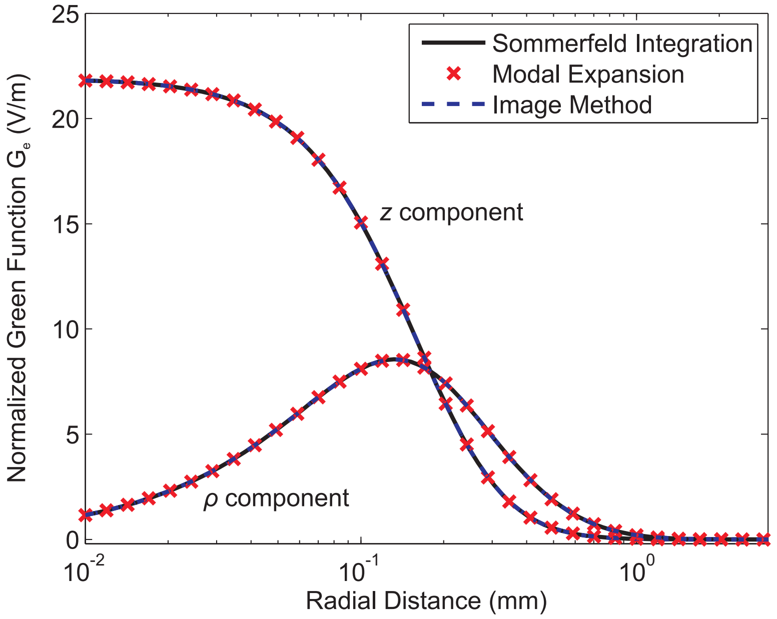

Figure 5.6.: Electric field GF (both $z-$ and $\rho-$components) as a function of the radial distance. The altitude position of the source and the observation point are $z_0 = 0.4$mm and $z = 0.6$mm, respectively.

when the source is close to the metal boundary the convergence is asymptotically proportional to $\propto 1/N^3$. After having performed several numerical experiments, we have found out that these two behaviors constitute the limit cases for the asymptotic forms of the electric field GF obtained by image series.

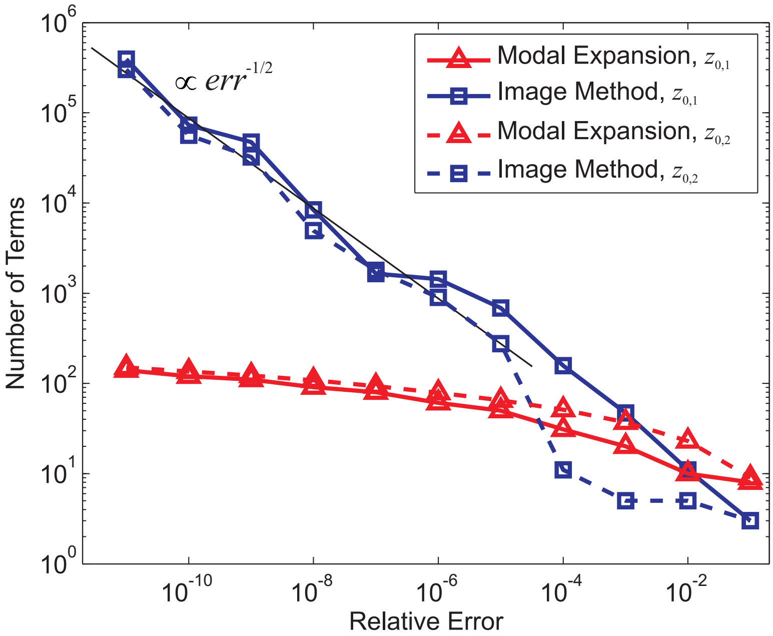

Figure 5.7.: Convergence of the potential GF. Two different cases are studied: in the first one the source is located close to the dielectric surface with $z_{0,1} = d + 0.1\,(h-d)$ and in the other the source is close to the metal plate with $z_{0,2} = h - 0.1\,(h-d)$. For both cases, the observation point is placed on the same altitude level as the corresponding source and in a radial distance of $\rho = 0.05h$.

In the previous examples we have studied the convergence considering a single observation point. The same asymptotic behaviors take place even if the observation point is placed in different positions with respect to the source. As the observation point is getting closer to the source the curves in Figs. 5.7 and 5.8 become lower for the image method and higher for the modal expansion. For a better overview of the image series convergence, the influence of the source-to-observer distance has been also investigated. Figure 5.9 depicts results on the relation between the relative error and the position of the observer, for a certain number of calculated terms. It is obvious that for close distances the electric field GF for the image method converges much faster than the potential GF, with a rate of $\propto \rho^2$ instead of $\propto \rho$, respectively. On the other hand, the modal expansion follows a similar tendency for both potential and electric field GF.

5.3.3. Efficiency and Accuracy

In this part we study the computational performance of the image series method in some examples of practical importance. As a first example, we evaluate the potential GF considering

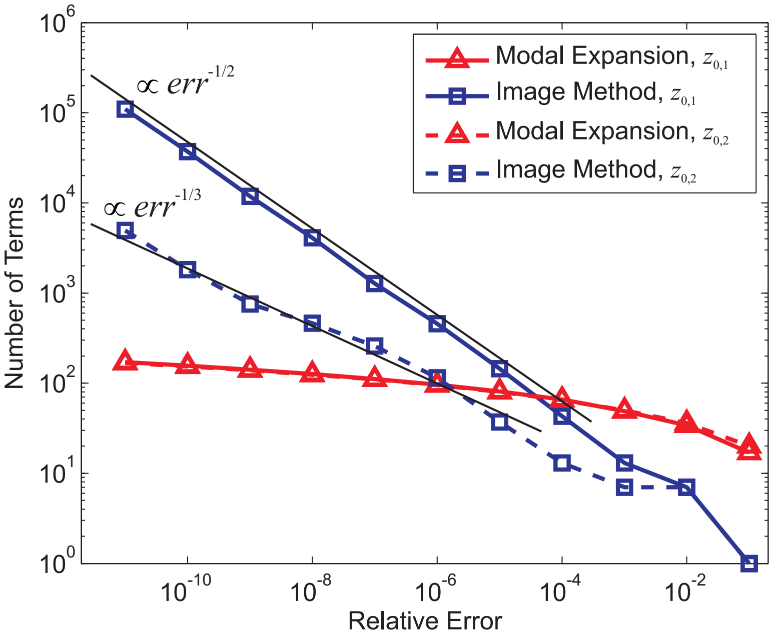

Figure 5.8.: Convergence of the electric field GF. Two different cases are studied: in the first one the source is located close to the dielectric surface with $z_{0,1} = d + 0.1\,(h - d)$ and in the other the source is close to the metal plate with $z_{0,2} = h - 0.1\,(h - d)$. For both cases, the observation point is placed at the same altitude level as the corresponding source and in a radial distance of $\rho = 0.05h$.

.

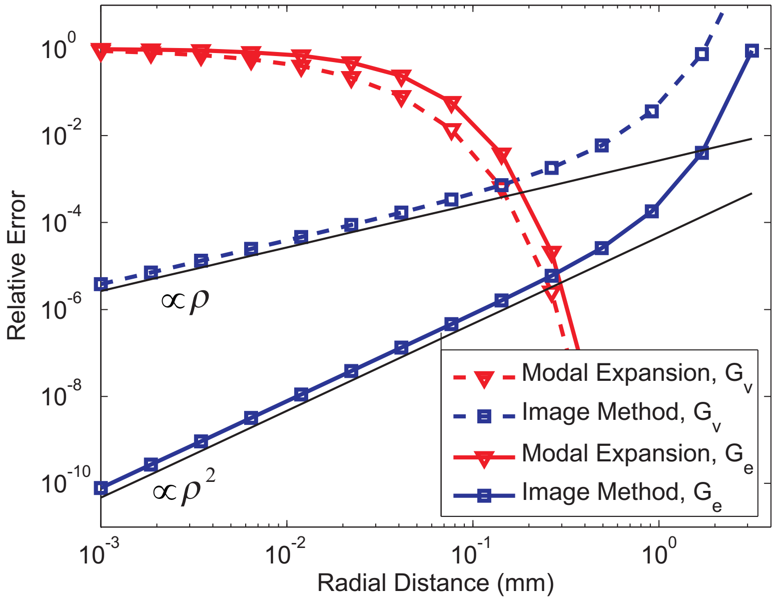

Figure 5.9.: Relative error of the Green function as a function of the radial distance. A number of $N_{\text{imag}} = 1000$ and $N_{\text{modes}} = 15$ has been considered, resulting in the same CPU time for both image and modal series simulations. The source and observer are placed on the same altitude level of $z_0 = z = 0.5$mm.

.

both source and observation points located on the dielectric surface. This case is encountered in the analysis of shielded printed circuits by using the Method of Moments (MoM). As Fig. 5.10 shows, the image method presents a remarkable computational efficiency for low radial distances, outperforming both modal expansion and the Sommerfeld integration technique for distances, approximately, up to $\rho = 0.5h$. Therefore, the image method could contribute in a MoM analysis by fast GF evaluations between neighbor patches. However, image series performance is limited to a point where the computational effort, needed for achieving a certain accuracy, explodes resulting in huge CPU evaluation times.

The second example is related to another area, the one of particle dynamics studies which are frequently encountered in plasma physics. In this case, in order to evaluate the motion of the charged particles the mutual interactions between particles, and especially between near particles, need to be calculated. Since the number of the considered particles is huge (typically higher than 10^5) and the mutual Coulomb field is evaluated in each time step, a compromise between accuracy and computational complexity needs to be done. Here, as an example, we assume a homogeneous distribution of 10^4 electrons in the area of $\rho \in [0, h]$ and $z \in [d, h]$. Then, we evaluate the electric field on these electrons due to a source located at $(\rho, z_0) = (0, h/2)$. Both image and modal series have been applied. The number of terms for each method has been chosen so that the total CPU time for both methods is approximately the same, $t_{\text{imag}} \approx t_{\text{modes}} = 1.5$s. Figures 5.11 and 5.12 depict the relative error of the electric field GF over the examined area as obtained by the image and the modal series, respectively. As can be seen, the image method provides an accuracy of at least 3 significant

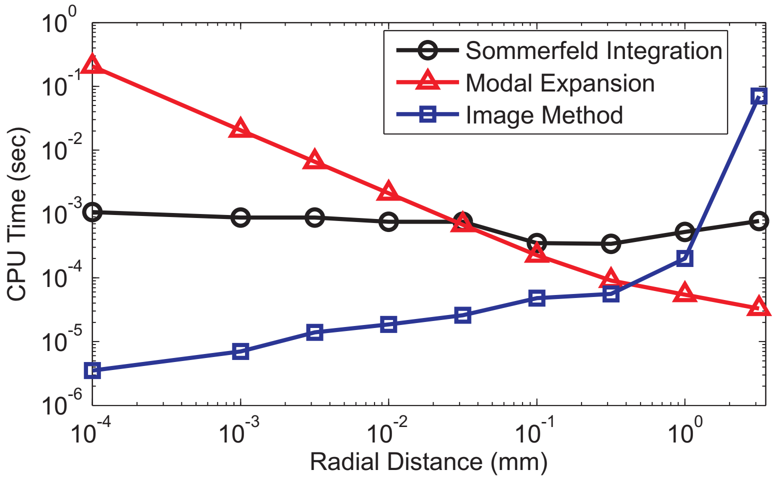

Figure 5.10.: CPU time needed for the calculation of the potential Green Function with a relative error equal to 10^{-5}. The source and the observation point are considered to be placed on the dielectric surface, i.e. $z_0 = z = d = 0.3$mm.

digits (error lower than 10^{-4}) all over the examined area, which can be considered sufficient for the computationally demanding particle simulations. Indeed, for near to the source distances, where the electric field is higher and consequently its consideration is more important for the particles motion, the image method yields higher precision, outperforming the modal series in the area for $\rho < 0.35h$. Although the modal expansion method provides very high accuracy far from the source, it fails to efficiently evaluate the electric field close to the source.

In continuance to the previous example, another issue appearing in the studies of particle dynamics is the evaluation of the force on the source due to the charges induced by the source itself on metal surfaces. This force can significantly affect the motion of a charged particle, especially when it is located close to metal surfaces. In order to evaluate it, one should calculate the electric field on the source, coming from the induced charges. For simplicity, let us call it 'self-field'. In order to evaluate the self-field, the singular free space contribution of the source should be extracted by the GF. This is straightforward in the image method, since the self-field can be directly obtained by the substraction of the source term, i.e. $w_0 \Big/ \sqrt{\rho^2 + \left(z - Z_1^0\right)^2}$, in the summation formula of Eq. (5.18). On the contrary, it is practically impossible to evaluate the self-field by the modal expansion since the source singularity is incorporated in all modes and an infinite number of terms is required in order to accurately extract it.

Figure 5.13 depicts the self-field as a function of the source position along the vertical axis. In addition to the image method, a Sommerfeld integration of Eq. (5.25b) has been applied extracting the first term of Eq. (5.22) which corresponds to the source in the spectral domain. As it is seen, when the source approaches any of the two surfaces, the self-field becomes stronger and it results in a force, always towards the surface. The asymmetry observed between the upper metal plate ($z = h$) and the lower dielectric surface ($z = d$) is due to the presence of the single dielectric slab.

Figure 5.14 illustrates the results with respect to the computational performance of the

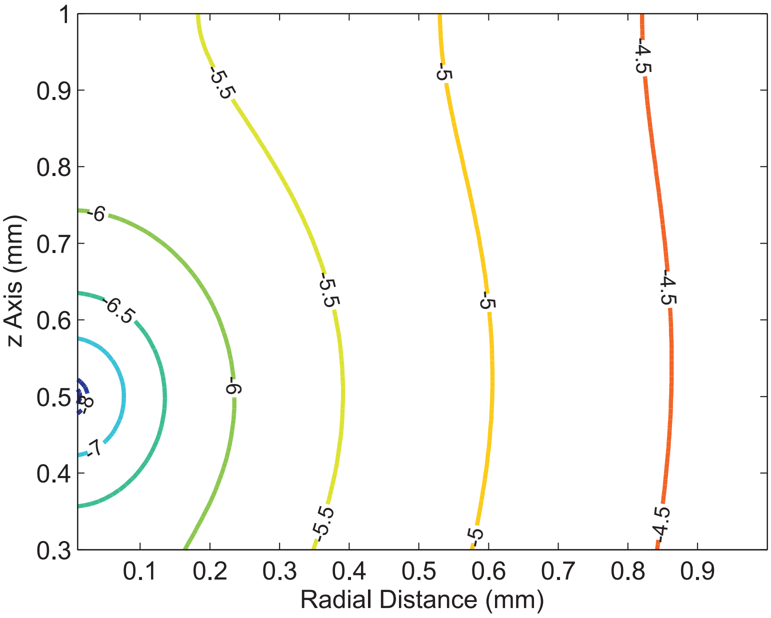

Figure 5.11.: Relative error of the electric field Green function obtained by the proposed image method considering the first $N_{\mathrm{imag}} = 1000$ terms. In total, 10^4 observation points have been simulated resulting in a CPU time of approximately 1.59 sec

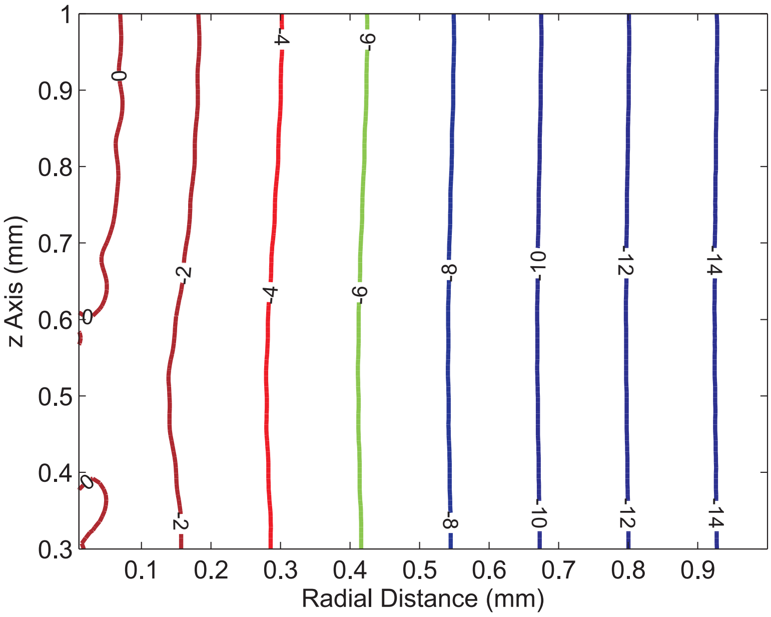

Figure 5.12.: Relative error of the electric field Green function obtained by modal expansion considering the first $N_{\mathrm{modes}} = 15$ terms. In total, 10^4 observation points have been simulated resulting in a CPU time of approximately 1.51 sec

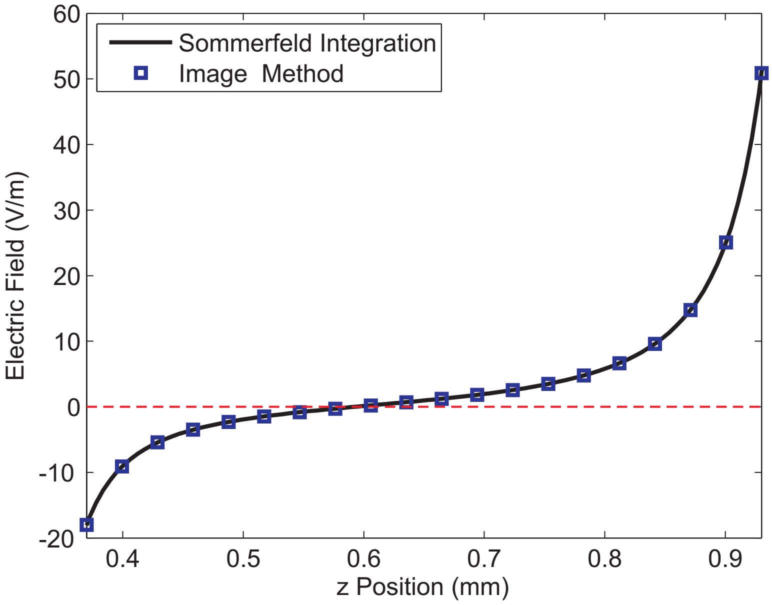

Figure 5.13.: Electric field on the source due to the induced charges, along the z axis. For the image method, a number of $N_{imag} = 1000$ terms has been used.

image method regarding the evaluation of the self-field. In order to have a comparison, an adaptive scheme, able to guarantee a certain accuracy, has been also applied in order to evaluate the self-field via the Sommerfeld integration. The applied scheme is based on the 16-points Gauss-Legendre quadrature rule. As it is shown, the image series perform better when the source is close to the boundaries. In such a case, fast convergence is achieved since the main contribution of the electric field comes from the closest-to-the-source image, located symmetrically to the boundary.

5.4. Conclusion

In this chapter, a new approach for the derivation of image series in layered, shielded media has been presented. The proposed technique constitutes an alternative to the conventional iterative process for image series derivation and it provides an exact, single series solution in a closed form. In this work, the technique has been derived for the case of two layers. However, the algorithm is based on a general concept, as Fig. 5.3 illustrates. As a continuance to the present work, the main steps of the proposed algorithm can potentially constitute the base of an extended technique able to derive the image series in general multilayer shielded structures.

The derived image series has been validated through comparisons with the modal expansion and Sommerefeld integration methods. Through numerical studies, we have also reviewed the asymptotical behavior of the series convergence. It has been shown that the electric field GF presents a faster convergence than the corresponding GF for the potential, especially when the source is placed close to the metal surface. The utility of the image method in the studied configuration has been demonstrated by some examples of practical interest. The image series

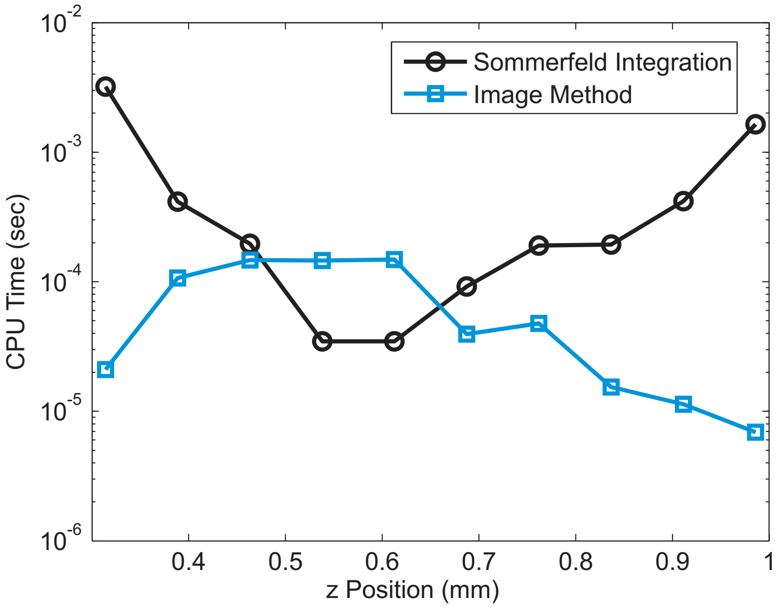

Figure 5.14.: CPU time needed for the calculation of the induced electric field on a source considering a relative error of 10^{-5}.

can be successfully complement other methods, like the modal expansion, for a fast evaluation of the GF in close-to-the-source distances. In general, the image method fits well to problems where a compromise between speed and accuracy needs to be found, since it provides fast GF evaluations for medium order of accuracy.

6. Summary and Perspectives

The phenomenon of multipactor evolves mainly in two phases: it starts with a fast growth of the electron population and finishes in the steady state during which the population reaches a saturation level and remains almost constant. While state-of-the-art computational models focus mainly on the first phase, the steady state can provide valuable information about the discharge, such as the radiated power density spectrum, the number of electrons involved in the breakdown, the head load of the waveguide to mention only but a few.

This thesis contributed to the modeling of long-term multipactor. After a profound review of the physics involved in the discharge a generalized technique able to analyze multipactor in arbitrary 1D configurations has been developed. For this, a generalized single electron model has been used. Based on this model, studies considering the effect of low-energy electron collisions and single-surface multipactor in non-uniform field, like for example in coaxial waveguides, have been considered. For a rigorous modeling, a full 3D multiple particle model for the secondary emission has been applied. The single electron model together with the 3D secondary emission model allows a fast and precise multipactor analysis as required in the design and synthesis of hardware but provides also physical insight to the steady-state regime.

Another important technological topic are components involving dielectrics. While multipactor is mainly studied in pure metal environments, little is still known about the discharge evolution in the presence of dielectrics. The developed single electron model has been extended to include dielectrics taking into account the effects of both the space charge and the the surface charge developed on the dielectric during the discharge. For the first time, the multipactor evolution has been modeled taking fully into count these two contributions that are mainly responsible for the steady-state behavior of the breakdown.

In this framework, for taking into count efficiently the effect of induced charges, the image series representation of the 3D Green Function for multi-layered media has been used. For this, a novel approach in order to derive the images series has been developed. It is based on the modal expansion of the Green Function and subsequently transformed into a real image series through the Poisson summation formula. The strength of this approach lies in the fact that the modal expansion can be quite easily obtained in the spectral domain. Then, by applying the Poisson summation formula an image series in closed form is obtained. This concept has been applied two a parallel-plates configuration with a dielectric slab but can be generalized to an arbitrary number of dielectric layers.

Perspectives

A direct continuation of this thesis would consist in the generalization of the image series of parallel-plates loaded with a dielectric slab to shielded multi-layered media with an arbitrary number of dielectric layers. In this framework, it would be also interesting to explore the possibility to apply concepts like the Ewald summation technique to accelerate the numerical evaluation of the 3D Green Function. Thus, it needs to be studied how to combine effectively the image series representation and the modal expansion of the Green Function of the multi-layered structure.

In this context, the application of the Fast Multipole Method (FMM) is an interesting direction to follow as well in order to increase the number of particles used in the simulations and to path the way to a full 3D simulation of steady-state multipactor in the presence of dielectrics.

The efficient and accurate modeling of the surface charge on the dielectric remains an open topic as well. Either, the surface charge is modeled as individual particles requiring methods like the FMM in order to simulate a reasonable number of particles. Another possibility would be the representation of the surface charge density by appropriate basis functions, e.g. piece-wise constant functions on a grid. Another intersting question is the surface charge distribution during the steady-state. First results seem to indicate that the distribution of the charge density converges to a constant distribution, which would allow to simplify its modeling. These results should be confirmed by further simulations and more accurate, full 3D models.

Concerning the study of the elastic reflection of impacting electrons, the results obtained in this thesis should be verified by a full 3D simulation. For this a particle-in-cell code or any other 3D method should be used, applying the 3D model of secondary emission.

Finally, in the framework of coaxial waveguides, it would be interesting to identify the different saturation mechanisms as it has been done for parallel-plates. This would provide analytical formulae for the number of electrons involved in the discharge, which could be used to link the experimentally observed radiated power density spectrum to the simulated one, allowing to define a unique criterion for multipactor onset in coaxial waveguides.

A. Solution of the Characteristic Equation

By applying the trigonometric identity $2\sin\theta\cos\varphi = \sin(\theta+\varphi) + \sin(\theta-\varphi)$, the characteristic equation (5.5) becomes

$$\sin(\omega_a\lambda) + c\sin(\omega_b\lambda) = 0, \tag{A.1}$$

where $\omega_a = h$, $\omega_b = h - 2d$ and $c = (\varepsilon_{r,2} - 1)/(\varepsilon_{r,2} + 1) < 1$. Then, the solutions of the characteristic equations will be the roots of the following function

$$h(x) = \sin(\omega_a x) + c\sin(\omega_b x)\,. \tag{A.2}$$

Although the characteristic equation consists of periodic trigonometric functions, its solutions are general non-periodic. Periodicity is guaranteed only when the ratio between ω_a and ω_b is a rational number. Due to the significant simplification of the analysis in such a case, here we assume that this condition is satisfied and consider

$$\frac{\omega_a}{\omega_b} = \frac{p}{q}, \tag{A.3}$$

where p and q are coprime integers. Note that such an assumption does not limit the accuracy by any means, since any real number is the limit of a sequence of rational numbers. Furthermore, in all practical situations, h and d are known to a limited number of digits.

Under this assumption, the period of the solutions of Eq. (A.1) reads

$$T = p\frac{2\pi}{\omega_a}. \tag{A.4}$$

Periodicity implies that the full set of solutions of (A.1) can be derived from the first N positive solutions, $\lambda_{0,1}, \lambda_{0,2}, \cdots, \lambda_{0,N}$, in the interval $(0, T]$ as

$$\lambda_{l,i} = \lambda_{0,i} + lT, \tag{A.5}$$

where $l \in \mathbb{Z}$. For this reason, we call $\lambda_{0,1}, \lambda_{0,2}, \cdots, \lambda_{0,N}$ the 'fundamental solutions' of the characteristic equation.

The fact that $c < 1$ leads to a very interesting result about the solutions of Eq. (A.1). In particular, it can be shown that there is one, and only one, solution between

$$x_1 = (2k+1)\frac{\pi}{2\omega_a} \tag{A.6a}$$

and

$$x_2 = (2k+3)\frac{\pi}{2\omega_a} \tag{A.6b}$$

where $k \in \mathbb{Z}$, corresponding to two sequential extrema of $\sin(\omega_a x)$.

In order to prove this property, we first consider that k is an even number. Then, it is easy to show that $h\left(x_1\right) = 1 + c\sin\left(\omega_b x_1\right)$ and $h\left(x_2\right) = -1 + c\sin\left(\omega_b x_1\right)$. Since $c < 1$, $h\left(x_1\right) > 0$ and $h\left(x_2\right) < 0$, showing that there is at least one root in the interval (x_1, x_2), which, as we will next show using 'proof by contradiction', is the only one in the corresponding interval. In particular, if more than one roots existed in the interval (x_1, x_2), there would be at least one root, $x_{r,2}$, satisfying the conditions

$$h\left(x_{r,2}\right) = 0 \tag{A.7a}$$

and

$$h'\left(x_{r,2}\right) \geq 0, \tag{A.7b}$$

as graphically explained in Fig. A.1. Substituting Eq. (A.1) into Eqs. (A.7) yields

$$\sin\left(\omega_a x_{r,2}\right) = -c\sin\left(\omega_b x_{r,2}\right) \tag{A.8a}$$

and

$$\omega_a \cos\left(\omega_a x_{r,2}\right) + c\,\omega_b \cos\left(\omega_b x_{r,2}\right) \geq 0. \tag{A.8b}$$

Observing that $\cos\left(\omega_a x\right) < 0$ in the interval (x_1, x_2), we can take the square of Eq. (A.8b) after bringing the first term in the left-hand side to the right hand-side, resulting in

$$\omega_a^2 \cos^2\left(\omega_a x_{r,2}\right) \leq c^2 \omega_b^2 \cos^2\left(\omega_b x_{r,2}\right). \tag{A.9}$$

Taking also the square of Eq. (A.8a) yields

$$\sin^2\left(\omega_a x_{r,2}\right) = c^2 \sin^2\left(\omega_b x_{r,2}\right). \tag{A.10}$$

Substituting the last equation into Eq. (A.9) and taking into account that $\omega_a \geq \omega_b$, the system of Eqs. (A.8) ends up to the following inequality

$$c > 1, \tag{A.11}$$

which is in contradiction with the definition of $c = (\varepsilon_{r,2} - 1)/(\varepsilon_{r,2} + 1) < 1$. Therefore, no more than one solutions can be found in the interval (x_1, x_2). Similar conclusions can be derived when k is an odd number.

Since there is a only one root in every interval (x_1, x_2), and since there are $2p$ such intervals in a period T, as can be found by the ratio $T/(x_2 - x_1)$ through (A.4) and (A.6), we conclude that there are $N = 2p$ fundamental solutions.

According to Eq. (A.5), the knowledge of the fundamental solutions, $\lambda_{0,1}, \lambda_{0,2}, \cdots, \lambda_{0,2p}$, is sufficient for the calculation of all the eigenvalues. The fundamental solutions can be numerically evaluated by applying a root-finding algorithm in each interval (x_1, x_2), for $k = 0, 1, \cdots 2p - 1$. However, only the first $p - 1$ solutions actually need to be evaluated through

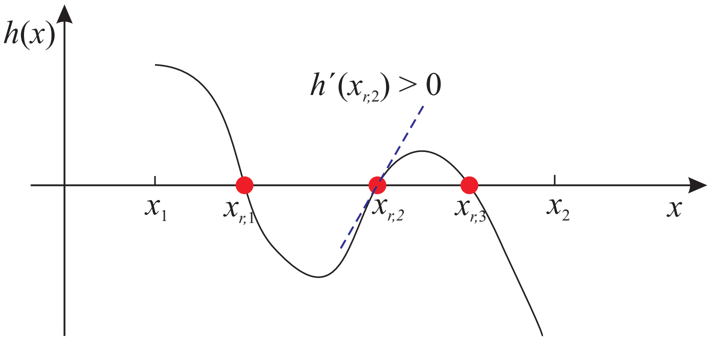

Figure A.1.: Graphical explanation of the conditions described in Eq. (A.7). The integer k of Eq. (A.6) is considered to be even, resulting in $h(x_1) > 0$ and $h(x_2) < 0$. Considering the existence of multiple roots, there would be at least one satisfying $h'(x_r) \geq 0$. In the depicted case, this corresponds to the root $x_{r,2}$, as it is illustrated by the tangent, dashed, line. The equality holds in the extreme case where two roots, e.g. $x_{r,2}, x_{r,3}$, overlap.

numerical solution of Eq. (A.1) while the rest can be obtained by the following formulas:

$$\lambda_{0,p} = T/2, \tag{A.12a}$$

$$\lambda_{0,2p} = T \tag{A.12b}$$

and

$$\lambda_{0,N-i} = T - \lambda_{0,i}, \quad i = 1, \cdots p-1. \tag{A.12c}$$

The first two relations are easily derived by direct substitution into Eq. (A.1). The last relation can be derived as follows: due to the odd symmetry of Eq. (A.1) if λ is an eigenvalue, $-\lambda$ is also an eigenvalue. Since the eigenvalues are periodic with period T, it follows that $T - \lambda$ is also an eigenvalue. Assuming that $\lambda_{0,i}$ is the eigenvalue in the i-th interval (the interval calculated from Eq. (A.6) for $k = i - 1$), it is not difficult to show that $T - \lambda_{0,i}$ belongs to the $(N - i)$-th interval, thus completing the proof of Eq. (A.12c).

Bibliography

[1] A. Woode and J. Petit, "Investigations into multipactor breakdown in satellite microwave payloads," *ESA Journal*, vol. 14, pp. 467–478, 1990.

[2] European Cooperation for Space Standardization (Organization), European Space Research, and Technology Centre and Requirements & Standards Division, *Space Engineering: Multiplication Design and Test*, ser. ECSS-E-20-01A. ESA-ESTEC, 2003.

[3] J. de Lara, F. Perez, M. Alfonseca, L. Galan, I. Montero, E. Roman, and D. Garcia-Baquero, "Multipactor prediction for on-board spacecraft rf equipment with the mest software tool," *Plasma Science, IEEE Transactions on*, vol. 34, no. 2, pp. 476–484, April 2006.

[4] V. Semenov, E. Rakova, D. Anderson, M. Lisak, and J. Puech, "Multipactor in rectangular waveguides," *Physics of Plasmas (1994-present)*, vol. 14, no. 3, p. 033501, 2007.

[5] K. Ohmi, "Beam-photoelectron interactions in positron storage rings," *Physical review letters*, vol. 75, no. 8, p. 1526, 1995.

[6] K. Ohmi, F. Zimmermann, and E. Perevedentsev, "Wake-field and fast head-tail instability caused by an electron cloud," *Physical Review E*, vol. 65, no. 1, p. 016502, 2001.

[7] G. Rumolo and F. Zimmermann, "Electron cloud simulations: beam instabilities and wakefields," *Physical Review Special Topics-Accelerators and Beams*, vol. 5, no. 12, p. 121002, 2002.

[8] S. Kurokawa and E. Kikutani, "Overview of the kekb accelerators," *Nuclear Instruments and Methods in Physics Research Section A: Accelerators, Spectrometers, Detectors and Associated Equipment*, vol. 499, no. 1, pp. 1–7, 2003.

[9] D. Preist and R. Talcott, "On the heating of output windows of microwave tubes by electron bombardment," *Electron Devices, IRE Transactions on*, vol. 8, no. 4, pp. 243–251, 1961.

[10] J. Vaughan, "Some high-power window failures," *Electron Devices, IRE Transactions on*, vol. 8, no. 4, pp. 302–308, 1961.

[11] L.-K. Ang, Y. Lau, R. A. Kishek, and R. M. Gilgenbach, "Power deposited on a dielectric by multipactor," *Plasma Science, IEEE Transactions on*, vol. 26, no. 3, pp. 290–295, 1998.

[12] E.-G. Schweppe, R. Bachmor, and E. Demmel, “Design and results of a 1.3 mw cw klystron for lep,” in *Particle Accelerator Conference, 1993., Proceedings of the 1993*. IEEE, 1993, pp. 1178–1180.

[13] F. Höhn, W. Jacob, R. Beckmann, and R. Wilhelm, “The transition of a multipactor to a low-pressure gas discharge,” *Physics of Plasmas (1994-present)*, vol. 4, no. 4, pp. 940–944, 1997.

[14] P. T. Farnsworth, “Television by electron image scanning,” *Journal of the Franklin Institute*, vol. 218, no. 4, pp. 411 – 444, 1934.

[15] E. Gill and A. Von Engel, “Starting potentials of high-frequency gas discharges at low pressure,” *Proceedings of the Royal Society of London. Series A. Mathematical and Physical Sciences*, vol. 192, no. 1030, pp. 446–463, 1948.

[16] A. J. Hatch and H. B. Williams, “The secondary electron resonance mechanism of low-pressure high-frequency gas breakdown,” *Journal of Applied Physics*, vol. 25, no. 4, pp. 417–423, 1954.

[17] ——, “Multipacting modes of high-frequency gaseous breakdown,” *Physical Review*, vol. 112, no. 3, p. 681, 1958.

[18] R. A. Kishek, Y. Y. Lau, L. K. Ang, A. Valfells, and R. M. Gilgenbach, “Multipactor discharge on metals and dielectrics: Historical review and recent theories,” *Physics of Plasmas (1994-present)*, vol. 5, no. 5, pp. 2120–2126, 1998.

[19] F. Zimmermann, “Review of single bunch instabilities driven by an electron cloud,” *Physical Review Special Topics-Accelerators and Beams*, vol. 7, no. 12, p. 124801, 2004.

[20] R. Udiljak, D. Anderson, P. Ingvarson, U. Jordan, U. Jostell, L. Lapierre, G. Li, M. Lisak, J. Puech, and J. Sombrin, “New method for detection of multipaction,” *IEEE transactions on plasma science*, vol. 31, no. 3, pp. 396–404, 2003.

[21] E. Sorolla, S. Anza, B. Gimeno, A. Perez, C. Vicente, J. Gil, F. Prez, F. D. Quesada, A. Álvarez, and V. E. Boria, “An analytical model to evaluate the radiated power spectrum of a multipactor discharge in a parallel-plate region,” *Electron Devices, IEEE Transactions on*, vol. 55, no. 8, pp. 2252–2258, 2008.

[22] G. Cheng and L. Liu, “Temporal evolution of multipactor electron discharge on a dielectric under excitation of high-power microwave,” *Plasma Science, IEEE Transactions on*, vol. 39, no. 4, pp. 1067–1074, 2011.

[23] A. Sazontov, V. Nechaev, and N. Vdovicheva, “The susceptibility diagrams of a multipactor discharge on a dielectric: Effects of rf magnetic field,” *Applied Physics Letters*, vol. 98, no. 16, p. 161503, 2011.

[24] H. Xiwei, S. Baipeng, and Z. Guanjun, “Pic-mcc simulation for hpm multipactor discharge on dielectric surface in vacuum,” *Plasma Science and Technology*, vol. 13, no. 6, p. 682, 2011.

[25] R. Kishek and Y. Lau, "Multipactor discharge on a dielectric," *Physical review letters*, vol. 80, no. 1, p. 193, 1998.

[26] A. Valfells, J. P. Verboncoeur, and Y. Y. Lau, "Space-charge effects on multipactor on a dielectric," *Plasma Science, IEEE Transactions on*, vol. 28, no. 3, pp. 529–536, 2000.

[27] G. Cheng, L. Liu, Y. Liu, and C. Yuan, "Monte carlo study of the single-surface multipactor electron discharge on a dielectric," *Plasma Science, IEEE Transactions on*, vol. 37, no. 10, pp. 1968–1974, 2009.

[28] J. Power, W. Gai, S. Gold, A. Kinkead, R. Konecny, C. Jing, W. Liu, and Z. Yusof, "Observation of multipactor in an alumina-based dielectric-loaded accelerating structure," *Physical review letters*, vol. 92, no. 16, p. 164801, 2004.

[29] O. V. Sinitsyn, G. S. Nusinovich, and T. M. Antonsen, "Self-consistent nonstationary two-dimensional model of multipactor in dielectric-loaded accelerator structures," *Physics of Plasmas (1994-present)*, vol. 16, no. 7, pp. –, 2009.

[30] O. Sinitsyn, G. Nusinovich, and T. Antonsen Jr, "Studies of multipactor in dielectric-loaded accelerator structures: Comparison of simulation results with experimental data," in *Advanced Accelerator Concepts: 14th Advanced Accelerator Concepts Workshop*, vol. 1299, no. 1, 2010, pp. 302–306.

[31] G. Torregrosa, A. Coves, C. P. Vicente, A. M. Perez, B. Gimeno, and V. E. Boria, "Time evolution of an electron discharge in a parallel-plate dielectric-loaded waveguide," *Electron Device Letters, IEEE*, vol. 27, no. 7, pp. 619–621, 2006.

[32] A. Coves, G. Torregrosa-Penalva, C. Vicente, B. Gimeno, and V. Boria, "Multipactor discharges in parallel-plate dielectric-loaded waveguides including space-charge effects," *Electron Devices, IEEE Transactions on*, vol. 55, no. 9, pp. 2505–2511, Sept 2008.

[33] S. Riyopoulos, "Multipactor saturation due to space-charge-induced debunching," *Physics of Plasmas (1994-present)*, vol. 4, no. 5, pp. 1448–1462, 1997.

[34] H. Bruining, *Physics and Applications of Secondary Electron Emission*, ser. Electronics and waves. Pergamon Press, 1954.

[35] E. J. Sternglass, "Theory of secondary electron emission by high-speed ions," *Phys. Rev.*, vol. 108, pp. 1–12, Oct 1957.

[36] R. Simon and B. Williams, "Secondary-electron emission," *Nuclear Science, IEEE Transactions on*, vol. 15, no. 3, pp. 167–170, June 1968.

[37] K. Kanaya and H. Kawakatsu, "Secondary electron emission due to primary and backscattered electrons," *Journal of Physics D: Applied Physics*, vol. 5, no. 9, p. 1727, 1972.

[38] C. Bouchard and J. Carette, "The secondary electron emission coefficient of disordered surfaces," *Surface Science*, vol. 100, no. 1, pp. 241 – 250, 1980.

[39] A. Shih, J. Yater, C. Hor, and R. Abrams, “Secondary electron emission studies,” *Applied Surface Science*, vol. 111, no. 0, pp. 251 – 258, 1997, proceedings of the International Vacuum Electron Sources Conference 1996.

[40] A.-G. Xie, H.-Y. Wu, and J. Xu, “Parameters of the secondary electron yield from metal,” *Journal of the Korean Physical Society*, vol. 62, no. 5, pp. 725–730, 2013.

[41] R. Willis and D. Skinner, “Secondary electron emission yield behaviour of polymers,” *Solid State Communications*, vol. 13, no. 6, pp. 685 – 688, 1973.

[42] I. Krainsky, K. Vaden, A. Curren, J. Dayton, J.A., and G. Mearini, “The angular distribution of elastically scattered electrons and computed impact on collector performance,” in *Electron Devices Meeting, 1992. IEDM ’92. Technical Digest., International*, Dec 1992, pp. 953–956.

[43] H. Seiler, “Secondary electron emission in the scanning electron microscope,” *Journal of Applied Physics*, vol. 54, no. 11, pp. R1–R18, 1983.

[44] C. Jardin, S. Kessas, B. Khelifa, P. Bondot, and B. Gruzza, “Energy dependence of the different electron emissions backscattered from polycrystalline molybdenum,” *Journal of Physics D: Applied Physics*, vol. 24, no. 7, p. 1115, 1991.

[45] J. H. Han, M. Krasilnikov, and K. Flöttmann, “Secondary electron emission in a photocathode rf gun,” *Phys. Rev. ST Accel. Beams*, vol. 8, p. 033501, Mar 2005.

[46] T. Koshikawa and R. Shimizu, “A monte carlo calculation of low-energy secondary electron emission from metals,” *Journal of Physics D: Applied Physics*, vol. 7, no. 9, p. 1303, 1974.

[47] Z. J. Ding, X. D. Tang, and R. Shimizu, “Monte carlo study of secondary electron emission,” *Journal of Applied Physics*, vol. 89, no. 1, pp. 718–726, 2001.

[48] Y. Lin and D. C. Joy, “A new examination of secondary electron yield data,” *Surface and Interface Analysis*, vol. 37, no. 11, pp. 895–900, 2005.

[49] M. Furman and M. Pivi, “Probabilistic model for the simulation of secondary electron emission,” *Phys. Rev. ST Accel. Beams*, vol. 5, p. 124404, Dec 2002.

[50] R. Cimino, I. Collins, M. Furman, M. Pivi, F. Ruggiero, G. Rumolo, and F. Zimmermann, “Can low-energy electrons affect high-energy physics accelerators?” *Phys. Rev. Lett.*, vol. 93, p. 014801, Jun 2004.

[51] A. Shih and C. Hor, “Secondary emission properties as a function of the electron incidence angle,” *Electron Devices, IEEE Transactions on*, vol. 40, no. 4, pp. 824–829, Apr 1993.

[52] D. Chernin, A. Drobot, and M. Kress, “A model of secondary emission for use in computer simulation of vacuum electronic devices,” in *Electron Devices Meeting, 1993. IEDM ’93. Technical Digest., International*, Dec 1993, pp. 773–776.

[53] J. R. M. Vaughan, “Multipactor,” *Electron Devices, IEEE Transactions on*, vol. 35, no. 7, pp. 1172–1180, 1988.

[54] A. Kryazhev, M. Buyanova, V. Semenov, D. Anderson, M. Lisak, J. Puech, L. Lapierre, and J. Sombrin, “Hybrid resonant modes of two-sided multipactor and transition to the polyphase regime,” *Physics of Plasmas (1994-present)*, vol. 9, no. 11, pp. 4736–4743, 2002.

[55] R. Kishek and Y. Y. Lau, “Interaction of multipactor discharge and rf circuit,” *Physical review letters*, vol. 75, no. 6, p. 1218, 1995.

[56] R. Udiljak, D. Anderson, M. Lisak, V. E. Semenov, and J. Puech, “Multipactor in a coaxial transmission line. i. analytical study,” *Physics of Plasmas (1994-present)*, vol. 14, no. 3, 2007.

[57] A. Sounas, E. Sorolla, and M. Mattes, “Analysis of Multipactor Effect in Coaxial Lines,” in *Proceedings of the MULCOPIM’11*, 2011.

[58] E. Sorolla, “Contribution to modelling multipactor and corona discharges in high power electromagnetic fields,” Ph.D. dissertation, École Polytechnique Fédérale de Lausanne, 2012.

[59] S. Riyopoulos, D. Chernin, and D. Dialetis, “Effect of random secondary delay times and emission velocities in electron multipactors,” *Electron Devices, IEEE Transactions on*, vol. 44, no. 3, pp. 489–497, Mar 1997.

[60] “High power SMA connectors,” Tech. Rep. ESA Contract No. 20967/07/NL/GCL.

[61] R. Woo, “Multipacting discharges between coaxial electrodes,” *Journal of Applied Physics*, vol. 39, no. 3, pp. 1528–1533, Feb 1968.

[62] M. H. W. Arter, “Multipaction threshold curves for coaxial geometries,” AEA Technology plc, Abingdon, U.K., Tech. Rep. AEA/TYKB/28046/RP/1, May 1997.

[63] V. E. Henrich, “Fast, accurate secondary electron yield measurements at low primary energies,” *Review of Scientific Instruments*, vol. 44, no. 4, pp. 456–462, Apr 1973.

[64] A. N. Andronov, A. S. Smirnov, I. D. Kaganovich, E. A. Startsev, Y. Raitses, and V. I. Demidov, “Secondary electron emission yield in the limit of low electron energy,” workshop on Electron-Cloud Effects: ECLOUD’12; 5-9 Jun 2012, La Biodola, Isola d’Elba, Italy.

[65] I. Khan, J. Hobson, and R. Armstrong, “Reflection and diffraction of slow electrons from single crystals of tungsten,” *Phys. Rev.*, vol. 129, pp. 1513–1523, Feb 1963.

[66] J. Roupie, O. Jbara, T. Tondu, M. Belhaj, and J. Puech, “The study of electron emission from aluminum in the very low primary energy range using monte carlo simulations,” *Journal of Physics D: Applied Physics*, vol. 46, no. 12, p. 125306, 2013.

[67] R. Seviour, “The role of elastic and inelastic electron reflection in multipactor discharges,” *Electron Devices, IEEE Transactions on*, vol. 52, no. 8, pp. 1927–1930, Aug 2005.

[68] V. Semenov, E. Rakova, D. Anderson, M. Lisak, and J. Puech, “Importance of reflection of low-energy electrons on multipactor susceptibility diagrams for narrow gaps,” *Plasma Science, IEEE Transactions on*, vol. 37, no. 9, pp. 1774–1781, Sept 2009.

[69] M. A. M. A. V. Gaponov, “Potential wells for charged particles in a high-frequency electromagnetic field,” *JETP*, vol. 7, p. 168, 1958.

[70] D. P. E. Somersalo, P. Yla-Oijala, “Analysis of multipacting in coaxial lines,” in *Proceedings of 1995 Particle Accelerator Conference.*

[71] E. Somersalo, P. Yla-Oijala, J. Sarvas, and D. Proch, “Computational methods for analyzing electron multipacting in RF structures,” *Part.Accel.*, vol. 59, pp. 107–141, 1998.

[72] E. Chojnacki, “Simulations of a multipactor-inhibited waveguide geometry,” *Phys.Rev.ST Accel.Beams*, vol. 3, p. 032001, 2000.

[73] V. E. Semenov, N. Zharova, R. Udiljak, D. Anderson, M. Lisak, and J. Puech, “Multipactor in a coaxial transmission line. ii. particle-in-cell simulations,” *Physics of Plasmas (1994-present)*, vol. 14, no. 3, pp. –, 2007.

[74] S. Nagesh, D. Revannasiddiah, and S. Shastry, “Investigation of multipactor breakdown in communication satellite microwave co-axial systems,” *Pramana*, vol. 64, no. 1, pp. 95–110, 2005.

[75] A. Perez, C. Tienda, C. Vicente, S. Anza, J. Gil, B. Gimeno, V. Boria, and D. Raboso, “Prediction of multipactor breakdown thresholds in coaxial transmission lines for traveling, standing, and mixed waves,” *Plasma Science, IEEE Transactions on*, vol. 37, no. 10, pp. 2031–2040, Oct 2009.

[76] T. P. Graves, B. LaBombard, S. Wukitch, and I. Hutchinson, “The coaxial multipactor experiment (cmx): A facility for investigating multipactor discharges,” *Review of Scientific Instruments*, vol. 77, no. 1, pp. –, 2006.

[77] I. A. Kossyi, G. S. Luk’yanchikov, V. E. Semenov, N. A. Zharova, D. Anderson, M. Lisak, and J. Puech, “Experimental and numerical investigation of multipactor discharges in a coaxial waveguide,” *Journal of Physics D: Applied Physics*, vol. 43, no. 34, p. 345206, 2010.

[78] R. Woo and A. Ishimaru, “A similarity principle for multipacting discharges,” *Journal of Applied Physics*, vol. 38, no. 13, 1967.

[79] E. Sorolla and M. Mattes, “Multipactor saturation in parallel-plate waveguides,” *Physics of Plasmas (1994-present)*, vol. 19, no. 7, p. 072304, 2012.

[80] R. E. Collin, *Field Theory of Guided Waves, 2^{nd} edition.* IEEE Press, 1991.

[81] G. Torregrosa-Penalva, A. Coves, B. Martinez, I. Montero, C. Vicente, and V. Boria, "Multipactor susceptibility charts of a parallel-plate dielectric-loaded waveguide," *Electron Devices, IEEE Transactions on*, vol. 57, no. 5, pp. 1160–1166, May 2010.

[82] S. Humphries, "Modeling secondary emission in a finite-element multipactor code," in *Proceedings of the 9 th Workshop on RF Superconductivity*, 1999, pp. 390–396.

[83] L.-K. Ang, Y. Lau, R. A. Kishek, and R. M. Gilgenbach, "Power deposited on a dielectric by multipactor," *Plasma Science, IEEE Transactions on*, vol. 26, no. 3, pp. 290–295, 1998.

[84] I. Kossyi, G. Luk'Yanchikov, V. Semenov, N. Zharova, D. Anderson, M. Lisak, and J. Puech, "Experimental and numerical investigation of multipactor discharges in a coaxial waveguide," *Journal of Physics D: Applied Physics*, vol. 43, no. 34, p. 345206, 2010.

[85] A. Valfells, L. Ang, Y. Lau, and R. Gilgenbach, "Effects of an external magnetic field, and of oblique radio-frequency electric fields on multipactor discharge on a dielectric," *Physics of Plasmas (1994-present)*, vol. 7, no. 2, pp. 750–757, 2000.

[86] A. Pérez, C. Tienda, C. Vicente, J. Sánchez, A. Coves, G. Torregrosa, A. San Blas, B. Gimeno, and V. Boria, "Multicoax: a software tool for predicting multipactor rf breakdown threshold in coaxial and circular waveguides," in *Proceedings of the 5th International Workshop on Multipactor, Corona and Passive Intermodulation in Space RF Hardware (MULCOPIM), ESA/ESTEC, Noordwijk, The Netherlands*, 2005, pp. 27–34.

[87] V. Semenov, N. Zharova, D. Anderson, M. Lisak, and J. Puech, "Simulations of multipactor in circular waveguides," *Physics of Plasmas (1994-present)*, vol. 17, no. 12, p. 123503, 2010.

[88] S. Anza, C. Vicente, D. Raboso, J. Gil, B. Gimeno, and V. Boria, "Enhanced prediction of multipaction breakdown in passive waveguide components including space charge effects," in *Microwave Symposium Digest, 2008 IEEE MTT-S International*, June 2008, pp. 1095–1098.

[89] H. C. Kim and J. P. Verboncoeur, "Time-dependent physics of a single-surface multipactor discharge," *Physics of Plasmas (1994-present)*, vol. 12, no. 12, 2005.

[90] R. Udiljak, D. Anderson, M. Lisak, J. Puech, and V. E. Semenov, "Multipactor in a waveguide iris," *Plasma Science, IEEE Transactions on*, vol. 35, no. 2, pp. 388–395, 2007.

[91] A. L. Sounas, E. Sorolla, and M. Mattes, "Multipactor analysis in parallel-plate waveguides loaded by a single dielectric slab," in *Antennas and Propagation (EuCAP), 2014 8th European Conference on*, April 2014, pp. 1469–1470.

[92] A. Sommerfeld, *Partial differential equations in physics.* Academic press, 1949, vol. 1.

[93] J. Mosig, “Integral equation technique,” in *Numerical Techniques for Microwave and Millimeter Wave Passive Structures*, T. Itoh, Ed. New York: Wiley, 1989, ch. 3.

[94] L. B. Felsen and N. Marcuvitz, *Radiation and Scattering of Waves.* IEEE Press, 1994.

[95] I. Stakgold, *Boundary Value Problems of Mathematical Physics, Vol. II.* SIAM, 2000, vol. II.

[96] D. J. Griggiths, *Introduction to Electrodynamics, 3^{rd} edition.* Prentice-Hall, 1999.

[97] J. Kraus and K. Carver, *Electromangetics, 2^{nd} edition.* McGraw-Hill, 1973.

[98] Y. Chow, J. Yang, D.-G. Fang, and G. Howard, “A closed-form spatial Green’s function for the thick microstrip substrate,” *Microwave Theory and Techniques, IEEE Transactions on*, vol. 39, no. 3, pp. 588–592, Mar 1991.

[99] Y. Chow, J. Yang, and G. Howard, “Complex images for electrostatic field computation in multilayered media,” *Microwave Theory and Techniques, IEEE Transactions on*, vol. 39, no. 7, pp. 1120–1125, Jul 1991.

[100] P. Silvester, “TEM wave properties of microstrip transmission lines,” *Electrical Engineers, Proceedings of the Institution of*, vol. 115, no. 1, pp. 43–48, January 1968.

[101] T. Sometani, “Image method for a dielectric plate and a point charge,” *European Journal of Physics*, vol. 21, no. 6, p. 549, 2000.

[102] J. Mosig, “Les structures microruban: Analyse au moyen des equations intégrals,” Ph.D. dissertation, École Polytechnique Fédérale de Lausanne, 1983.

[103] A. Papoulis, *The Fourier Integral and its Applications.* New York: McGraw-Hill, 1962.

[104] O. Kurokawa, “Shielding apparatus for a printed circuit board,” 1988, US Patent 4,739,453.

[105] R. Hui and S. Tang, “Planar printed-circuit-board transformers with effective electromagnetic interference (EMI) shielding,” 2002, US Patent 6,501,364.

[106] B. Archambeault, C. Brench, and S. Connor, “Review of printed-circuit-board level EMI/EMC issues and tools,” *Electromagnetic Compatibility, IEEE Transactions on*, vol. 52, no. 2, pp. 455–461, May 2010.

[107] R. Harringthon, *Field Computation by Moment Methods.* Willey-IEEE Press, 1993.

[108] P. P. Ewald, “Die Berechnung optischer und elektrostatischer gitterpotentiale,” *Ann. der Phys.*, vol. 64, pp. 253–287, 1921.

[109] M.-J. Park, J. Park, and S. Nam, “Efficient calculation of the Green’s function for the rectangular cavity,” *IEEE Microw. Guided Wave Lett.*, vol. 8, no. 3, pp. 124–126, March 1998.

[110] G. Lovat, P. Burghignoli, and R. Araneo, “Efficient evaluation of the 3-d periodic Green’s function through the Ewald method,” *IEEE Trans. Microw. Theory Tech.*, vol. 56, no. 9, pp. 2069–2075, 2008.

[111] J. Mosig, “The weighted averages algorithm revisited,” *Antennas and Propagation, IEEE Transactions on*, vol. 60, no. 4, pp. 2011–2018, April 2012.

List of Figures

1.1. Trend of power capability of GEO satellites. Source: WTEC Panel Report on Global Satellite Communications Technology and Systems, December 1998 International Technology Research Institute Baltimore, Maryland 21210-2699 ISBN 1-883712-51-3 2

2.1. Multipacting process. (a) A free electron is accelerated by the electric field. (b) The electron hits the surface and (c) causes the emission of two secondary electrons. The field reverses direction and the new electrons are accelerated towards the opposite conductor. (d) The procedure continues. 8

2.2. Emission mechanisms occuring after impact of an electron bunch impact on a surface. 9

2.3. A typical Secondary Emission Yield (SEY) curve as a function of the impact energy. The total SEY results from the contribution of the true secondary, of the inelastically backscattered and of the elastically reflected electrons. 10

2.4. SEY curve as it was measured on a molybdenum sample for several incidence angles [51]. 11

2.5. A sample of the emission energy spectrum extracted from [49]. The primary energy is $E_{\mathrm{PE}} = 300$eV. The areas that correspond to each emission mechanism are separated by the red dashed lines. 12

2.6. Measured EDCs for different primary energies extracted from [50]. 13

2.7. Angular distribution of the true secondary electrons. The length of each arrow is proportional to the number of the emitted electrons. 13

2.8. Periodic motions of electrons in parallel plates configuration: (a) 1^{st} resonance order, (b) 3^{rd} resonance order. The electrons are emitted with a time difference τ_{res} with respect to the moment at which the electric field changes polarity. i.e every half period. The corresponding resonant phase is equal to $\varphi_{\mathrm{res}} = \omega\tau_{\mathrm{res}}$, where ω is the angular frequency of the applied RF field. 15

2.9. Conditions for achieving 1^{st} resonance order in parallel-plates configuration. A constant emission velocity equal to $u_0 = 4\,\mathrm{eV}$ is considered. 15

2.10. Single side resonant motion in a coaxial cable. The following parameters are considered: $r_{outer}/r_{inner} = 5.3$, $V = 150$ V and $f = 65$ GHz where r_{inner} and r_{outer} is the radius of the inner and the outer conductor, respectively, V the gap voltage between the conductors and f the frequency of the applied RF field. A constant emission velocity equal to $u_0 = 4\,\mathrm{eV}$ is considered. 16

2.11. Phase focusing mechanism when the electron is emitted with a initial phase error considering constant emission velocity: (a) electron motion, (b) phase error at the impact events. 17

2.12. Phase focusing mechanism when the electron is emitted with a random initial velocity that follows a normal distribution with $\mu = u_0 = 4$ eV and $\sigma = 0.3$ eV: (a) electron motion, (b) phase error at the impact events. 17

3.1. Configuration under study: two infinite parallel plates are considered, lying on xy plane. An external alternating voltage V_{rf} is applied between the plates. The single electron model is assumed: the electrons move in z direction, normally to the plates, all with the same speed, composing an infinite electron sheet. . . 23

3.2. Theoretical resonant motion without considering the presence of the plates. a) The electron returns back to the initial plate before it reaches the opposite one. b) Advanced impact on the opposite plate before the predicted impact at $t_{\mathrm{imp,res}}$. 26

3.3. Solid lines: Gap voltage required so that the resonant electrons hit the opposite plate with a certain impact energy. The dashed line corresponds to the minimum possible gap voltage needed for resonant motion, i.e. $V_{\mathrm{res,min}}$ as given in Eq. (3.6). The 1st resonance mode is considered. The emission velocity is $u_0 = 4$eV 28

3.4. Range of stable resonance phases according to Eq. (3.16). Stability is assured in the grey area, i.e. in the range $[\varphi_{\mathrm{l,max}}, \varphi_u]$. Stability is possible under conditions in the white area i.e. in the range $[\varphi_{\mathrm{l,min}}, \varphi_{\mathrm{l,max}}]$, while stability is impossibe in the remaining, shadowed area. The phase range of the resonance phases $a^{(1)}_{0,\mathrm{res}}$ and $a^{(2)}_{0,\mathrm{res}}$ are also depicted, under the assumption $\omega h > N\pi u_0$. The arrows show the trend of $a^{(1)}_{0,\mathrm{res}}$, $a^{(2)}_{0,\mathrm{res}}$ and φ_{l} as the applied gap voltage increases. 29

3.5. a) Lower and b) upper multipactor threshold for the 1st multipactor mode. The parameters are: $u_0 = 3.68$eV, $u_1 = 30$eV and $u_2 = 1000$eV. 31

3.6. Multipactor chart using the same parameters as in Figs. 3.5a and 3.5b. The first four, odd-order, resonance modes are considered. The zones delimited by solid lines indicate the areas within which phase-focusing is active (stable resonance). The dashed lines represent zones without considering the stability condition (unstable phases are also included). 33

3.7. Qualitative representation of the applied SEY model [3]. The SEY function (solid black line) considers additively all the secondary emission mechanisms. . 35

3.8. Different representations of multipactor chart. a) Multipactor threshold. b) Multipacting rate per period expressed by exponential coefficient a_{T} as given in Eq. (3.26). c) Geometric mean value of SEY at impacts. d) Multipacting rate expressed by exponential coefficient a as given in Eq. (3.23). The color scale is linear in all cases. Results have been obtained by considering SEY properties of silver. For the studied case the maximum values in the charts b), c) and d) are $a_{\mathrm{T,max}} = 0.8$, $\delta_{\max} = 2.22$ and $a_{\max} = 2$ ps^{-1}, respectively. 37

3.9. Multipactor zones in parallel plates considering SEY parameters of silver. . . . 38

3.10. Electron motion corresponding to points A and B of Fig. 3.9. a) point A: $fh = 3.73$ GHz mm, $V = 240$ V, b) point B: $fh = 4.86$ GHz mm, $V = 1030$ V . 39

3.11. Multipactor chart for coaxial lines compared with a) Woo experiments [61] for a coaxial line of copper and b) numerical results for a coaxial line of alodine [62]. In both cases the characteristic impedance is equal to $Z = 50\ \Omega$. 40

3.12. Multipactor threshold considering different values for the elastic reflection coefficient $e_{0,\text{elast}}$. Parallel plates made of silver are considered. 42

3.13. Electron motion for the cases A, B, C and D as depicted in Fig. 3.12. a) point A: $fh = 0.65$ GHz mm and $V = 100$ V and b) point B: $fh = 0.75$ GHz mm and $V = 30$ V, c) point C: $fh = 1.35$ GHz mm and $V = 50$ V and d) point D: $fh = 1.9$ GHz mm and $V = 115$ V 43

3.14. Distribution of impact energy for the cases C and D as depicted in Fig. 3.12. a) point C: $fh = 1.35$ GHz mm and $V = 50$ V and b)D: $fh = 1.90$ GHz mm and $V = 115$ V. For illustration purposes the SEY curve used in the example of Fig. 3.12 for $\varepsilon_{0,\text{elast}} = 1$ is depicted, too. SEY values correspond to the right vertical axis. 43

3.15. Electric field distribution between the inner and the outer conductor in coaxial lines. The electric field component is normalized to the field at the middle point between the two conductors. The horizontal dashed line corresponds to the case of parallel plates. 44

3.16. Multipactor threshold for different gaps. A coaxial line made of copper, with a characteristic impedance equal to $Z = 50\ \Omega$, is considered. 46

3.17. Multipactor chart in coaxial lines. Color intensity represents the geometric mean SEY value. Both electrodes are made of copper. Different characteristic impedances, Z are considered: a) parallel plates ($Z \to 0\ \Omega$), b) $Z = 50\ \Omega$, c) $Z = 75\ \Omega$ and d) $Z = 100\ \Omega$. 48

3.18. Single-sided multipaction in coaxial lines considering a characteristic impedance of a) $Z = 50\ \Omega$ and b) $Z = 100\ \Omega$. The SEY parameters of silver have been used (see Table 3.2). 49

4.1. Configuration under study: A parallel-plate waveguide loaded by a single dielectric layer. 52

4.2. The proposed 1D model for the investigation of the long-term multipactor evolution in parallel plates loaded by a single dielectric slab. The electron population is represented by an electron sheet, according to the single electron approach (see Chapter 3). A homogeneous surface charge is considered on the dielectric surface. Its intensity changes after electron collisions with the dielectric slab. Saturation is modeled by considering the field due to the surface charge and due to the charges induced by the electron sheet on the metal plates 54

4.3. Qualitative representation of the results reported in literature [31, 32],. The electron population and the surface charge on the dielectric are simultaneously increasing. When the surface charge becomes high the DC-field due to the surface charge leads to the decrease of the electron population. Note, that both positive and negative net charge on the dielectric surface has been reported in the literature. However, for both cases result the electron cloud disappears at the end. 59

4.4. **Short term evolution:** Mulipactor chart for parallel plates loaded by a single dielectric slab. The color intensity represents the geometric mean SEY value at impacts, $\langle \text{SEY} \rangle$, for the first phase of the multipactor evolution (multipactor onset). The following parameters have been considered: $h = 1.1$mm, $d = 0.1$mm and $\epsilon_r = 3$. The SEY properties of silver, as given in Table 3.2, have been assumed for both metal and dielectric surfaces. Long-term multipaction will be studied later for the points A and B. A: $V = 45$ V, $f = 1$ GHz, B: $V = 110$ V, $f = 1.2$ GHz 61

4.5. Time evolution of the charge density (amplitude) of the electron sheet, $|\sigma_{\text{el}}|$ and of the surface charge on the dielectric, $|\sigma_{\text{diel}}|$. The results correspond to the operation point A in Fig. 4.4. Note, that the vertical axis represents the amplitude of the charge densities, given in $|e|/\text{m}^2$, where e is the charge of a single electron. For the depicted case, the surface charge on the dielectric is positive. 62

4.6. Evolution of the charge density (amplitude) of the electron sheet and of the surface charge on the dielectric during the multipactor onset for the same case as in Fig. 4.5. Results obtained by neglecting the saturation mechanisms are also included for comparison reasons. The ration between the charge density of the electron sheet and the density of the surface charge on the dielectric is equal to $|\sigma_{\text{diel}}/\sigma_{\text{el}}| = 0.528$. 63

4.7. Electric field due to the saturation mechanisms (induced charge and surface charge) as a function of the position of the moving electron sheet, z'. The same configuration as in Fig. 4.4 is considered. The ratio between the density of the surface charge and the density of the electron sheet corresponds to the one of Fig. 4.6, i.e. $\sigma_{\text{diel}}/\sigma_{\text{el}} = -0.528$ ($\sigma_{\text{el}} < 0$ and $\sigma_{\text{diel}} > 0$). 64

4.8. Evolution of the electron population for the examined case A (see Fig. 4.4). Three different models have been considered regarding the saturation mechanisms. Dashed line marked with circles: only the induced charge is taken into account. Dashed line marked with rectangles: only the surface charge on the dielectric is taken into account. Solid line: Full model taking into account both the induced charge and the surface charge both the induced charge and the surface charge (same as in Fig. 4.5). 64

4.9. Motion of the electron sheet during the saturation stage. The case A of Fig. 4.4 is considered. 65

4.10. SEY at impact events during the transition from the multipactor onset to the saturation. The case A of Fig. 4.4 is considered. 65

4.11. SEY at impact events during the transition from the saturation stage to the final extinguishing stage. 66

4.12. Time evolution of the charge density (amplitude) of the electron sheet, $|\sigma_{\mathrm{el}}|$ and of the surface charge on the dielectric, $|\sigma_{\mathrm{diel}}|$. The results correspond to the operation point B in Fig. 4.4. Note, that the vertical axis represents the amplitude of the charge densities, given in $|e|/\mathrm{m}^2$, where e is the charge of a single electron. 67

4.13. Motion of electron sheet during the saturation stage. The case B of Fig. 4.4 is considered. 68

4.14. Electric field (normalized to the peak value of the RF field) as a function of time. 68

4.15. **Long term evolution:** Multipactor chart showing in which area each of the two long-term evolution mechanism occurs. The same parameters as in the Fig. 4.4 have been considered. 70

4.16. Discretization of the dielectric surface into patches. The surface charge density on a single patch is considered constant. After every impact event, the total charge of the corresponding patch changes according to the charge added at the collision point. 74

4.17. Configuration under study in the 3D analysis. The following dimensions are considered: $h = 1.1$mm, $d = 0.1$mm, $w = 5$mm. The dielectric constant of the slab is equal to $\varepsilon_{\mathrm{r}} = 3$ The SEY properties of silver are considered for both metallic and dielectric surfaces (see Table 3.2). The moving electrons that exceed the lateral limits are considered as lost. 77

4.18. Time evolution of the electron population (electron cloud) and of the accumulated charge on the dielectric (given in $|e|$, where e is the charge of a single electron). The results correspond to the operation point A in Fig. 4.4. The following simulation parameters have been considered: $N_{\mathrm{macro}} = 20000$, $\Delta x = 0.1$ mm and $\Delta y = 0.1$ mm, where N_{macro} is the number of the macroparticles, Δx and Δy the dimensions of each surface patch. 77

4.19. Electron cloud distribution at the end of the simulation of the studied case (same parameters as in Fig. 4.18). 78

4.20. Charge density on the dielectric surface at the end of the simulation of the studied case (same parameters as in Fig. 4.18) 79

5.1. Parallel plates waveguide partially loaded by a dielectric slab. 82

5.2. Eigenvalues of the characteristic equation (5.5). The following configuration has been considered: $h = 1.5\,\mathrm{mm}$, $d = 0.25\,\mathrm{mm}$ and $\varepsilon_{r,2} = 9$. The corresponding integer coefficients of Eq. (5.11) are $p = 3$ and $q = 2$ while the fundamental period of the eigenvalues is equal to $T = 4\pi$. 85

5.3. Main steps of the proposed image method. 87

5.4. Charges of the images for both set of images as defined in Table 5.1. The following configuration has been considered: $h = 2\text{mm}$, $d = 0.25\text{mm}$, $\varepsilon_{r,2} = 2$ and $z_0 = 1.65\text{mm}$. The vertical lines correspond to the margins of the structure: the two black lines represent the lower and the upper metallic plate, the green one the limit of the dielectric slab. The first images with zero charge are marked by the rectangular dashed box. The first images with non zero charge (excluding the main images of both sets, i.e. for $n = 0$), are marked with dashed circles. 88

5.5. Potential Green function as a function of the radial distance between the source and the observation point. The source and the observation point are placed on the same altitude position of $z_0 = z = 0.5\text{mm}$. A number of $N_{\text{mod}} = 1000$ modes and $N_{\text{WA}} = 35$ partial integrals has been used for the modal expansion and the Sommerfeld integration, respectively, while several simulations with different number of images have been performed. 91

5.6. Electric field GF (both $z-$ and $\rho-$components) as a function of the radial distance. The altitude position of the source and the observation point are $z_0 = 0.4\text{mm}$ and $z = 0.6\text{mm}$, respectively. 91

5.7. Convergence of the potential GF. Two different cases are studied: in the first one the source is located close to the dielectric surface with $z_{0,1} = d{+}0.1\,(h-d)$ and in the other the source is close to the metal plate with $z_{0,2} = h{-}0.1\,(h-d)$. For both cases, the observation point is placed on the same altitude level as the corresponding source and in a radial distance of $\rho = 0.05h$. 92

5.8. Convergence of the electric field GF. Two different cases are studied: in the first one the source is located close to the dielectric surface with $z_{0,1} = d{+}0.1\,(h-d)$ and in the other the source is close to the metal plate with $z_{0,2} = h{-}0.1\,(h-d)$. For both cases, the observation point is placed at the same altitude level as the corresponding source and in a radial distance of $\rho = 0.05h$. 93

5.9. Relative error of the Green function as a function of the radial distance. A number of $N_{\text{imag}} = 1000$ and $N_{\text{modes}} = 15$ has been considered, resulting in the same CPU time for both image and modal series simulations. The source and observer are placed on the same altitude level of $z_0 = z = 0.5\text{mm}$. 94

5.10. CPU time needed for the calculation of the potential Green Function with a relative error equal to 10^{-5}. The source and the observation point are considered to be placed on the dielectric surface, i.e. $z_0 = z = d = 0.3\text{mm}$. 95

5.11. Relative error of the electric field Green function obtained by the proposed image method considering the first $N_{\text{imag}} = 1000$ terms. In total, 10^4 observation points have been simulated resulting in a CPU time of approximately 1.59 sec . 96

5.12. Relative error of the electric field Green function obtained by modal expansion considering the first $N_{\text{modes}} = 15$ terms. In total, 10^4 observation points have been simulated resulting in a CPU time of approximately 1.51 sec 96

5.13. Electric field on the source due to the induced charges, along the z axis. For the image method, a number of $N_{imag} = 1000$ terms has been used. 97

5.14. CPU time needed for the calculation of the induced electric field on a source considering a relative error of 10^{-5}. 98

A.1. Graphical explanation of the conditions described in Eq. (A.7). The integer k of Eq. (A.6) is considered to be even, resulting in $h\left(x_1\right) > 0$ and $h\left(x_2\right) < 0$. Considering the existence of multiple roots, there would be at least one satisfying $h'\left(x_r\right) \geq 0$. In the depicted case, this corresponds to the root $x_{r,2}$, as it is illustrated by the tangent, dashed, line. The equality holds in the extreme case where two roots, e.g. $x_{r,2}, x_{r,3}$, overlap. 103

List of Tables

3.1. Multipacting Conditions. 32
3.2. SEY properties for different materials applying SEY model of [3] 35

5.1. Positions & Charges of the images. 86
5.2. CPU time for the calculation of a single term of each method. 90

Apostolos Sounas

Curriculum Vitae

Address: Institute of Electrical Engineering
Ecole Polytechnique Fédérale de Lausanne
LEMA ELB 010, Station 11
Lausanne, CH-1015, Switzerland
Phone: +41 216934641
+41 767425218
Email: apostolos.sounas@epfl.ch

General Information

April 25, 1986	Date of Birth: Polygyros, Greece Marital status: Single

Education

2010 – 2014	**Ph.D in Electrical Engineering** Laboratory of Electromagnetics and Acoustics (LEMA) Ecole Polytechnique Fédérale de Lausanne (EPFL) Thesis Title: “*Modeling of Long-Term Multipactor Evolution in Microwave Components Including Dielectric Layers*” Thesis director: Juan R. Mosig Thesis co-director: Michael Mattes
2004 – 2009	**Diploma of Electrical and Computer Engineering (5 years degree)** Aristotle University of Thessaloniki, Greece GPA: 8.59/10.00 Rank: 6th among 345 graduates (top 1.5%)

Professional Experience

2010 – present	**Research Assistant at the Laboratory of Electromagnetics and Acoustics (LEMA)** Ecole Polytechnique Fédérale de Lausanne (EPFL)
2010 – 2012	**Technical Researcher** Project: POSEIDON – *Development of a Novel Platform for the Numerical Analysis and Synthesis of Next-Generation Microwave Devices and Technologies.* Funded by: Swiss Commission for Technology and Innovation (CTI) Partners: SPEAG AG, LEMA EPFL, IT’IS foundation ETHZ Task: Efficient Multipactor Solver for New Generation Space Applications
2010 – present	**Library Manager of Laboratory of Electromagnetics and Acoustics (LEMA)** Ecole Polytechnique Fédérale de Lausanne (EPFL)
July – Aug. 2008	**Internship in Public Power Corporation,** Polygyros, Greece Detection of electrical failures and control of power distribution network.

Teaching Experience

2011 – 2013
Teaching Assistant
Electromagnetism I & II

Spring 2012
Semester Projects Supervisor
Mikael Walter, Analyse Electromagnétique avec la Méthode des Différences Finies

Summer 2011
Erasmus Projects Supervisor
Maria Salvatierra, Development of a GUI environment for the multipactor analysis in parallel-plates waveguides

Awards - Distinctions

1999 – 2003
17th – 20th National Mathematical Olympiads (Archimedes), Athens, Greece
- Finalist (Top 50 in national level)
- Finished 15th in 18th National Mathematical Olympiad

2004
Graduation Award of excellence and Scholarship
EFG Eurobank Greek Bank

Languages

Greek (native speaker)
English (fluent)
French (beginner)

Computer Experience

Programming Languages
C++, C, Matlab, Mathematica, Python, Java

Engineering Software
Spice, Autocad, SEMCAD, CST Microwave Studio, CST Particle Studio, FEST3D, SPARK3D

Other Software
MS Office, Corel Draw, Latex Word Processing

Professional Committees

- Institute of Electrical and Electronics Engineers, IEEE
- Technical Chamber of Greece (TEE - TCG)

Scientific Interests

Electromagnetics
electromagnetic theory, computational electromagnetics, microwave devices, antennas, filters

Plasma Physics
multipaction, electron cloud effect, corona discharge, particle dynamics

Numerical Modeling
method of moments (MoM), finite element method (FEM), finite-difference time domain (FDTD), boundary element method (BEM), N-body algorithms

List of Publications

Refereed Journal Papers

1. E. Sorolla, A. Sounas and M. Mattes, “Space Charge Effects for Multipactor in Coaxial Lines”, accepted for publication in *Physics of Plasmas*.

2. A. Sounas, I. Koufogiannis, J. R. Mosig and M. Mattes, “Image Method for the Electrostatic Green Function in Multilayered Shielded Media”, submitted in *Antennas and Propagation, IEEE Transaction on*.

Conference Papers

1. A. Sounas, E. Sorolla and M. Mattes, “Investigation of Multipactor Steady State in Paralle-Plate Waveguides Loaded by a Single Dielectric Slab”, MULCOPIM 2014, Valencia, Spain Sept. 17-19, 2014

2. A. Sounas, E. Sorolla and M. Mattes, Long-Term Multipactor Evolution in the Case of Amplitude Modulation Schemes”, MULCOPIM 2014, Valencia, Spain, Sept. 17-19, 2014

3. A. Sounas, E. Sorolla and M. Mattes, “Multipactor Analysis in Parallel-Plate Waveguides Loaded by a Single Dielectric Slab”, 8th European Conference on Antennas and Propagation (EuCAP), The Hague, Netherlands, April 6-11, 2014

4. A. Sounas, J. R Mosig and M. Mattes, “Effect of Digitally Modulated Signals on Multipactor Breakdown”, 7th European Conference on Antennas and Propagation (EuCAP), Gothenburg, Sweden, April 8-12, 2013

5. A. Sounas and M. Mattes, “Multipaction Analysis under Digitally Modulated Signals”, 5th International Workshop on Microwave Filters (IWMF), Toulouse, France, Oct. 1-3, 2012

6. A. Sounas and T. Yioultsis, “Explicit Scheme for Indoor Propagation Modeling Based on the Hybrid Parabolic-Integral Equation Method”, 6th European Conference on Antennas and Propagation (EuCAP), Prague, Czech Republic, Mar. 26-30, 2012

7. A. Sounas, E. Sorolla and M. Mattes, “Analysis of Multipactor Effect in Coaxial Lines”, MULCOPIM 2011, Valencia, Spain Sept. 21-23, 2011